NASA Technical Paper 3330

ATCOM Technical Report 93-A-004

May 1993

Determining XV-15 Aeroelastic Modes from Flight Data with Frequency-Domain Methods

C. W. Acree, Jr.
and Mark B. Tischler

US ARMY
AVIATION and
TROOP COMMAND

National Aeronautics and
Space Administration

NASA Technical Paper 3330

ATCOM Technical Report 93-A-004

1993

Determining XV-15 Aeroelastic Modes from Flight Data with Frequency-Domain Methods

C. W. Acree, Jr.
Ames Research Center, Moffett Field, California
and
Mark B. Tischler
Aeroflightdynamics Directorate
U.S. Army Aviation and Troop Command
Ames Research Center, Moffett Field, California

National Aeronautics and Space Administration

Ames Research Center
Moffett Field, California 94035-1000

CONTENTS

NOMENCLATURE

Symbols

A	frequency-response gain factor
C_p/σ_r	ratio of power coefficient to rotor solidity
C_ε	overlapped-window correction factor
f	frequency, Hz
f_i	discrete frequency point, Hz
f_n	natural frequency, Hz
f_s	zero-airspeed structural frequency, Hz
$G_{n_i n_i}(f)$	input measurement-noise autospectrum
$G_{xx}(f)$	input signal autospectrum
$G_{xy}(f)$	cross-spectrum between input and output signals
$G_{yy}(f)$	output signal autospectrum
$H(f)$	frequency response
$H_M(f)$	modeled (assumed) frequency response
i	curve-fit frequency index
k	time-history section index
K	number of time-history sections = $2n_d - 1$
L	number of data points in one time-history section
n_d	number of data sections (statistically independent) = $T_c / L\Delta t$
$n_i(t)$	input measurement noise
$n_o(t)$	output measurement noise
$n_p(t)$	unmeasurable input (process noise)
N	number of curve-fit frequency points
Q	curve-fit cost function
T	length of each time-history section, sec
T_c	total length of concatenated time histories, sec
U	scale factor for the time-history window function
V	frequency sweep rate, Hz/sec
$W(f)$	curve-fit error weighting function
$x(t)$	actual input
$x_1(t) \ldots x_{nr}(t)$	1st through nth input data records
$x_m(t)$	measured input
$y_1(t) \ldots y_{nr}(t)$	1st through nth output data records
$y_m(t)$	measured output
$X_k(f)$	discrete-frequency Fourier coefficient for the input
$Y_k(f)$	discrete-frequency Fourier coefficient for the output
$\gamma^2_{xy}(f)$	coherence function
Δf	frequency separation of adjacent modes, Hz
Δt	sampling interval for time-history data, sec
$\Delta\omega$	chirp z-transform frequency increment, rad/sec
σ_d	air density ratio
σ_{f_n}	standard deviation of the natural frequency
σ_ζ	standard deviation of the damping ratio
ω	frequency, rad/sec
ω_n	undamped natural frequency, rad/sec
ω_0, ω_1	chirp z-transform initial and final frequencies, rad/sec
ζ	damping ratio
ζ_{se}	zero-airspeed structural damping ratio, empirically adjusted
ζ_{sm}	zero-airspeed structural damping ratio, from model tests

Operators

Im[ ]	imaginary part of complex function [ ]
Re[ ]	real part of complex function [ ]
ε[ ]	normalized spectral random error of [ ]
|[ ]|	magnitude of complex function [ ]
$\angle$[ ]	angle of complex function [ ]
$\overline{[\ ]}$	average of [ ]
$\hat{[\ ]}$	estimate of [ ]
[ ]*	complex conjugate of [ ]

Acronyms

ARS	Attitude Retention System
ASAP	Aeroelastic Stability Analysis of Prop-Rotors
ATB	Advanced Technology Blades
CAMRAD	Comprehensive Analytical Model of Rotorcraft Aerodynamics and Dynamics
CIFER	Comprehensive Identification from FrEquency Responses
FFS	Force Feel System
FFT	fast Fourier transform
FIR	finite impulse response
FRESPID	Frequency Response Identification
HD	density altitude, ft
KCAS	knots calibrated airspeed
KIAS	knots indicated airspeed
KTAS	knots true airspeed
LVDT	linear variable differential transformer
NASTRAN	NASA Structural Analysis
PASTA	Proprotor Aeroelastic Stability Analysis
PCM	pulse code modulation
RHPN	normalized rotor shaft horsepower, hp/σ_d
rms	root mean square
rpm	revolutions per minute
SCAS	Stability Control Augmentation System
TRENDS	Tilt-Rotor Engineering Database System

Notes on Units

Two different units of frequency are used in this report. The natural mathematical unit for frequency is radians per second (rad/sec); the associated variable is ω. The programs FRESPID and NAVFIT use this unit for both input and output. The common engineering unit is cycles per second, or Hertz (Hz); the associated variable is f. The flight-test literature usually uses this unit. Both units are used herein as is appropriate to the context.

The damping ratio, ζ, is dimensionless and is so calculated by CAMRAD, ASAP, and NAVFIT. Although it is common in flight-test work to report damping as a percentage of critical damping ($\zeta = 1$), damping is given herein in dimensionless form to avoid confusion with percentage errors.

SUMMARY

The XV-15 tilt-rotor wing has six major aeroelastic modes that are close in frequency. To precisely excite individual modes during flight test, dual flaperon exciters with automatic frequency-sweep controls were installed. The resulting structural data were analyzed in the frequency domain (Fourier transformed). All spectral data were computed using chirp z-transforms. Modal frequencies and damping were determined by fitting curves to frequency-response magnitude and phase data. The results given in this report are for the XV-15 with its original metal rotor blades. Also, frequency and damping values are compared with theoretical predictions made using two different programs, CAMRAD and ASAP. The frequency-domain data-analysis method proved to be very reliable and adequate for tracking aeroelastic modes during flight-envelope expansion. This approach required less flight-test time and yielded mode estimations that were more repeatable, compared with the exponential-decay method previously used.

INTRODUCTION

The XV-15 tilt-rotor research aircraft has a large pylon on the end of each wing; each pylon houses the engine, transmission, and pivoting mechanism for its rotor. Figure 1 illustrates the three flight modes of the XV-15: cruise or "airplane" mode, with the pylons locked down; "tilt-rotor" mode, with the pylons partially tilted; and hover or "helicopter" mode, with the pylons vertical. Although the wings are short and thick, hence stiff, the concentrated masses at the pylons keep the modal frequencies of the wings fairly low. Furthermore, the aeroelastic coupling between each rotor, pylon, and wing is destabilizing. Consequently, close attention must be paid to potential whirl-mode instability (flutter) during flight test. The highest speeds are obtained in the cruise mode, making it the critical flight mode for aeroelastics.

The whirl-mode problem is not unique to the XV-15 research aircraft; it is fundamental to any tilt-rotor aircraft of similar configuration, such as the XV-3, for which it was extensively studied (refs. 1 and 2), and the V-22 Osprey (ref. 3). Reference 4 includes a summary of the development of whirl-mode flutter analyses as applied to tilt rotors. The impact of aeroelastic stability requirements on tilt-rotor design is discussed in reference 5.

The advent of the V-22, plus the planned flight tests of new composite rotor blades on the XV-15 (ref. 6), provided the incentive for a thorough reevaluation of XV-15 aeroelastics using the latest flight-test and mode-identification techniques. The flight-test program reported here had three basic purposes:

(a) "Airplane" flight mode

(b) "Tilt-rotor" flight mode

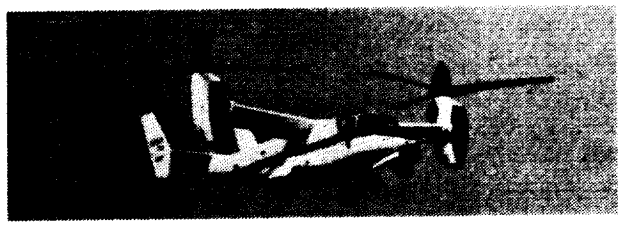

(c) "Helicopter" flight mode

Figure 1. Flight modes of the XV-15 tilt-rotor research aircraft. (a) "Airplane," (b) "Tilt-rotor," (c) "Helicopter."

1. The generation of a more reliable data base of XV-15 wing/pylon aeroelastic modes for the original metal blades and new steel hubs
2. The validation of new frequency-domain data-analysis techniques for identifying the modes
3. The development of improved flight-test techniques to support the new analytical techniques

In addition, the new flight-test data gave the opportunity to evaluate the latest predictive methods. Two different theoretical methods, embodied in the computer codes CAMRAD and ASAP, were used to predict the aeroelastic modes using mathematical models of the XV-15. Because the main focus of the flight-test program was to validate the new mode-identification technique within the existing XV-15 flight envelope before flying the new, composite Advanced Technology Blades (ATB), all

flight-test data and theoretical predictions discussed herein are for the metal blades.

The XV-15 wing modes were excited with flaperon frequency sweeps, and frequency spectra of the resulting time-history data were generated with chirp z-transforms. Modal freqencies and damping were determined by fitting curves to frequency-response magnitude and phase data. This data-analysis technique had been used successfully on other flight-test data, notably for XV-15 handling qualities (refs. 7 and 8). The success of the flight-test program reported here shows that aeroelastic modes can be efficiently and reliably identified by frequency-domain techniques, and such techniques can now be routinely used to support flight tests of the new composite blades.

Early results of the frequency-domain analysis were reported in reference 9, along with the original mode predictions. The flight-test data-analysis technique and the predictive programs were subsequently revised, in some areas extensively. The updated results were summarized in reference 10, of which the current report is an expansion.

General overviews of XV-15 structural dynamics, including previous flight-test data, are given in references 11 and 12. It should be noted that the flight-test data discussed in the current report are all for the original metal blades and new steel hubs. References 11 and 12 give data for the metal blades and original titanium hubs.

This report is divided into discussions of the XV-15 aeroelastic modes and the flight-test techniques used to excite them; the analytical procedures used to extract modal frequencies and damping from flight-test data; plots and tables of the results, including frequency and damping versus airspeed; and comparisons with values predicted by both CAMRAD and ASAP. Appendix A tabulates the numerical results generated for all test points. Appendix B lists the instrumentation and associated data-processing setups used to generate all flight-test data reported herein.

The authors wish to thank the late L. G. Schroers for his long involvement and many contributions to the development of the XV-15 and for his generous and unwavering support of this work. The authors also wish to thank J. R. Gillman, then of the Boeing Helicopter Corporation, for providing upgrades to the CAMRAD model of the XV-15, and S. K. Yin of Bell Helicopter Textron for the ASAP predictions.

FLIGHT-TEST METHODS

The intent of the flight tests was to validate the frequency-domain mode-identification method and to map out the dominant aeroelastic modes (illustrated in figs. 2 and 3). This section gives a brief overview of the aeroelastic modes of interest and the experimental methods used to identify them.

The flight conditions flown are discussed in the section entitled Flight-Test Results. The individual test points are tabulated in appendix A.

Motivations

A summary of the causes of rotor/pylon instability is given in reference 3. The rotor, pylon, and wing constitute a dynamic system that oscillates in pitch when perturbed. Torsional flexing of the wing and pylon imposes a pitch rate on the rotor, resulting in a net in-plane rotor force. The accompanying torsional moment on the pylon acts in the same direction as the original motion; it is, in effect, a negative spring. Negative damping may also occur at low ratios of pylon pitch rate to rotor speed. The inertia of the pylon and the elastic restraint of the wing cause oscillatory motion, which under some circumstances can become unstable.

The six most important wing/pylon aeroelastic modes for the XV-15 are illustrated in figure 3. Early predictions of damping versus airspeed, made by CAMRAD (ref. 13), are plotted in figure 4 for each mode. For certain combinations of altitude, rotor speed, and power, at least one mode became unstable (damping $\rightarrow 0$) at a sufficiently high airspeed. The predictions plotted in figure 4 represent an extreme case, based on the original aircraft design: titanium hubs with 2.5° of precone, 457 rpm (76% of the nominal 601 rpm), and a nominal zero-airspeed structural damping ratio of 0.01 for all wing/pylon modes. In

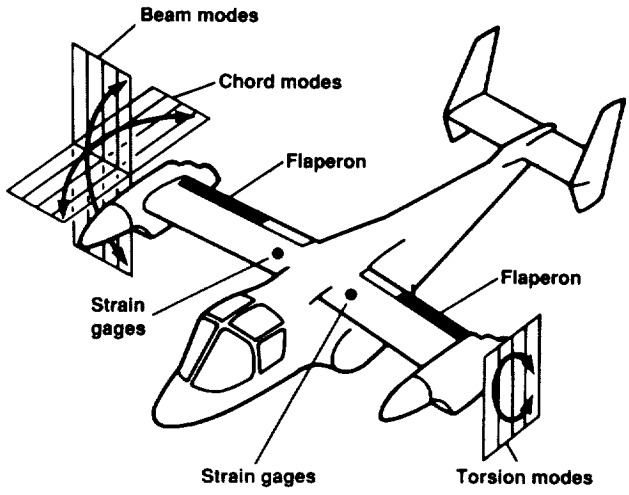

Figure 2. XV-15 aircraft, showing flaperons, strain gages, and wing modes.

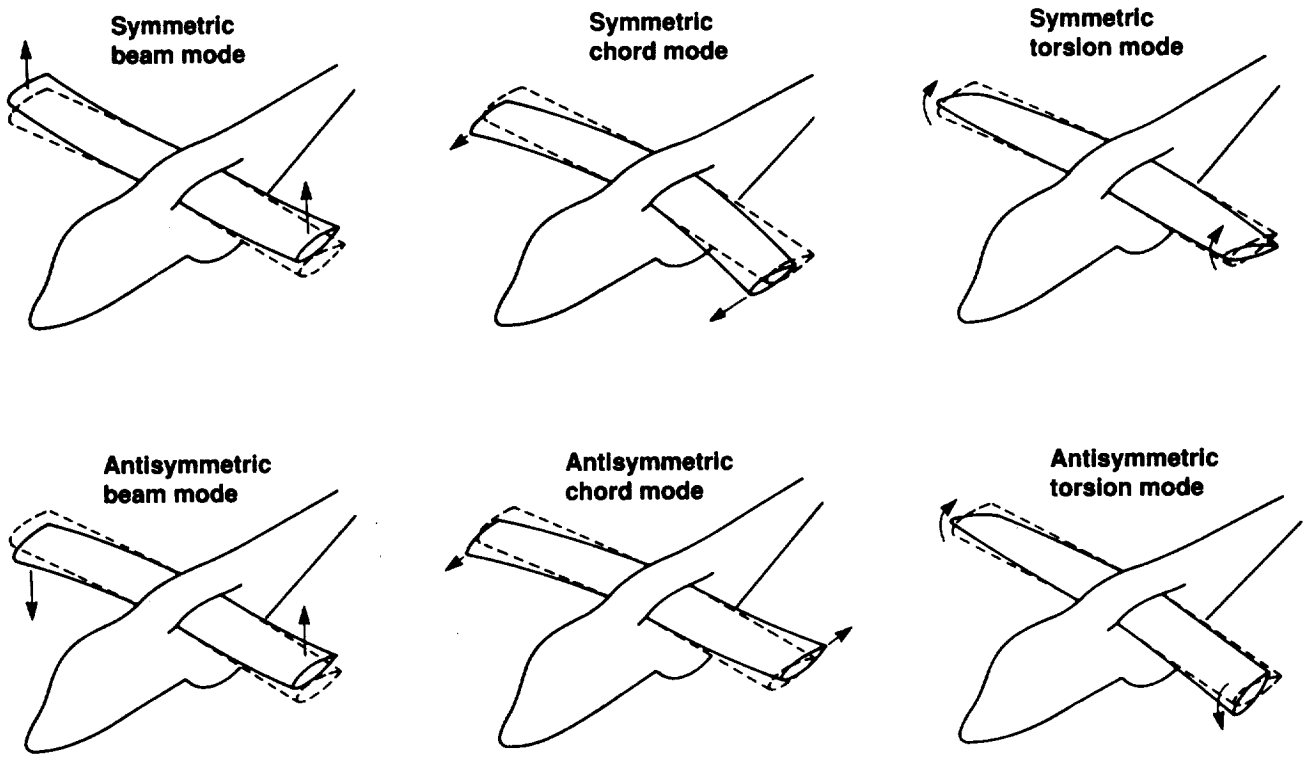

Figure 3. XV-15 aeroelastic wing modes, detail.

contrast, figure 5 shows the most recent CAMRAD predictions for the XV-15 configuration actually flown in the flight tests reported here: 1.5°-precone steel hubs, structural damping[1] based on full-scale wind-tunnel tests (ref. 14), rotor speed restricted to 86% of nominal speed, and maximum $C_p/\sigma_r = 0.046$ at 10,000 ft (the transmission torque limit at the nominal flight condition).

Maximum true airspeed at 10,000 ft is 260 knots, thus even the worst predicted stability margin (over 100 KTAS) is adequate, and the revised predictions show no instability at all. However, the large differences between figures 4 and 5 show that the stability margin can be sensitive to seemingly small changes in the model or flight conditions. It is not merely the airspeed for which instability is predicted that matters; for flight test, the rate at which instability is approached is also important. In the early predictions (fig. 4), the symmetric chord and antisymmetric beam modes show damping decreasing rapidly with increasing airspeed above 300 KTAS; hence relatively small errors in the analytical model could translate into large errors in the actual airspeed margins.

Except for the symmetric beam mode, the frequencies of all modes lie within about 2 Hz of each other; two frequencies—those of the antisymmetric chord and antisymmetric torsion modes—are within 0.1 Hz of each other at low airspeeds. Also, the frequency of the symmetric torsion mode lies within the design rotor-speed range. The possibility of a rapid decrease in stability with increasing airspeed makes precise identification of individual modes necessary, and the modes' close placement in frequency makes such identification difficult. Moreover, the exponential-decay method used in early XV-15 flight tests to estimate damping produced results that in some cases had scatter that was a large fraction of the predicted damping, as will be shown later in this report.

Accordingly, the development of an improved in-flight method of determining aeroelastic stability had high priority. The frequency-domain method showed the greatest promise of improved accuracy. Compared to the exponential-decay method, it also promised to reduce the flight-test time required for mode identification.

Previous Investigations

In previous flight tests (refs. 11 and 12), frequency and damping were measured using primarily the exponential-decay technique. The right-hand flaperon (fig. 2) was oscillated at a fixed frequency to drive a selected structural mode at resonance and was then

[1]See the Flight Test Results section for a table and discussion of structural damping assumptions.

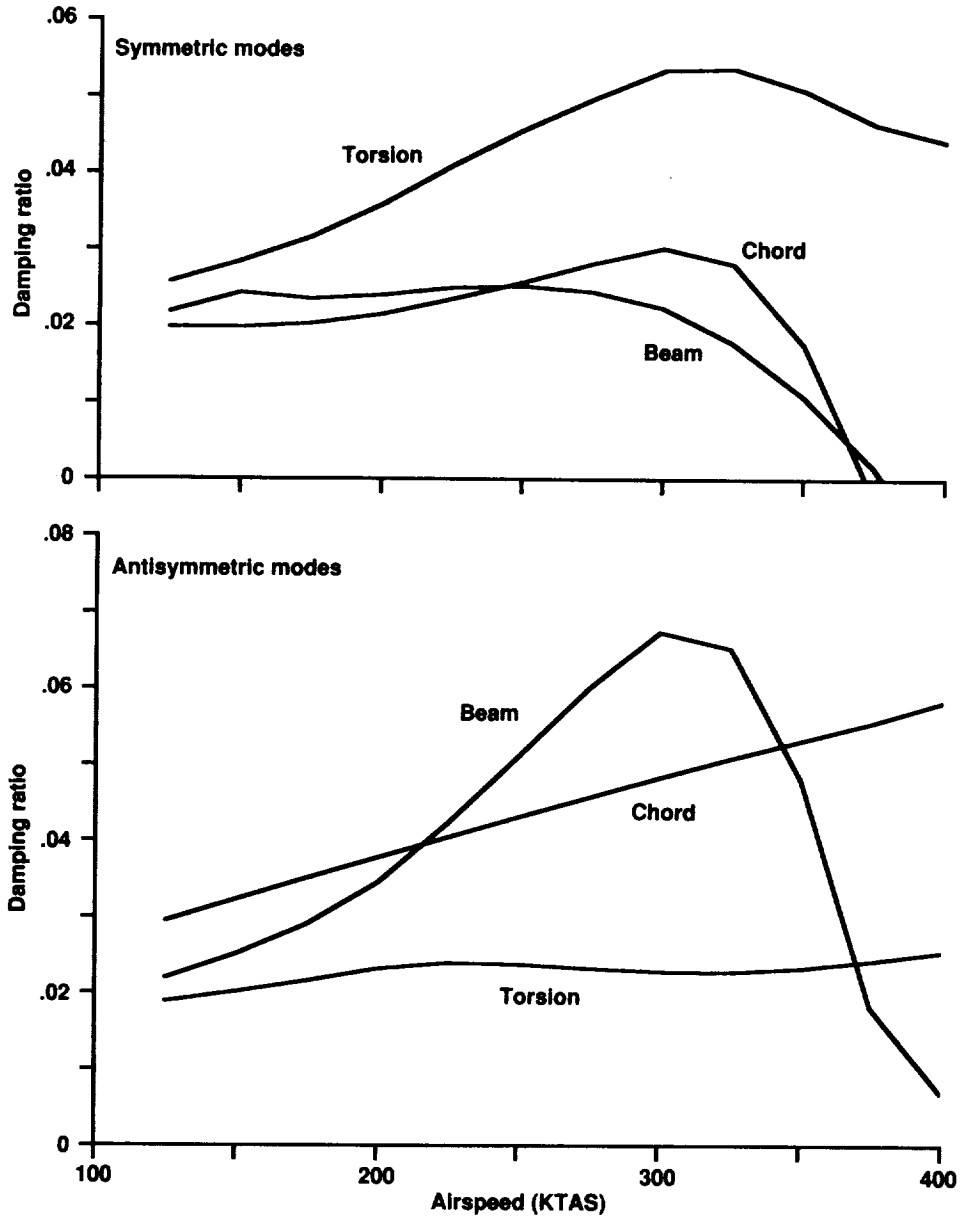

Figure 4. CAMRAD damping predictions for original XV-15 design: 2.5°-precone titanium hubs, nominal structural damping, 76% rotor speed at sea level, no torque limit.

abruptly turned off; the rate of exponential decay was a function of the modal damping. The right-hand rotor collective control was similarly used to excite the chord modes. Frequency-sweep inputs and natural-turbulence excitation were also tried. In additional flight tests (ref. 7), frequency-domain analysis was used to identify frequencies and damping from turbulence-excitation data.

Reference 11 lists the pros and cons of the different flight-test techniques for acquiring aeroelastics data. Reference 15 discusses the errors of the analytical methods associated with the testing techniques listed in reference 11. The results of using these methods during earlier flight-test programs may be summarized as follows:

1. The exponential-decay method yielded a great deal of scatter in the damping estimates, especially where neighboring modes were grouped closely together (ref. 11).

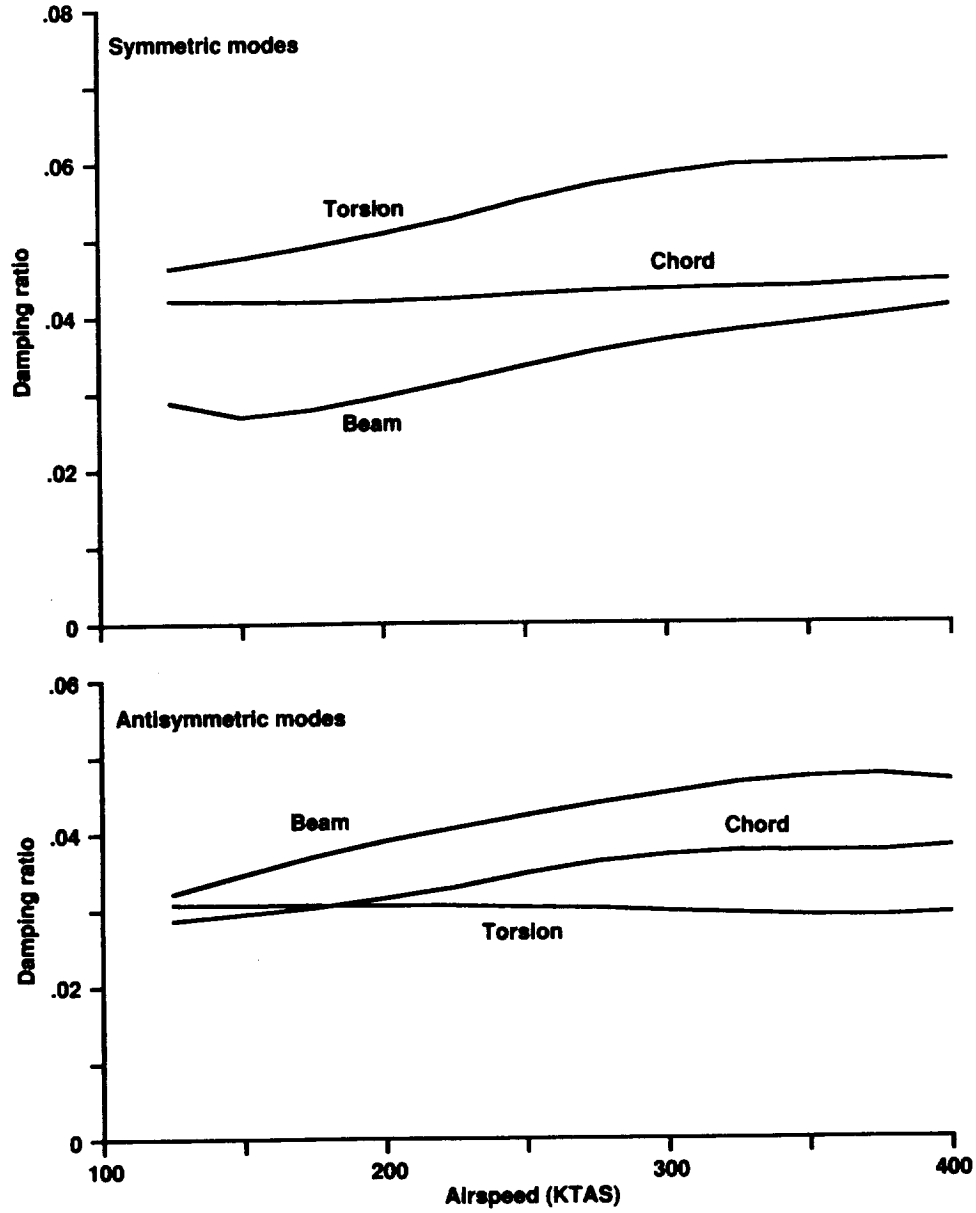

Figure 5. CAMRAD damping predictions for XV-15 as flown: 1.5°-precone steel hubs, empirical structural damping, 86% rotor speed at 10,000 ft, maximum $C_p/\sigma_r = 0.046$.

2. Turbulence excitation with random-decrement analysis produced results that agreed closely with those of the exponential-decay method but also showed considerable scatter. However, not all modes could be identified because of insufficient turbulence levels (ref. 12).

3. Frequency sweeps with single flaperon and collective exciters were generally unsuccessful, largely because the original exciter installation was unable to adequately excite the modes (ref. 12). The data were processed with an inverse fast Fourier transform (FFT) followed by an exponential-decay analysis, and were also analyzed with Kalman-filter techniques.

4. Turbulence excitation with the frequency-domain analysis of reference 16 (cross-spectrum integration) occasionally yielded good results, but the existing turbulence did not excite the modes strongly enough for the technique to work in most cases (ref. 7).

In nearly all cases, the natural frequencies were precisely identified, but the scatter in the damping values

indicated that a better method was needed. The results given in reference 7 indicated that the frequency-domain method was the most promising approach, provided that an improved means of exciting the structure could be devised. To this end, an exciter was added to the left flaperon so that the flaperons could be used together to selectively excite the symmetric and antisymmetric modes, as recommended in reference 11.

Four frequency-domain mode-identification methods were then tested with new flight data: (1) curve-fitting to frequency responses, (2) curve-fitting to cross-spectra, (3) integrating frequency-response magnitude data, and (4) integrating cross-spectra. The cross-spectra were computed from output data only; the integration method is discussed in reference 16. The final choice of method 1 was based on the scatter in estimating the damping ratio ζ and the natural frequency f_n at the baseline point (defined in Flight-Test Results). The results made it clear that simultaneously curve-fitting frequency response gain and phase was a superior method overall.

Early results of the application of frequency-domain techniques to XV-15 aeroelastics were reported in reference 9. That effort included the method of curve-fitting the cross-spectra between the left and right strain-gage output data; this proved useful for analyzing the chord modes. Since then, improvements have been made to the flight-test data analysis, including refinements of the transducer signal processing and of the associated sum-and-difference procedures that are used on the time-history data. These improvements permitted frequency responses to be used exclusively for all modes.

Wing-mounted strain gages provided data that proved adequate for good mode identification. Pylon-mounted accelerometers were also used, but their data were never better, and were often much worse, than strain-gage data. This may have been caused by the particular accelerometer installation on the XV-15 during the flight tests and should not be taken to mean that accelerometer data are inherently worse than strain-gage data or that the wing is a better location than the pylon for such measurements.

Frequency-Sweep Modal Excitation

Previous flight tests (ref. 11) used a high-frequency, limited-authority servo actuator in series with the right flaperon-control linkage to excite the beam and torsion modes, and a similar actuator in series with the right rotor collective control to excite the chord modes. Adding flaperon and collective excitation to the left wing allowed the symmetric and antisymmetric modes to be separately excited more easily. Symmetric modes were excited by driving the flaperons in phase; antisymmetric modes were excited by driving the flaperons in opposite phase. Furthermore, the paired flaperon exciters adequately excited the chord modes without using the collective exciters, considerably simplifying the flight tests.

Flaperon motion was measured by linear variable differential transformers (LVDT) on the flaperon control linkages; wing responses were measured by separate beam, chord, and torsion strain gages at the wing roots. Data from corresponding left and right transducers were summed or differenced, depending on the mode, to form composite inputs and outputs. When the two transducers were properly chosen, the structural signals were highly correlated and in phase for symmetric modes, and highly correlated but reversed in phase for antisymmetric modes. Noise was not correlated, thereby minimizing corruption of the spectral data.

An electronic controller automatically swept the flaperons from 1 to 10 Hz. Figure 6(a) shows the sum of the LVDT outputs for the two flaperons for one symmetric sweep. For an antisymmetric sweep, the difference between the LVDT outputs would yield an identical plot except for phase reversal. At least three sweeps in succession were performed at each test condition, and all results reported here are based on three sweeps. For clarity, however, only one sweep is shown in figure 6 (and in related figures 7–12).

The controller used a logarithmically increasing sweep rate of approximately ten cycles per octave (the sweep rate was proportional to frequency). It took about 23 sec to complete a sweep. Although this was considerably faster than the rate preferred for a full-magnitude response, it proved slow enough to adequately excite all of the modes, and it allowed the pilot to hold a steady flight condition without an excessive work load.

The decrease in flaperon oscillation amplitude with time, and hence with increasing frequency, resulted from limited flaperon-actuator frequency response. This effect was compensated for during the frequency-response calculations (described in the next section, Analysis Methods).

If the excitations, instrumentation, and signal processing were perfect, the antisymmetric content of a symmetric sweep (that is, the difference between the flaperon signals) would be exactly zero. For the symmetric sweep of figure 6, the symmetric content (fig. 6(a)) had, in fact, a magnitude about 20 times greater than the residual antisymmetic content (fig. 6(b)). The full-magnitude part of the sweep (at the beginning) was over 40 times greater than the noise at the start of the data record, before the sweep began. These comparisons were based on root-mean-square (rms) deviations from the mean values.

Representative responses to symmetric excitation are shown in figures 7–9 and to antisymmetric excitation in figures 10–12. The vertical scales were varied to best display each mode. All responses were outputs of strain

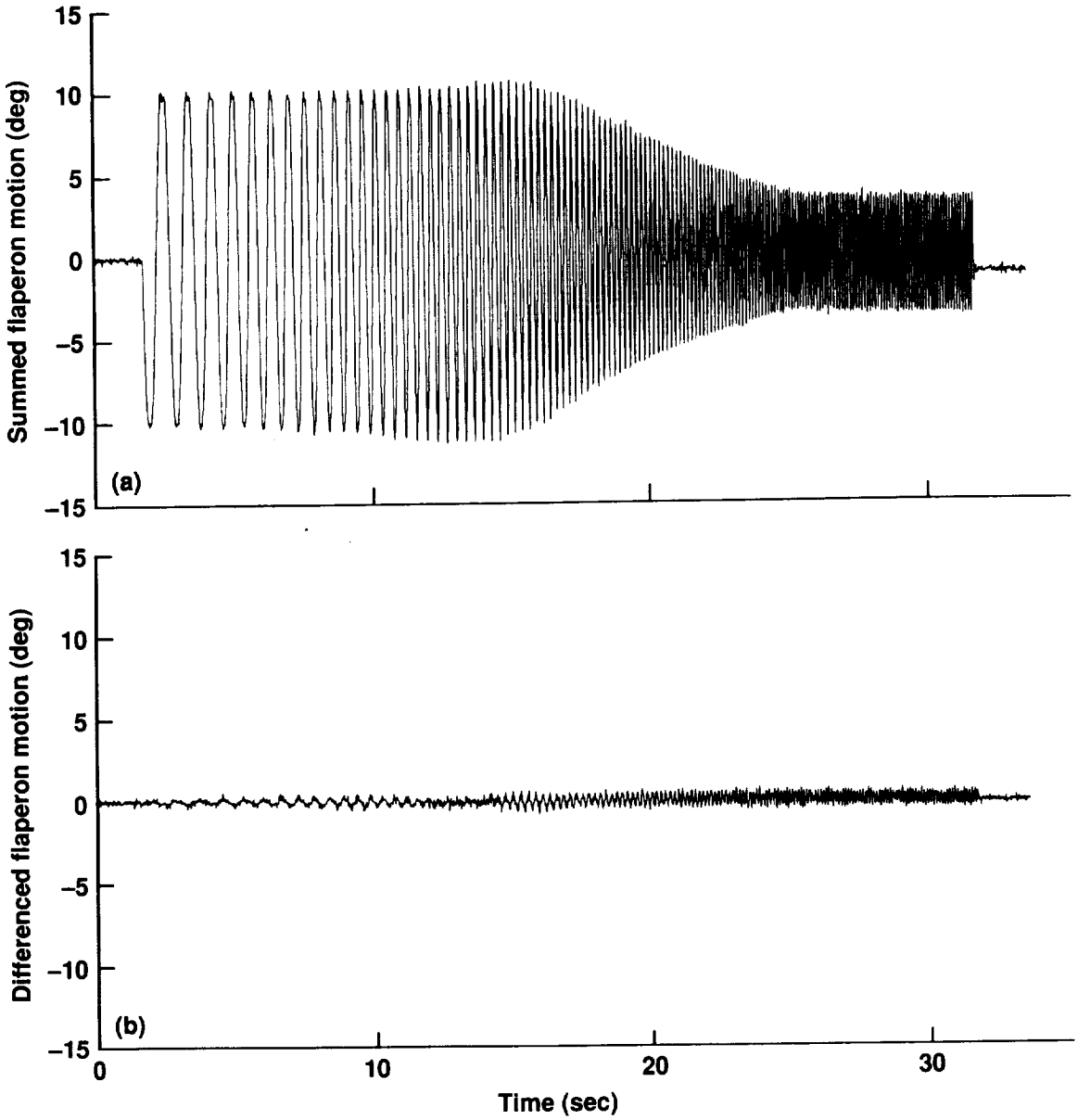

Figure 6. Flaperon time histories for one symmetric sweep. (a) Summed, (b) differenced.

gages mounted on the wings and were plotted as time histories. Left and right strain-gage outputs were summed for symmetric sweeps and differenced for antisymmetric sweeps.

The controller did not shut off automatically at the end of each sweep, so there were a few extra seconds of excitation at a steady 10 Hz, as can be seen in figure 6(a). The extra oscillations were outside the range of the peak modal frequencies and did not affect the analyses discussed in this report. Also, the recorded time histories included a few seconds of data both before and after the sweeps. For the symmetric sweep and corresponding responses in figures 6–9, there are about 2 sec of noise before the excitation begins and about 4 sec after it ends. The antisymmetric sweep (not shown; it is identical to fig. 6(a) but reversed in phase) that excited the responses in figures 10–12 began at about 2 sec and stopped at 33 sec. The effects of noise are discussed in detail in the section Sweep Parameters.

By far the clearest response is seen for the symmetric beam mode (fig. 7); perhaps the weakest is for symmetric torsion, for which a barely visible response is seen at

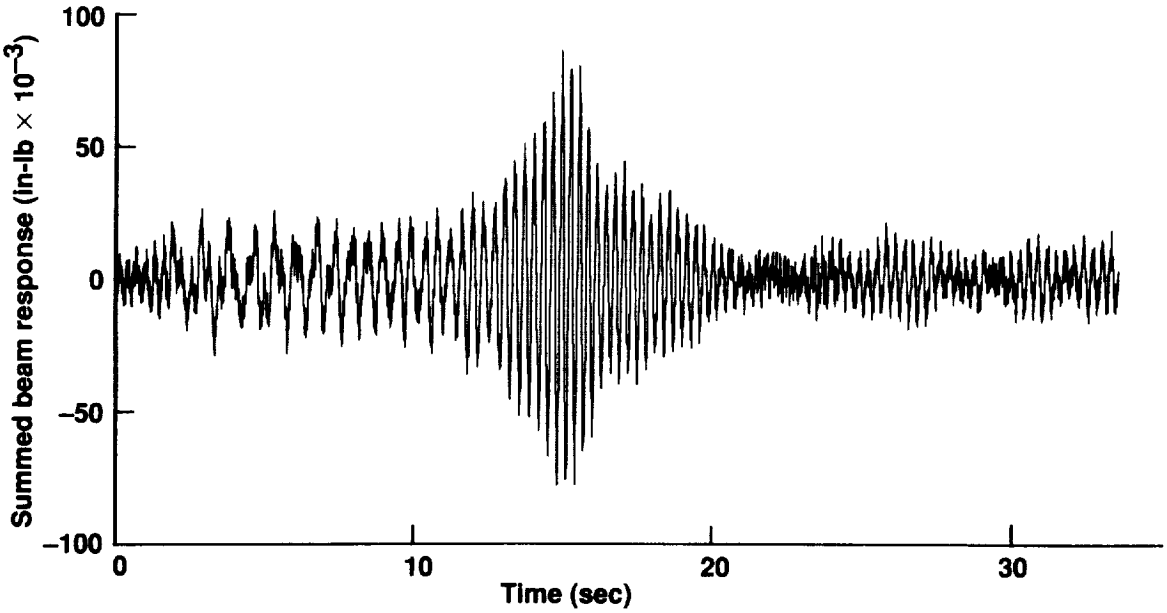

Figure 7. Beam strain-gage response to a symmetric sweep.

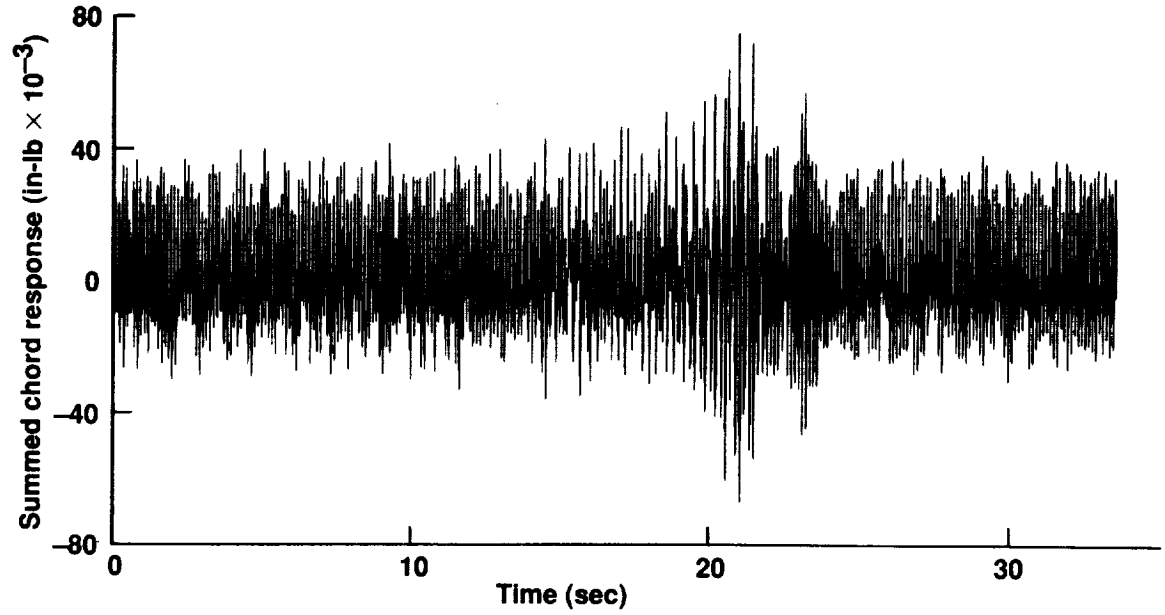

Figure 8. Chord strain-gage response to a symmetric sweep.

about 23 sec (fig. 9). Symmetric chord has a mild response at 21 sec (fig. 8). All antisymmetric modes show responses near 22.5 sec: antisymmetric beam has a predominant response at 20 sec (fig. 10), and antisymmetric chord shows a broad response that starts at 21 sec (fig. 11) and continues through the antisymmetric torsion mode at 22.5 sec (fig. 12). The frequency-domain method was able to distinguish between these two modes at the same frequency, as discussed in the section Individual Modes.

Sweep Parameters

Four parameters can be adjusted for flaperon frequency sweeps: amplitude, relative phase, sweep rate, and

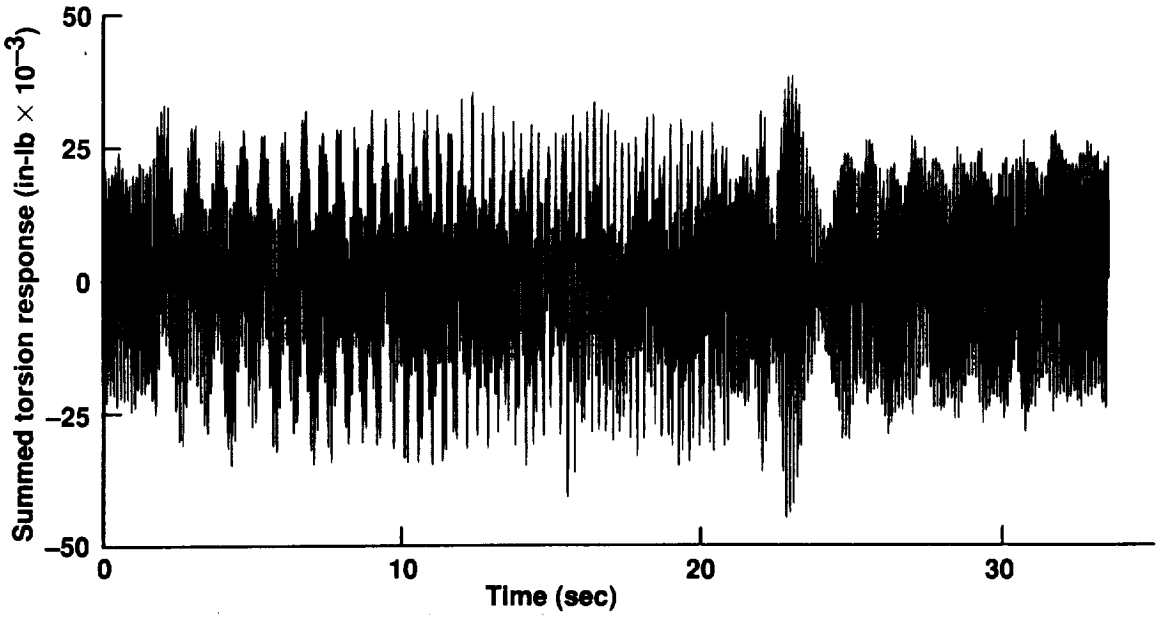

Figure 9. Torsion strain-gage response to a symmetric sweep.

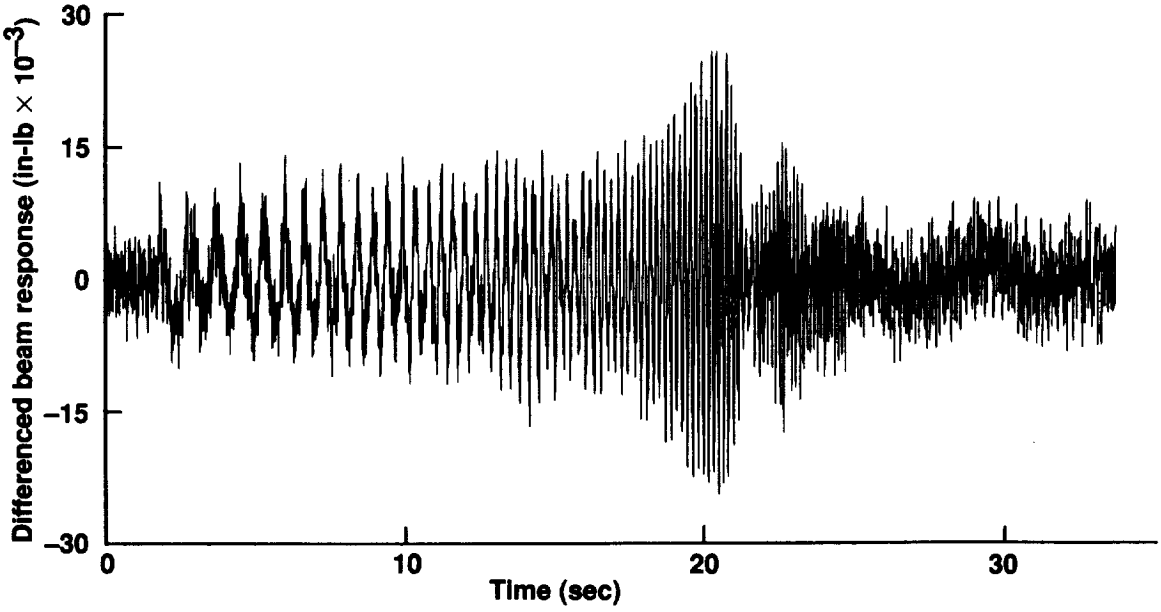

Figure 10. Beam strain-gage response to an antisymmetric sweep.

number of sweeps. (In principle, initial phase can also be varied, but this has no influence on frequency-domain analysis.) Ideally, many very slow sweeps would be run at each test point, all at high amplitude. However, it is necessary to minimize flight-test time. The initial choice of three 23-sec sweeps was a compromise between adequate mode identification and minimum flight time.

The lower the modal frequency and damping, the longer it takes for an excited mode to decay. On the XV-15, the lowest frequency and damping both occur for the same mode (the symmetric beam mode). Therefore, the sweeps were always run from low to high frequency so that residual low-frequency data could be acquired while sweeping through the high-frequency modes. This

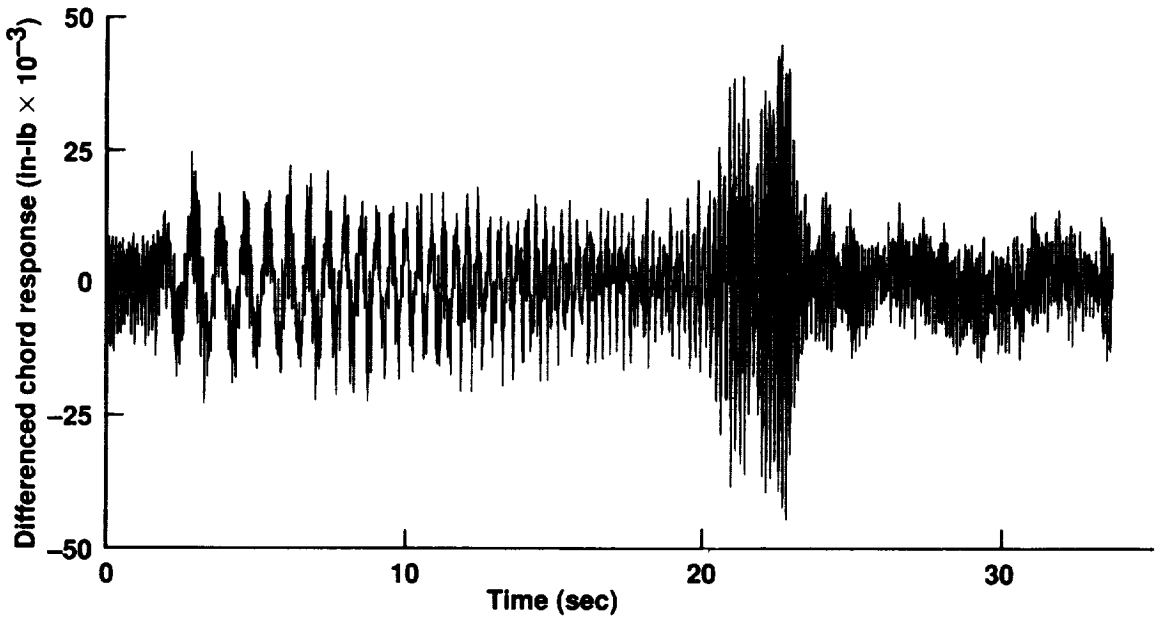

Figure 11. Chord strain-gage response to an antisymmetric sweep.

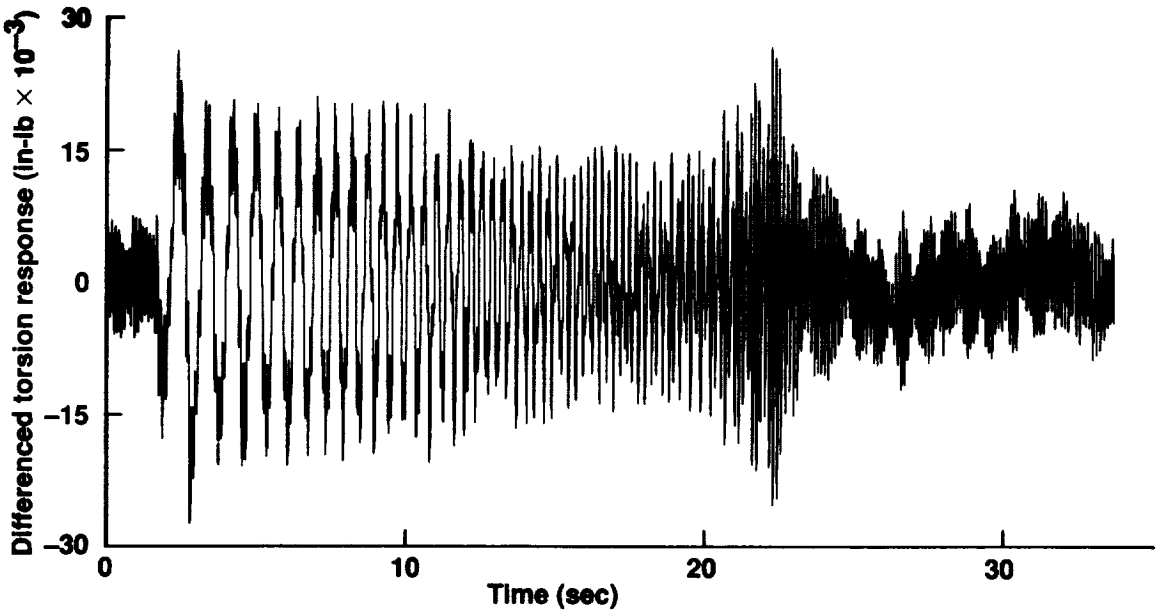

Figure 12. Torsion strain-gage response to an antisymmetric sweep.

procedure maximized the efficiency of the frequency-sweep method.

Since sweep amplitude does not affect the flight time, it was set at 100%, or ±5° of flaperon travel, for all sweeps analyzed for this report. A few preliminary sweeps were tried with lower amplitudes; as expected, full amplitude gave the best excitation, there being no problems with saturation. However, vibratory airframe loads were high, especially for the 98%-rotor-speed test conditions, so full amplitude may not be usable for all future work.

A fundamental problem is that both the number of sweeps and the sweep rate have nonlinear effects on the accuracy of mode identification. As the sweep rate is reduced, the spectral amplitude and the signal-to-noise ratio asymptotically approach their maximum values.

Progressively larger increases in flight time are needed to obtain even minor improvements in accuracy. Eventually it becomes more valuable, for a given amount of flight time, to have more sweeps than to have slower sweeps, although the accuracy increases only as the square root of the number of sweeps (discussed in detail under Error Analysis). For example, changing from 3 to 5 sweeps would reduce the random error by 23%, but no fewer than 12 sweeps would be required for a 50% improvement.

A further problem is that the true values of the modal parameters are not precisely known (they can only be estimated from flight data), thus there is no way of knowing in advance how close to the optimum values the initial values of the sweep parameters are. The maximum sweep rate that allows two closely spaced modes to be identified was derived in reference 17 to be approximately

$$V = 2\pi\zeta f_n \Delta f \quad \text{Hz/sec} \tag{1}$$

where V is the sweep rate, Δf is the frequency separation of the modes, and ζ and f_n are the damping ratio and natural frequency of the worst-case (lowest damped) mode. This implies a logarithmic sweep, with a minimum time per decade (Hz) of

$$\int_1^{10} \frac{df}{V} = \frac{\ln 10}{2\pi\zeta\Delta f} \quad \text{sec} \tag{2}$$

The most difficult modes to differentiate would seem, from table A1 in appendix A, to be the antisymmetric chord and antisymmetric torsion modes at low airspeeds; their exact coincidence would in principle dictate an extremely long sweep. Fortunately, the chord and torsion modes were measured by different strain gages, which had sufficiently low crosstalk to allow use of a reasonably fast sweep. The closest modes measured by the same strain gages were the two torsion modes; the sweep rate was much more important in this case. Assuming a minimum damping value of 0.04 and a frequency separation of 0.8 Hz, equation (2) yields a minimum sweep time of 11 sec/decade (Hz), half of that actually used. Considerably longer sweeps are necessary for full modal response; 95% magnitude requires a sweep about three times longer than that implied by equation (2). Nevertheless, the 23-sec sweep time proved slow enough to reveal all individual modes, and no attempts to refine the sweep parameters were made. The sum-and-difference data processing further reduced interference between closely spaced modes.

ANALYSIS METHODS

The overall concept of the mode identification method used in this study is first to estimate the (nonparametric) structural frequency response $H(f)$ stimulated by aircraft excitation, and then to determine the (parametric) modal damping and frequency values by fitting a second-order curve to the frequency response. With the exception of simple summing and differencing operations on the raw time-history data and a digital anti-jitter filter, all analyses were carried out in the frequency domain.

The following sections discuss the reasons for frequency-domain analysis of XV-15 aeroelastics data, outline the different steps in the analysis, and present details of the computational steps implemented in the analysis. Complete examples are given for the symmetric wing beam mode; key results are given for other modes. See appendix A for numerical tabulations of the identified modal parameters.

Advantages of the Frequency-Domain Method

The frequency-domain method has a number of characteristics that make it well suited for the identification of aeroelastic modes. The frequency-response calculation in which the cross-spectrum is divided by the input autospectrum eliminates the effects of uncorrelated noise (details are given in the General Approach section). In contrast, the results of analogous time-domain ("output-error") methods are biased by the presence of process noise (e.g., turbulence)—a key consideration when the level of direct modal excitation is small. In particular, the exponential-decay method, which uses the output only, gives results biased by both process and measurement noise. This characteristic leads to significantly worse scatter in the exponential-decay results than in the frequency-domain results.

A second feature of the frequency-domain method is that individual modes are isolated and identified by fitting curves to the frequency response within a narrow frequency band. This is important when the aeroelastic modes are closely spaced, as in the XV-15. When modes are too close to be treated separately, multiple-mode identification can be performed. In contrast, time-domain methods such as exponential decay cannot separate the modes; either all modes must be identified together, or neighboring modes must be ignored. Either approach can lead to significant errors.

A final key aspect of the frequency-domain method is the availability of the coherence function. This function allows a direct measure of the level of modal excitation, the level of random error, and the signal-to-noise ratio.

General Approach

Figure 13 illustrates the signals and noise affecting the analysis. The actual input $x(t)$ is corrupted by input measurement noise $n_i(t)$, giving a measured input $x_m(t)$, and the measured response $y_m(t)$ is corrupted by output measurement noise $n_o(t)$. Added to the true input is the unmeasurable input (process noise) $n_p(t)$. If the measurable and unmeasurable inputs and the output measurement noise are not fully correlated, then the frequency response $H(f)$ may be estimated without bias from the cross- and autospectral functions $G_{x_m y_m}(f)$ and $G_{x_m x_m}(f)$ as

$$\hat{H}(f) = \frac{G_{xy}(f)}{G_{xx}(f)} \tag{3}$$

(For simplicity, the m subscripts are omitted here and in the remainder of the Analysis Methods section.)

Although both the numerator and denominator of equation (3) are correlated with the measured input $x_m(t)$, the unmeasurable input $n_p(t)$ and the output measurement noise $n_o(t)$ are not correlated with $x_m(t)$, so they do not corrupt the calculation of $\hat{H}(f)$. Unmeasurable inputs $n_p(t)$ do contribute to the measured output $y_m(t)$, but not to $x_m(t)$, hence they do not bias $G_{xy}(f)$. Two examples of unmeasurable inputs are turbulence (which could also be reflected to the output and treated as an output noise source) and motion of the pilots' controls during the frequency sweep. Output measurement noise comprises primarily instrumentation noise in the strain-gage signals. Only input measurement noise $n_i(t)$, such as errors in measuring the flaperon motion, causes a bias in the frequency-response calculation of equation (3). In general, however, input measurement errors are small relative to unmeasurable inputs and output measurement errors, so equation (3) is the optimum method (ref. 18).

The estimated frequency response $\hat{H}(f)$ may be fitted with a second-order model of the form

$$H_M(f) = \frac{A}{1-(f/f_n)^2 + i2\zeta f/f_n} \tag{4}$$

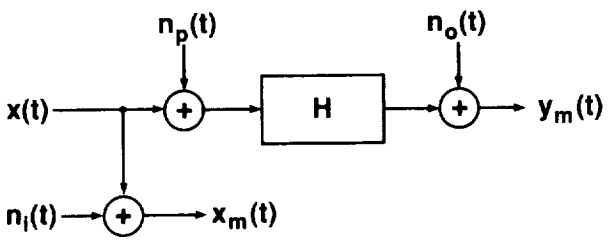

Figure 13. Signals and noise affecting frequency-response calculations.

The parameters A, f_n, and ζ are iteratively varied to get the best fit to the frequency response; the parameters f_n and ζ are the natural frequency and the damping ratio, whose values are desired.

Figure 14 schematically shows the procedures used to conduct the analyses. Each large block corresponds to a separate computer program. After each flight, the flaperon sweeps (input data) and the modal responses (output data) were loaded into the Tilt-Rotor Engineering Database System (TRENDS) for general error-checking and ease of subsequent access. Next, the Frequency Response Identification (FRESPID) program generated the spectral functions from the time histories in TRENDS. Finally, the modal parameters were determined by using the curve-fitting program NAVFIT. All computations were performed postflight.

TRENDS was developed by M. J. Bondi of NASA Ames Research Center and W. S. Bjorkman of Analytical Mechanics Associates, Inc. (ref. 19). FRESPID was written by M. B. Tischler and J. G. M. Leung of Ames Research Center, and NAVFIT was originally developed at McDonnell Douglas Aircraft (ref. 20). The discussions of FRESPID and NAVFIT given below are based on those in reference 8. Both programs are part of the Comprehensive Identification from FrEquency Responses (CIFER) system (ref. 21).

FRESPID Computations

Figure 15 shows the computational procedures used in FRESPID to generate the auto- and cross-spectral functions from selected input and output time histories. First the dc components and linear drifts are removed to prevent oscillation in the spectral calculation. Multiple runs are then concatenated to form composite input and output time histories, and simple data adjustments such as scale factors and signal summation may be applied. The concatenated and adjusted time histories are digitally filtered, then partitioned into K sections of L discrete data points. Each section overlaps the preceding one by 50%, increasing the number of averages by $K - 1$. The sections are then windowed to prevent side lobes and leakage. The spectral content of each section is analyzed using the chirp z-transform. The total spectrum is finally determined from a linear average of the spectra over the K sections.

After the Fourier coefficients have been computed, the auto- and cross-spectral functions $G_{xx}(f)$, $G_{yy}(f)$, and $G_{xy}(f)$ and the frequency response $H(f)$ are calculated by the formulas in reference 18. The coherence function $\gamma^2_{xy}(f)$ is also computed. (Equations are given in the section Spectral Functions.)

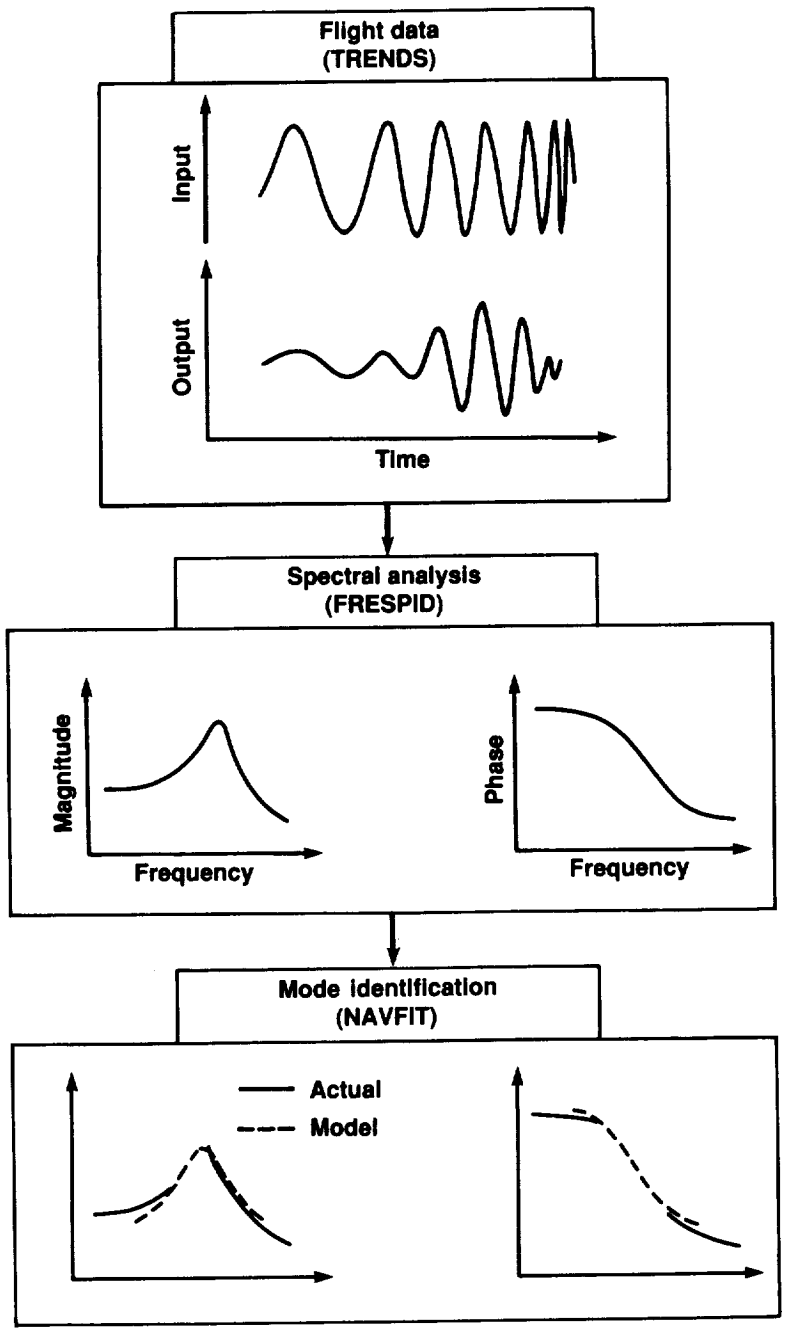

Figure 14. Data processing for frequency-domain mode identification.

The following sections describe various details of the procedure.

Sum-and-difference procedure– If the input or output time histories are available as paired data streams that are outputs of transducers making similar measurements, sum-and-difference preprocessing may be appropriate. The matched beam, chord, and torsion strain gages on the left and right wings meet these criteria, as do the flaperon LVDTs. If the excitation is symmetric, then the structural signals will be highly correlated and in phase for symmetric modes, and highly correlated but out of phase for antisymmetric modes. The left and right flaperon signals are always so correlated. Adding the left- and right-hand signals together tends to cancel out the antisymmetric content, thereby suppressing antisymmetric modes in the spectra. Subtracting paired signals likewise suppresses symmetric modes for antisymmetric excitation.

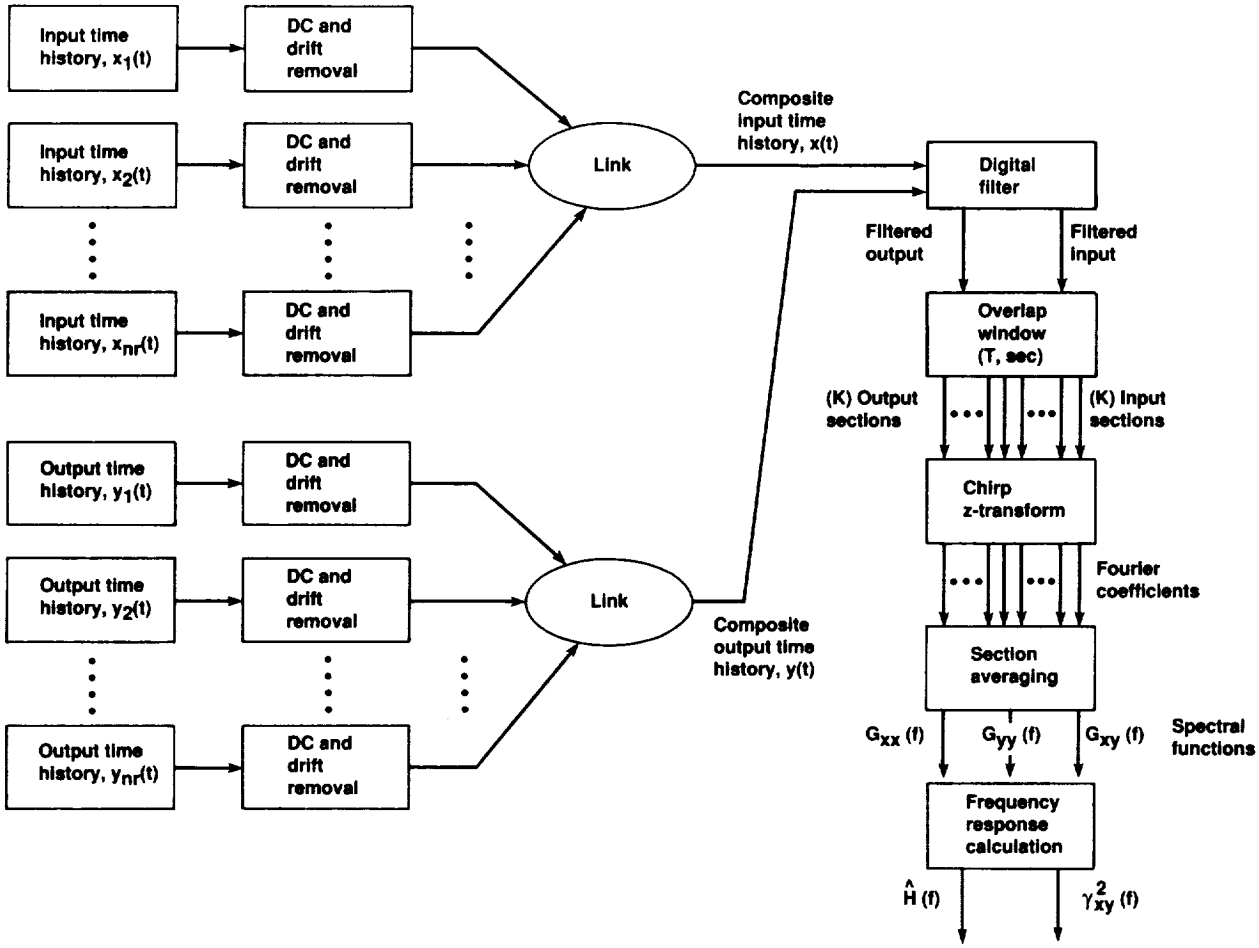

Figure 15. Flow chart of computations performed by the FRESPID program.

An example of the sum-and-difference procedure is shown in figure 6. It should be noted that this operation does not improve the fundamental signal-to-noise ratio; both the desired signal and the random noise are doubled. Improvements obtained in the spectra are generally not visible in the time histories, where random noise is much more apparent to the eye than the unwanted modal responses.

All results reported here are based on left-right pairs of similar transducers: LVDTs for inputs, and strain gages for outputs. The best correlation for the desired modal responses and the best rejection of unwanted modes occur when the transducers are closely matched to each other.

Windowing and filtering– Choosing the proper section size L is an important step in applying the frequency-domain method. Given a fixed record length and sample rate, a compromise must be made between good smoothing and high resolution (ref. 22). Short sections give the most averaging, hence the best smoothing out of noise; long sections give more low-frequency information. The sections used here overlapped each other by 50%. Overlapped sections made more efficient use of the data at the edges of the sections, thereby creating less spectral bias and variance than non-overlapped sections (refs. 18 and 23).

The preferred input section size for the aeroelastics study was 1792 points. At the nominal sample rate of 125.5/sec, each section was about 14 sec long—just over half a sweep. Because of overlaps, the usual three sweeps produced at least 9 sections, which were enough to yield low errors (see Error Analysis). Each section was scaled with a squared-cosine weighting function (Hanning window) (see refs. 23 and 24 for detailed discussions of windows).

The output always comprised 256 frequency points. The widest frequency range was 40 rad/sec (for the anti-symmetric beam mode and the symmetric torsion mode), giving a worst-case frequency resolution ($1/2\ \Delta\omega$) of 0.0781 rad/sec, or 0.0124 Hz. The output resolution of FRESPID was always better than the input resolution of

NAVFIT (see Curve-Fit Parameters), which ensured that the FRESPID output itself imposed no resolution limits on the curve fits.

An important reason for windowing is the reduction of leakage, or the appearance of incorrect frequency components in the spectra (ref. 22; see also refs. 18, 23, and 24). This is particularly important for swept signals. Because the signals never remain at a particular frequency for an extended period, the correlation functions (which underlie the spectral functions defined in the section Spectral Functions) tend to underestimate the actual magnitudes; the spectral energy "leaks" out. Proper use of windows can minimize the problem. Furthermore, the curve-fitting routine depends only on the overall shapes of the responses (the relative spectral values), not on the absolute magnitudes. Small errors in the peak magnitude caused by windowing are much less troublesome than false data (sidelobes) at other frequencies.

All time-history data were filtered with an optimal linear phase finite impulse response (FIR) digital filter designed by J. G. M. Leung, who used the bandpass algorithm given in reference 25. The cutoff frequency was 31.375 Hz (197 rad/sec), which is 1/2 the Nyquist frequency. The filter eliminated the jitter (digital noise) arising from asynchronous sampling of the signals; jitter can cause distortion in the calculated spectra.

Chirp z-transform– The chirp z-transform (ref. 25) is an efficient method for evaluating the z-transform of a time history along specific contours in the z-plane. When the contour is a unit circle, the chirp z-transform is equivalent to the Fourier transform. When the contour is an arc subscribed by the angle ω_0 to ω_1 rad on a unit circle, the chirp z-transform gives the Fourier transform of the time history between the selected frequencies $\omega_0/2\pi$ and $\omega_1/2\pi$ Hz. Unlike the discrete Fourier transform and its conventional fast Fourier transform (FFT) implementations,[2] the chirp z-transform permits arbitrary specification of frequency resolution and of minimum and maximum frequencies (up to the Nyquist frequency) with more accuracy than zero-padding. Thus, the chirp z-transform allows the extraction of high-resolution spectra in a narrow frequency band. This results in an increase in the identified dynamic range, especially at the low-frequency end, and excellent out-of-band rejection of the aliased components.

Most frequency-transform algorithms require that the number of samples and of frequencies be equal and be an integral power of two, whereas the chirp z-transform used for this analysis requires only that their sum be a power of two. Additional advantages of chirp z-transforms are discussed in reference 8.

Spectral functions– Let the measured input and output time histories $x_m(t)$ and $y_m(t)$ be segmented into K windowed sections, and for each section k let $X_k(f)$ and $Y_k(f)$ be the Fourier coefficients at frequency f. Then the two-sided band-limited spectral functions are given by the following equations (based on those in reference 18):

$$G_{xx}(f) = \frac{1}{KTU} \sum_{k=1}^{K} |X_k(f)|^2 \tag{5}$$

$$G_{yy}(f) = \frac{1}{KTU} \sum_{k=1}^{K} |Y_k(f)|^2 \tag{6}$$

$$G_{xy}(f) = \frac{1}{KTU} \sum_{k=1}^{K} X_k^*(f) Y_k(f) \tag{7}$$

where $G_{xx}(f)$, $G_{yy}(f)$, and $G_{xy}(f)$ are the discrete input, output, and cross-spectral functions, respectively, and * denotes the complex conjugate. In these equations, K is the number of overlapped time-history sections, U is the scale factor for the time-history window function, and T is the length of each section in seconds. For the Hanning windows used here, $U = \sqrt{8/3}$ (ref. 18).

Once the input, output, and cross-spectral estimates for a selected time-history pair have been determined, the input-to-output frequency response is calculated by

$$\hat{H}(f) = \frac{G_{xy}(f)}{G_{xx}(f)} \tag{3}$$

There are several different ways of estimating $H(f)$; reference 26 discusses the pros and cons of the most common ones. Equation (3) is the optimum method for XV-15 flight data.

For the following sections, the discrete frequency dependency (f) is omitted, but it is implied throughout. The frequency-response results are presented in modified Bode form, that is, plots of magnitude (dB) and phase (deg) versus frequency (Hz) (see Examples of Spectra). These quantities are determined from the complex-valued frequency response by

$$|H| = \sqrt{[\mathrm{Re}(H)]^2 + [\mathrm{Im}(H)]^2} \tag{8}$$

[2]That is, those algorithms based on the Cooley-Tukey method. The chirp z-transform algorithm used here has an FFT embedded within it.

$$|H|_{dB} = 20 \log_{10}|H| \tag{9}$$

$$\angle H = \tan^{-1}\frac{|\mathrm{Im}(H)|}{|\mathrm{Re}(H)|} \tag{10}$$

where Re(H) and Im(H) denote the real and imaginary parts of H. Note that the appropriate unit for spectral magnitude is power decibels; thus, for input autospectra

$$|G_{xx}|_{dB} = 10 \log_{10}|G_{xx}| \tag{11}$$

An analogous definition holds for the output autospectral and cross-spectral magnitudes. Frequency is plotted linearly, not logarithmically (the standard Bode form), because all frequency ranges of interest are considerably less than one decade.

In the context of nonlinear systems analysis, the result presented in equation (3) is a describing function since it describes the part of the output that can be linearly related to the input. A good indication of the quality of the linear model of the input-to-output dynamics is obtainable from the coherence function $\gamma^2_{xy}(f)$, defined by

$$\gamma^2_{xy}(f) = \frac{|G_{xy}|^2}{G_{xx}G_{yy}} \tag{12}$$

which may be interpreted as the fraction of the output spectrum that can be accounted for by a linear relation with the input spectrum (ref. 21). When the process under investigation is perfectly linear and the spectral estimates are noise free, the coherence function is unity for all frequencies within the input spectrum.

A common cause of reduction of the coherence function is nonrandom input and output noise. The random output noise components are eliminated by the frequency-response calculation of equation (3), and the random input noise components introduce only very small errors (see the Error Analysis section). However, nonrandom or correlated noise components can cause a significant drop in the coherence function. Significant improvements in the spectral results are obtained when multiple runs are concatenated, since the variance in the spectral estimates is inversely proportional to the number of time-history averages.

Examples of spectra– Figure 16 is an autospectrum plot of the flaperon motion; it corresponds to the time-history data shown in figure 6(a). The autospectrum G_{xx} reveals a drop in amplitude as frequency increases; the drop is caused by response limitations of the exciter servos. Since both the frequency-response and coherence are calculated as ratios, they are not affected by a varying sweep amplitude.

Figure 17 is the autospectrum plot for the symmetric beam output; it corresponds to figure 7. The output autospectrum G_{yy} clearly shows the peak of the first beam mode at 3.3 Hz. The cross-spectrum G_{xy} is plotted in figure 18. It is similar in shape to the autospectrum, but distorted by scaling effects. For ease of comparison, the vertical scales on all three magnitude plots, plus figure 19, cover a 40-dB range, with the minimum magnitudes adjusted as appropriate.

Figure 19 shows the frequency-response magnitude and phase for the symmetric beam response to flaperon input. Although the shape of the magnitude peak of the mode is similar to that of the output autospectrum G_{yy} (fig. 17), it is not identical because the input autospectrum G_{xx} is not precisely constant (fig. 16). The magnitude plot clearly shows the second-order response peak, and the phase plot shows the 90° change in phase at the natural frequency.

Figure 20 illustrates the coherence function $\gamma^2_{xy}(f)$ that corresponds to the frequency response shown in figure 19 for the symmetric beam mode. Reduced coherence above the natural frequency f_n was seen in all modes, especially near 1/rev (8.6 Hz at 86% rpm). Worse coherence was generally seen in the antisymmetric chord and

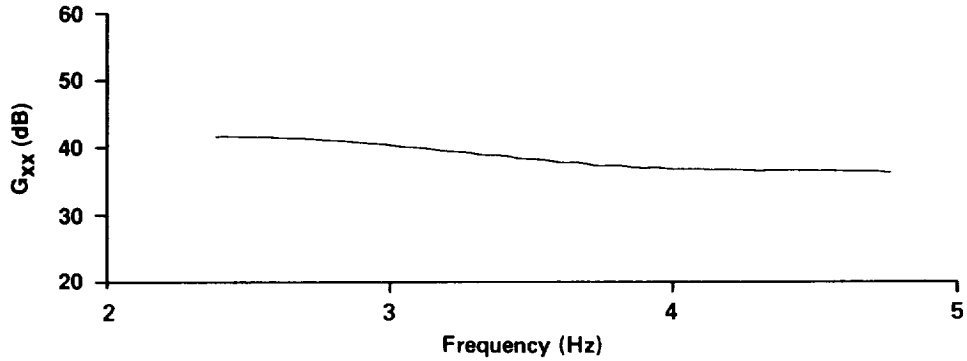

Figure 16. Autospectrum G_{xx} of the summed flaperon inputs for three symmetric sweeps.

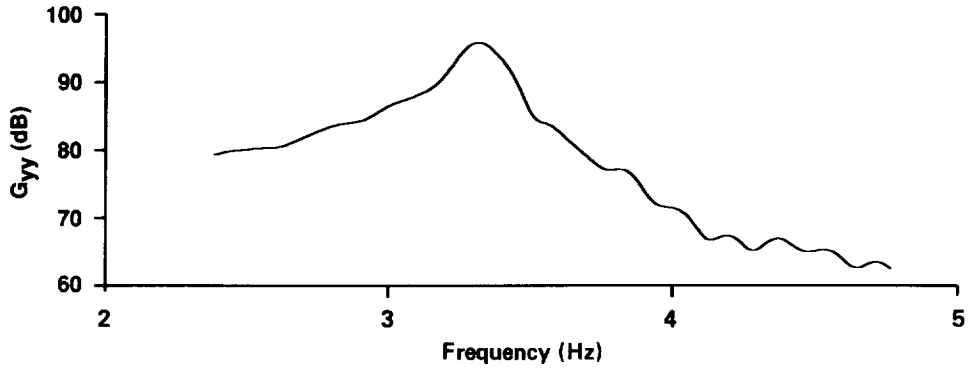

Figure 17. Autospectrum G_{yy} of the summed beam strain-gage responses for three symmetric sweeps.

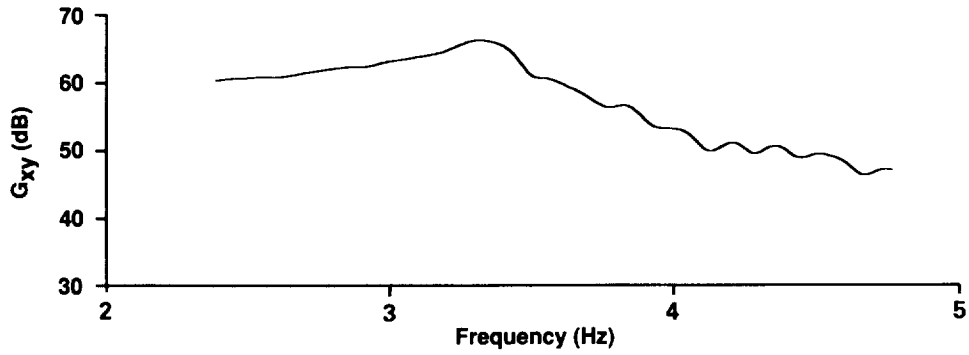

Figure 18. Cross-spectrum G_{xy} between the flaperon inputs and strain-gage outputs.

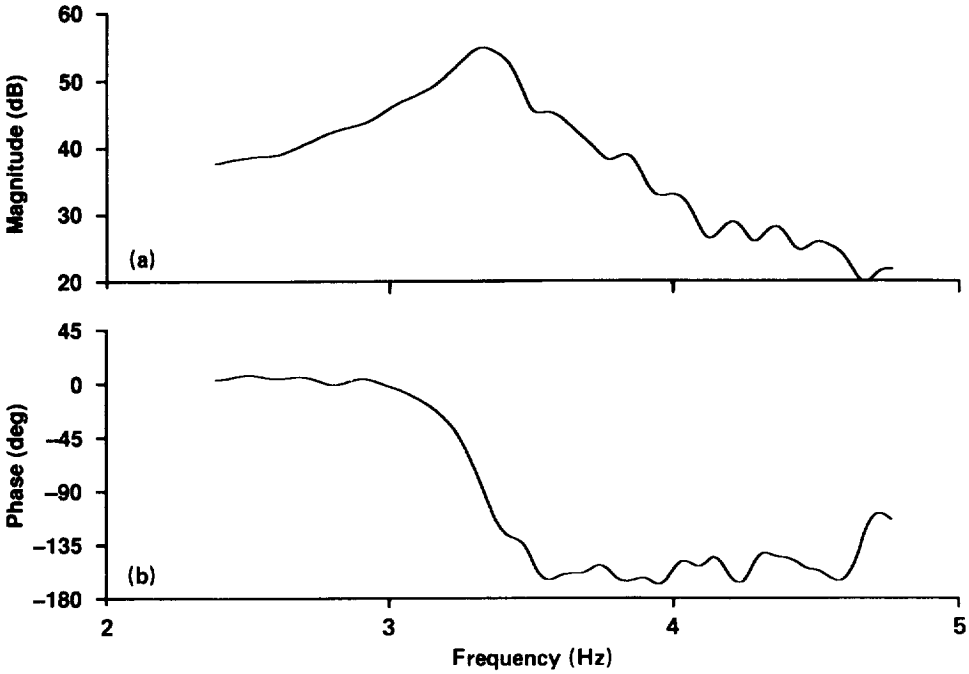

Figure 19. Frequency response H for the symmetric beam mode. (a) Magnitude, (b) phase.

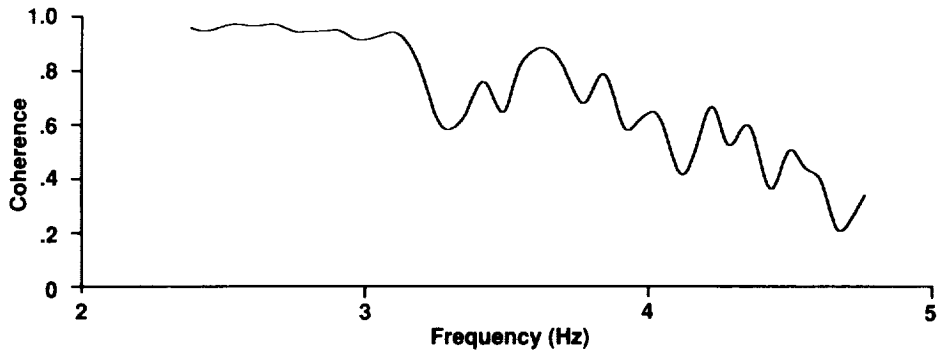

Figure 20. Coherence function γ^2_{xy} associated with the symmetric-beam-mode frequency response shown in figure 19.

symmetric torsion modes, falling off significantly at frequencies both above and below f_n. Furthermore, the coherence was sometimes reduced at the peak modal response itself, as is evident in figure 20. This effect was also seen during ground tests for which there were no aerodynamic loads, only low-level inertial responses.

The most likely cause of reduced coherence at the peak response is imperfect measurement of flaperon motion, including nonlinear linkage geometry, friction, and free play. Another possibility is that the wing structural response is inherently nonlinear and becomes more so when the response is of high magnitude, which is exactly the situation at the spectral peak. In addition, a nonlinear relation between flaperon motion and oscillatory airload would result in reduced coherence in the flight data. Nevertheless, the coherence was always high enough over some portion of the response to allow good mode identification.

Error analysis– There are many different ways of looking at errors in spectral analyses; see, for example, reference 18, which discusses at length the fundamental error limits of spectral functions generated by Fourier transforms. Bias and random errors are discussed below. The coherence function (eq. (12)) is a measure of linearity; its relation to random errors is also discussed. Repeatability of results between flight-test points is also important; statistics are given in the section Flight-Test Results.

If the input measurement noise $n_i(t)$ is zero, the calculated frequency response (eq. (3)) is unbiased. If $n_i(t)$ is nonzero, we have

$$|\hat{H}| = \frac{|H|}{1+\left[G_{n_i n_i}/G_{xx}\right]} \tag{13}$$

(The dependence of H and G on frequency f is implied.) The bias error is caused only by noise inputs that do not pass through the system.

For the frequency-sweep method, the bias error can be kept to very low levels. The input signal-to-noise ratio is about 40; the resulting bias error in $|H|$ is less than 2.5%. This is much less than the random error in estimating $|H|$, which is shown below to be 12%. (This value for the random error is misleadingly high; as will be shown, the consistency between independent estimates of modal parameters is much better.)

The normalized random error in the frequency-response magnitude is

$$\varepsilon\left[|\hat{H}|\right] \cong C_\varepsilon \frac{\left(1-\gamma^2_{xy}\right)^{1/2}}{|\gamma_{xy}|\sqrt{2\,n_d}} \tag{14}$$

where n_d is the number of statistically independent sections of data, and the factor C_ε accounts for the overlapping windows used by FRESPID. For a total length of concatenated time histories T_c, a section length of L points, and a sampling interval Δt,

$$n_d \cong \frac{T_c}{L\Delta t} \tag{15}$$

The non-normalized random error in the phase, $\varepsilon\left[\angle\hat{H}\right]$, is approximately the same magnitude (in radians) as $\varepsilon\left[|\hat{H}|\right]$ (ref. 18). Given a large enough value of the coherence, the frequency response has lower random errors than either the auto- or cross-spectrum, making it the preferred spectral function for mode identification.

For sections overlapped 50%, the total number of sections is $K = 2n_d - 1$. Reference 23 gives equations for the error reduction effected by overlapped windows. For an infinite number of squared-cosine (Hanning) windows with 50% overlap, $C_\varepsilon = 0.727$. A typical case for the study reported here was a 14-sec section applied to three 23-sec data runs, yielding $n_d = 5$ statistically independent sections and $K = 9$ sections total, for which $C_\varepsilon = 0.764$.

These values of C_ε are verified by the empirically derived factor of $\sqrt{0.55}$ given in reference 27.

Assuming $\gamma_{xy}^2 = 0.8$ at the spectral peak, $\varepsilon[|\hat{H}|] = 0.121$. However, the standard deviations of the modal parameters for a repeated flight condition are all less than the error derived from equation (14) (see Flight Test Results, table 2, for statistics for the baseline point). This is because the curve-fitting program NAVFIT effectively averages the spectra over 50 frequency points, reducing the averaged random error by a factor of $1/\sqrt{50}$ (neglecting variations in γ_{xy}^2). Thus, the limiting error is roughly 1.7%. This value does not include instrumentation or signal processing errors, or the effects of imperfectly flown test points.

Mode Identification Using NAVFIT

Many methods are available for identifying modal parameters from frequency spectra; reference 28 includes a discussion of some of the more common methods. With the exception of the integration method of reference 16, all methods employ a variation of curve fitting. Such methods are generally limited either in the number of data points that can be used or in the frequency range over which the points can be distributed. Some methods are also limited to second-order systems only, or can use only magnitude or phase data.

It is the combination of several features that makes the curve-fitting method embodied in NAVFIT unique:

1. Magnitude and phase data are fitted simultaneously.
2. There is no limit to the number of frequency points that can be fitted. (There is a program restriction of 50 points, but this is not a fundamental limit.)
3. There is essentially no limit to the frequency range that can be fitted: NAVFIT can handle dc up to the Nyquist limit, or whatever is specified for the chirp z-transform.
4. Multiple modes of arbitrary order can be explicitly modeled and fitted, as can be time delays. Furthermore, any parameter can be freed or fixed at any step in the fit.
5. The relative weights of magnitude and phase errors can be specified by the user.
6. The curve-fit error at each frequency point can be weighted by the coherence function.

The major drawback to NAVFIT is computational expense: the curve-fitting algorithm may take many iterations to converge. As more powerful computers are developed, however, computational time and expense will decrease. (Indeed, substantial increases in speed were seen during the course of the work reported here.) Another problem is that convergence to a local minimum is not precluded; user experience is needed to select appropriate initial estimates to avoid unrealistic fits. Also, NAVFIT is not highly automated; any highly generalized program requires extensive operator initialization for a particular problem. To alleviate this difficulty, a major upgrading of NAVFIT (and FRESPID) was completed in the new CIFER system (ref. 21) to simplify and partially automate the user inputs by incorporating more advanced user-interface concepts.

Curve-fit procedures– Once frequency responses have been calculated by the Fourier-transform program FRESPID, modal frequencies and damping are determined by fitting curves to the spectral data. Given a structure with natural frequency f_n and damping ratio ζ, the response can be well approximated by the quadratic second-order model of equation (4), repeated here:

$$H_M(f) = \frac{A}{1-(f/f_n)^2 + i2\zeta f/f_n} \tag{4}$$

Only such models (with a time delay included, if necessary) were used in the current study, as is appropriate for structural analysis.

Although the calculation of the frequency-response gain A by NAVFIT is necessary for an accurate curve fit, it is not used in subsequent aeroelastics analyses. The gain is determined largely by the sensitivities of the aircraft transducers and has no direct bearing on aeroelastic stability. See reference 29 for an illustration of the potentially misleading effects of gain variations.

The NAVFIT user specifies a frequency range, the order of the model to be fitted, and (optionally) initial estimates of f_n, ζ, and A. Phase shifts caused by unmodeled higher modes can be fitted with a time delay. An iterative algorithm is used to refine the model by systematically varying f_n, ζ, and A (and the time delay, when enabled) to get the best fit.

Fifty frequency points were used for each curve fit. The resolution of the fits depended on the frequency range used for each mode, but was always more coarse than the resolution of the spectral data generated by FRESPID. The spectral values actually used were those closest to an equal distribution in frequency over the specified, logarithmic fitting range, without any interpolation.

The model is fitted by minimizing a cost function Q, which is based on the squares of both magnitude and phase errors. To emphasize the most reliable data, the errors are also weighted by an exponential function of the coherence at each frequency point (ref. 30):

$$W(f) = 1.58\left(1 - e^{-\gamma_{xy}^2}\right) \tag{16}$$

The cost function is then

$$Q = \sum_{i=1}^{N} W(f_i)\left[H_M(f_i) - \hat{H}(f_i)\right]^2 \tag{17}$$

where i is the index of each of the N frequency points. The phase errors, in degrees, were weighted 7.57 times the magnitude errors, in decibels, thereby giving results equivalent to equal weighting of the real and imaginary parts of $|H|$ (ref. 8).

Earlier work (ref. 9) used a simple cosine weighting function to emphasize spectral data near f_n; coherence weighting was not used. For both weighting methods, standard deviations at the baseline point and standard errors over the airspeed range were calculated for f_n and ζ for all modes (see Flight-Test Results for definitions of the test conditions). Although there were no statistically significant differences (based on 10%-level F-ratio tests) between the results of the two weighting methods, coherence weighting proved to be more computationally robust and is a more general approach that may be applied to data with irregular variations in γ_{xy}^2. Consequently, the estimates of frequency and damping given in this report are generally different from those in reference 9 (see in particular tables 2 and 3 in Flight-Test Results).

Curve-fit examples– Examples of the use of NAVFIT to determine frequency and damping are given in figures 21–26 for the six modes. Note that magnitude and phase data are both fitted with second-order responses. Modal parameters determined by the fits are given in the figures. All spectra shown are based on the time-history data shown in figures 6–12 (but with three full sweeps). The frequency, magnitude, and phase scales have all been varied as required to best illustrate the details of each fit.

The symmetric beam mode is the most easily excited mode, and the second-order-response model yields a good fit (fig. 21). The fitted response is shifted slightly down in frequency at the peak spectral magnitude, but the shift is minimal for the fit to phase data. This illustrates the advantage of coherence weighting; the data at the peak are less reliable than on the flanks, as indicated by the drop in γ_{xy}^2 at 3.3 Hz in figure 20. The slight discrepancy in the curves at the peak magnitude is more than compensated for by a better fit to the rest of the response, especially for phase data.

The fit for the antisymmetric beam mode is shown in figure 22; the peak response is just below 6 Hz. Also visible is a second mode, apparently antisymmetric torsion, somewhat above 7 Hz, which could have two possible origins. Either the strain gages were not perfectly installed, so that they responded slightly to off-axis structural loads; or an aeroelastic mode in one axis caused changes in the total airloads that were then reflected by additional loads in other axes, so that even perfect strain gages responded to more than one mode. The curve fit was modified by truncating the frequency range at 40 rad/sec (6.4 Hz) to avoid the higher frequency mode; note that the phase dictates the upper limit of the fit. In principle, a multi-mode model could have been fitted by extending equation (4) to include two quadratic systems, but truncating the second-order model proved adequate (and was much more efficient).

The model for the symmetric chord mode (fig. 23) was similarly truncated to avoid the symmetric torsion mode (not visible in the figure); otherwise, the fit was straightforward. The frequency range of the curve fit for each mode was determined by the worst noise or spectral interference (such as the 1/rev spike) in all of the spectra generated for that mode. Thus, the fit to magnitude data in figure 23 could have been safely extended to perhaps 7 Hz, but not the fit to phase data.

The antisymmetric chord mode (fig. 24) offers perhaps the best example of a difficult fit; the magnitude data are noisy, and the phase data show the strong influence of neighboring modes, visible as a nearly constant time delay. NAVFIT can fit a pure time delay in addition to the second-order model of equation (4) to account for the influence of higher order modes; this option was exercised for all modes and resulted in an acceptable fit to the antisymmetric-chord phase response.

Figure 25, the fit for the symmetric torsion mode, illustrates yet another problem: the 1/rev spike at 8.6 Hz. It is broadened in part by the averaging of a long time history over which the rotor speed was not perfectly constant, and in part by the highly expanded frequency scale. In the example given, coherence weighting could have been used to effectively ignore the data at the spike, allowing a good fit both above and below it. However, there were other flight conditions for which the spectra were too noisy to permit consistent phase calculations across the spike. Therefore, all fits for the symmetric torsion mode were truncated at 53 rad/sec (8.4 Hz). Truncation at the low-frequency end of the fit was also necessary to avoid severe spectral noise outside the range of the response.

The final example, the antisymmetric torsion mode, is shown in figure 26. The curve fit was truncated here also, again because of a 1/rev problem. In this case, the 1/rev effect is not confined to a simple spike, but is manifest as corrupted spectra well above and below the rotor frequency. Because a 1/rev disturbance is neither symmetric

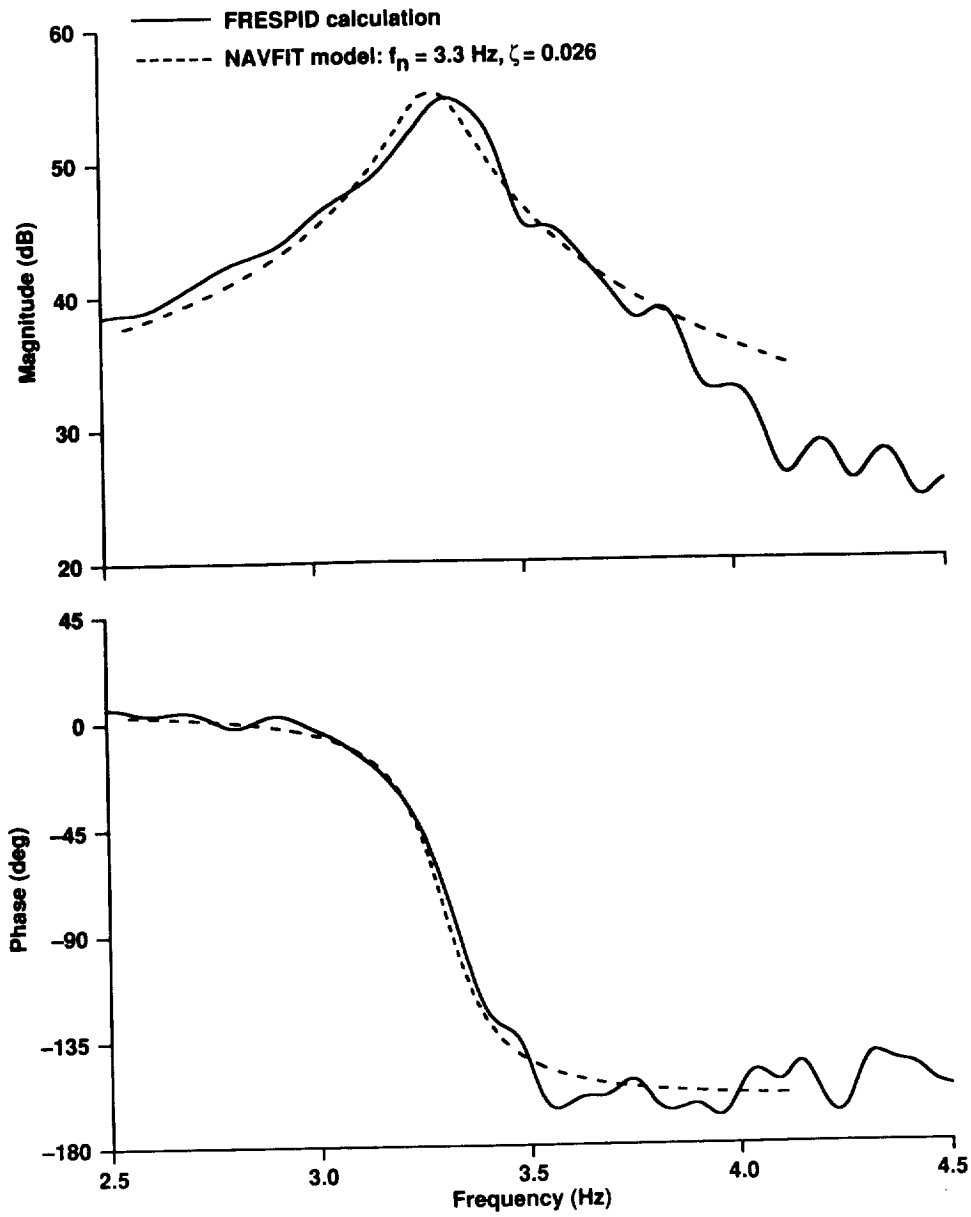

Figure 21. Curve fits to the symmetric-beam-mode frequency response.

nor antisymmetric (unless by accident), its effects cannot be reliably canceled by sum-and-difference procedures. The magnitude and phase of the net 1/rev response depend on the track and balance of the two rotors; they are not necessarily constant from one flight to the next, or even for all flight conditions in a given flight.

Curve-fit parameters– Table 1 lists the frequency ranges and initial mode estimates used for all modes. The frequency ranges were compromises between including the most data possible and concentrating the curve fits near the modal peaks. The preferred range was $0.8\omega_n$ to $1.2\omega_n$ (estimated), but the range was often truncated to avoid neighboring modes or noise, such as the 1/rev spike near the symmetric torsion mode. The initial estimates were chosen for convenience; they ensured that each series of curve-fit iterations began from a consistent set of initial conditions.

FLIGHT-TEST RESULTS

Frequency sweeps were performed for a variety of flight conditions, mostly level flight at 10,000 ft. The results of frequency-domain analysis of the flight-test data are presented below, along with older, exponential-decay

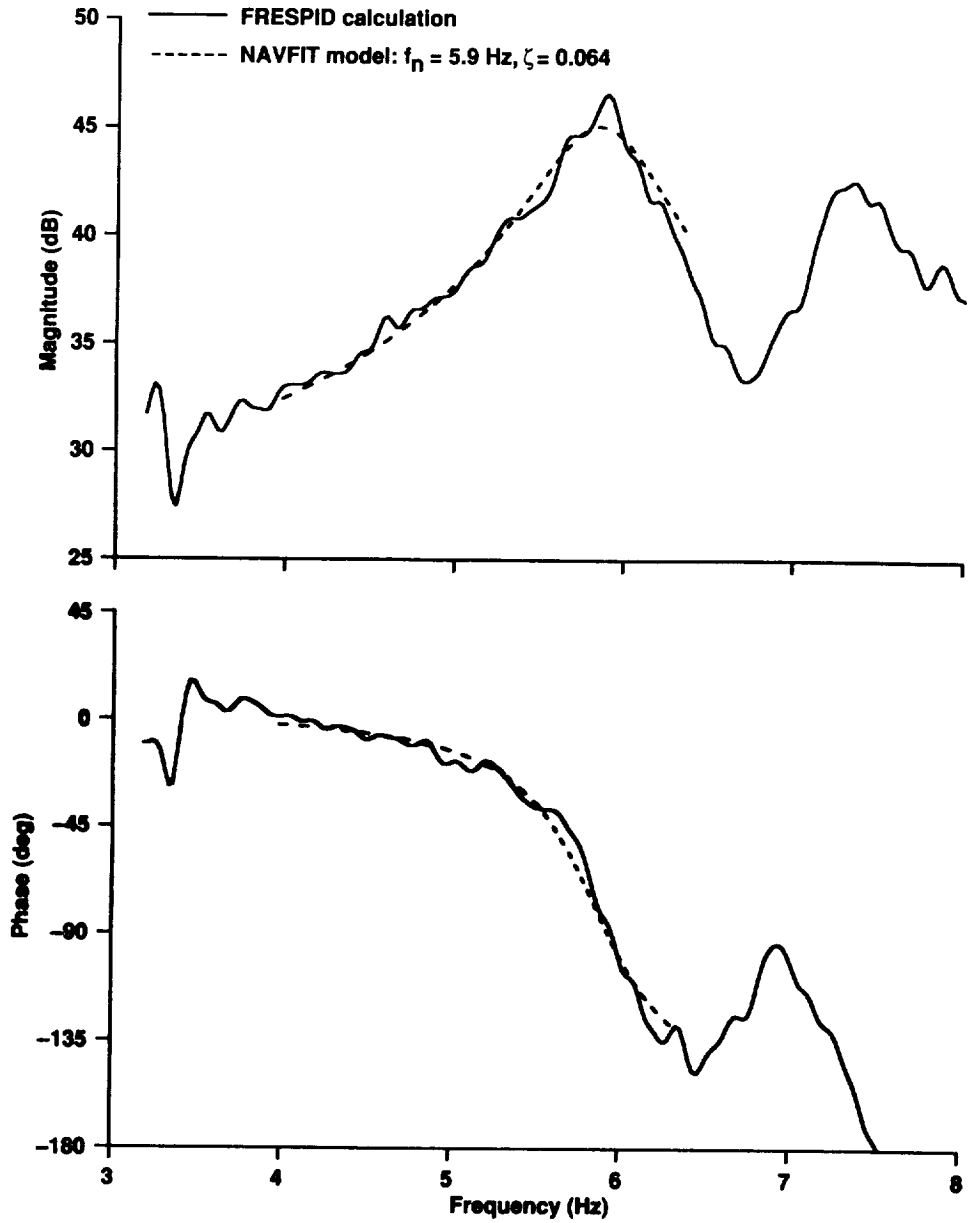

Figure 22. Curve fits to the antisymmetric-beam-mode frequency response.

Table 1. NAVFIT initial conditions

Mode	Frequency range, min–max (rad/sec)	A	ζ	ω_n (rad/sec)
Symmetric beam	16–26	30	0.02	21
Antisymmetric beam	25–40	–20	0.06	37
Symmetric chord	30–42	50	0.04	40
Antisymmetric chord	40–50	40	0.04	46
Symmetric torsion	42–53	20	0.04	51
Antisymmetric torsion	35–47	20	0.06	45

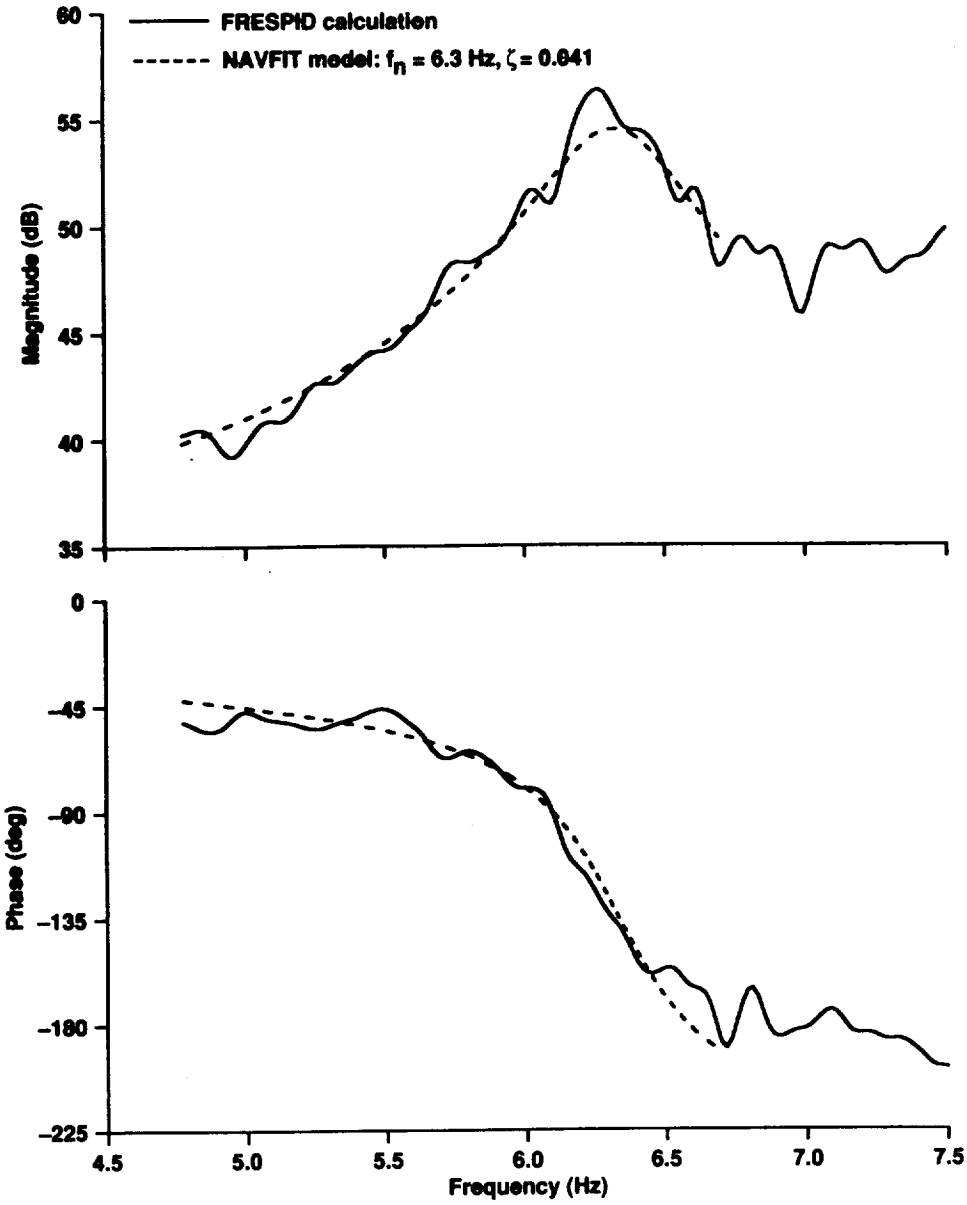

Figure 23. Curve fits to the symmetric-chord-mode frequency response.

results from reference 31. Predictions made with two different analysis programs, ASAP and CAMRAD, are presented for comparison. The following sections describe the test data obtained, compare the results of the frequency-sweep and exponential-decay methods, and compare the frequency-sweep results with the predictions.

Test Conditions

Figure 27 shows the portions of the XV-15 flight envelope covered during the latest aeroelastics flight tests. Because the aircraft had already been cleared (with the exponential-decay method) to fly the envelope shown, the frequency sweeps were concentrated within a fairly narrow region so as to more rigorously verify the frequency-domain technique. The most complete data set obtained is discussed at length in the remainder of this report; it was acquired at a density altitude of 10,000 ft at 86% rotor speed (8.6 Hz), with a typical gross weight near 13,000 lb. The airspeed range was 180 KTAS (150 KIAS) (the normal speed for conversion to airplane mode) to 260 KTAS (220 KIAS) (the torque-limited maximum speed for level flight). See appendix A for a detailed tabulation of all test conditions.

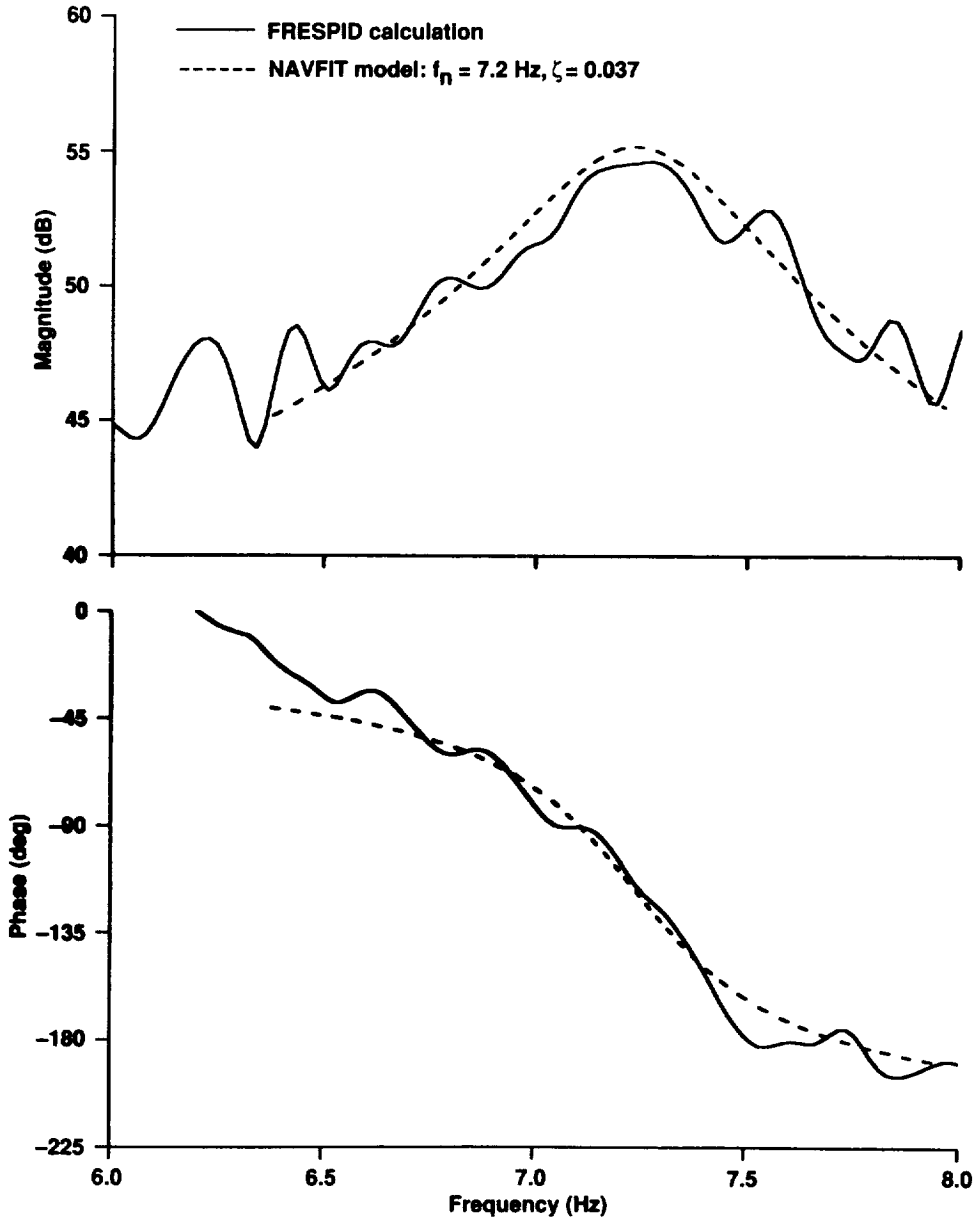

Figure 24. Curve fits to the antisymmetric-chord-mode frequency response.

Limited frequency-sweep data were also taken at 5,000 ft and 15,000 ft at 86% rotor speed, and at 10,000 ft at 98% rotor speed. Maximum-power climbs and power-off descents were performed at 150 KIAS at 86% rotor speed, with data taken as the aircraft passed 10,000 ft. The results of analyzing these additional data sets are summarized in the section Additional Flight Data.

Ideally, several replications (i.e., several complete, independent sets of three symmetric and three antisymmetric sweeps) would have been performed at each flight condition. Because this would have taken far too much flight time, an easily repeatable flight condition was chosen as a baseline for replications: 180 KTAS at 10,000 ft density altitude and 86% rotor speed. The XV-15 usually achieves this condition immediately after conversion to cruise mode, making it an efficient baseline point. Five full replications were performed to explicitly test for scatter in the frequency and damping estimates.

Earlier flight tests (ref. 11) revealed interaction of the Stability Control Augmentation System (SCAS) with modal responses; this was eliminated by modification of the SCAS. To ensure that there were no other interactions, each part of the automatic flight control system—the SCAS, the Attitude Retention System (ARS), and the

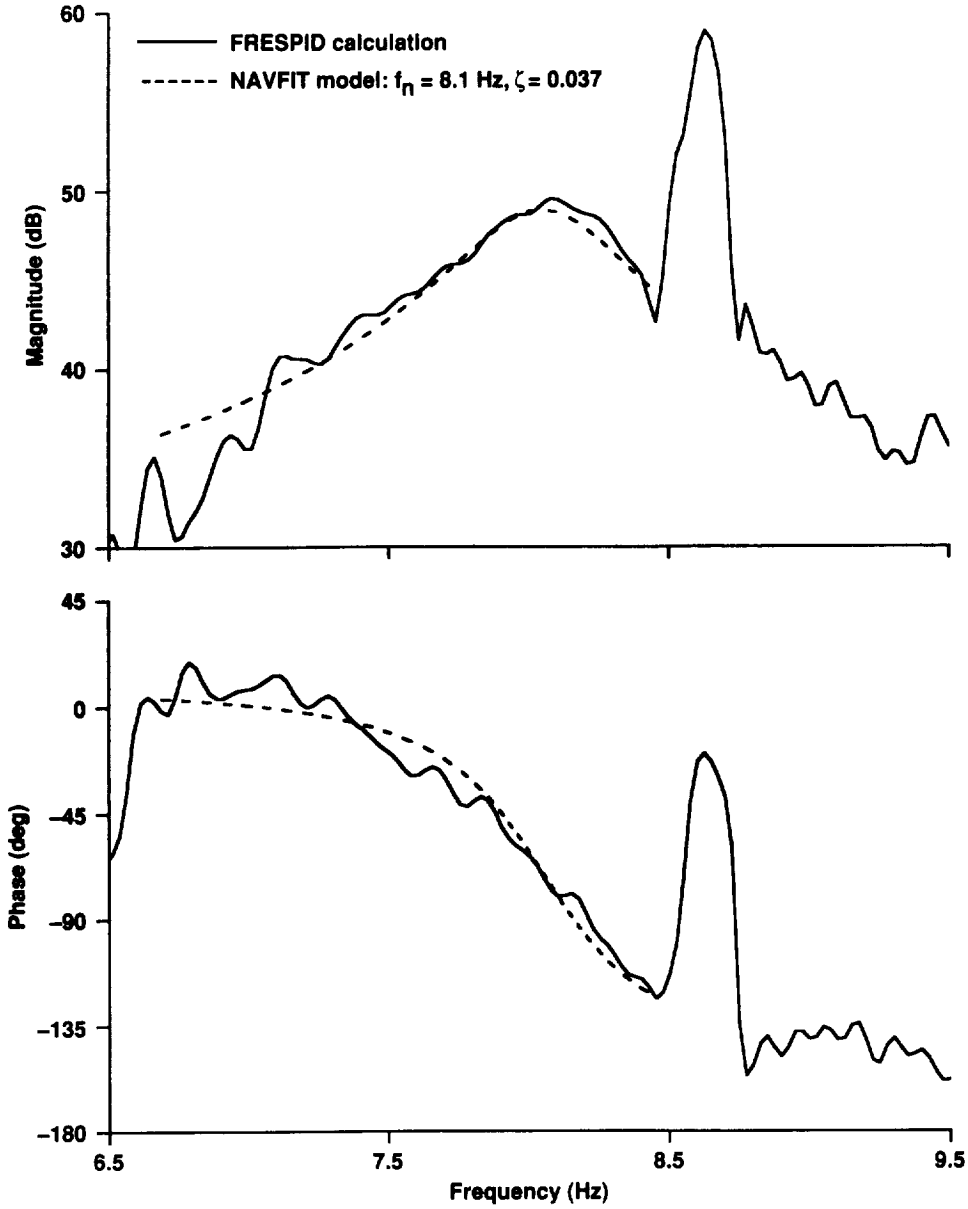

Figure 25. Curve fits to the symmetric-torsion-mode frequency response.

Force Feel System (FFS)—was individually turned off during three series of sweeps at the baseline point. In a comparison of the results with the other baseline estimates, no statistically significant differences were noted. (This analysis was based on the "Gross Errors" test of reference 32.) These data were subsequently included in the baseline data.

A less rigorous, but still useful, test of scatter was provided by the speed-sweep data, one full set at a density altitude of 10,000 ft and one partial set at 15,000 ft, both sets at 86% rotor speed. Only the first set was analyzed for scatter, because it contained the most data points.

Figures 28(a) through 28(f) summarize the frequency and damping results for all six aeroelastic modes for the 10,000-ft speed-sweep data (level flight at 86% rotor speed). Closed symbols are estimates made using frequency-sweep data; open symbols are exponential-decay estimates (from reference 31, which does not give an explicit frequency estimate corresponding to each damping estimate). All data are plotted against true airspeed, the critical value for aeroelastics. The frequency-sweep method yields low scatter at the baseline point and good consistency between airspeeds, which is a considerable improvement over the exponential-decay method.

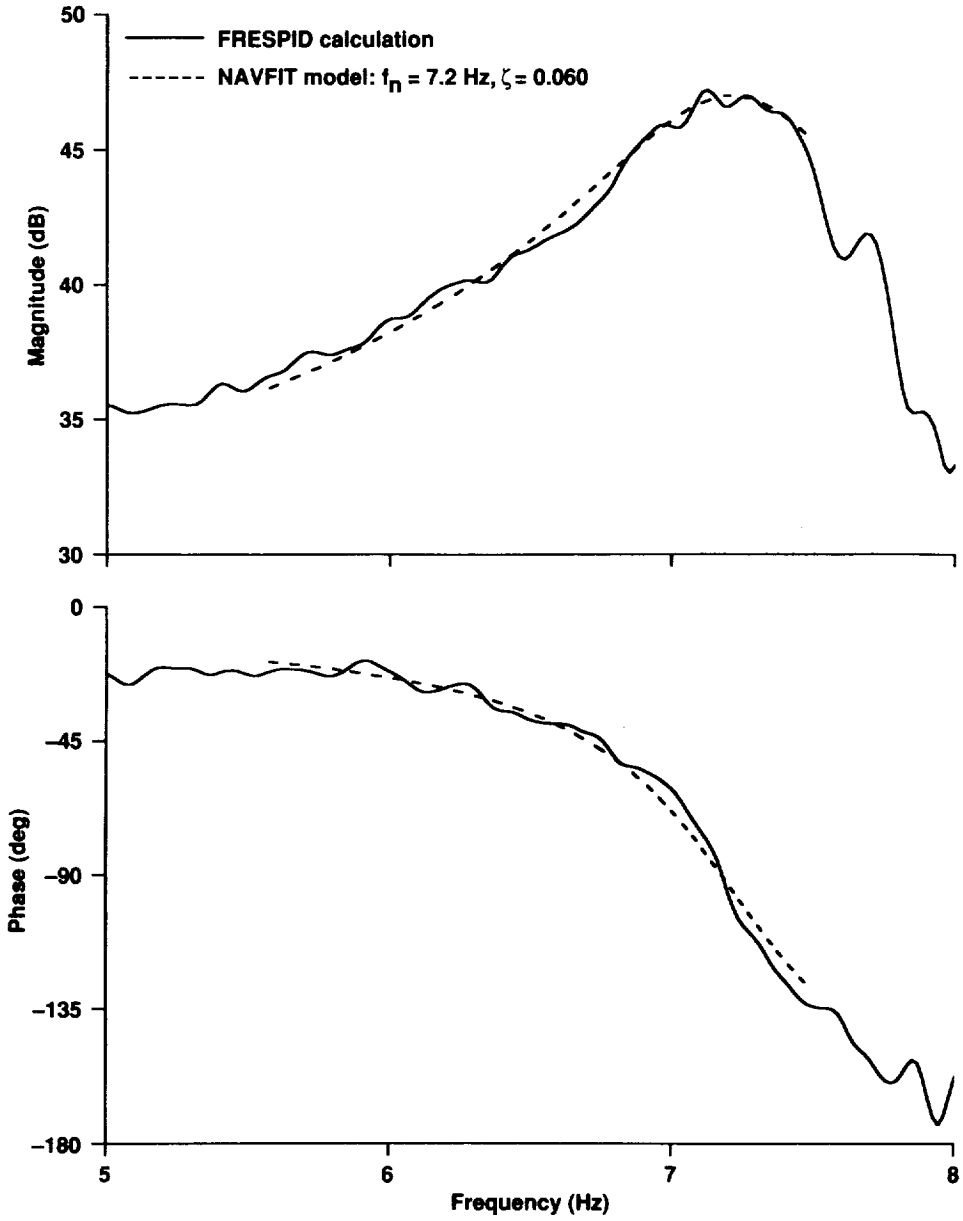

Figure 26. Curve fits to the antisymmetric-torsion-mode frequency response.

(Individual modes are discussed in detail in the section Individual Modes.)

Numerical results of the frequency-sweep method are summarized in table 2 for the 180-knot baseline point. Listed for each mode are the averages of damping ratio $(\overline{\zeta})$ and natural frequency $(\overline{f_n})$ and their respective standard deviations (σ_ζ and σ_{f_n}). The standard deviations of the damping ratio are from 7% to 9% of the average values, and the standard deviations of the frequency are all less than 1%.

In a few frequency-sweep cases—notably, antisymmetric torsion—a statistically significant fraction of the scatter (based on a 10%-level *t*-test) can be explained by weight changes caused by fuel burnoff. All baseline points were curve-fitted against gross weight to determine the correlation coefficients, which indicate the amount of variation caused by changes in weight. For the significant cases, the percentage of total variation caused by weight changes is 59% for symmetric-beam f_n; 49% for symmetric-chord ζ; and 82% and 40% for antisymmetric-torsion f_n and ζ, respectively. (These may not be the only effects of weight; see the discussion of altitude variations in the section Additional Flight Data.) It is not practical to collect all flight data at exactly the same fuel state.

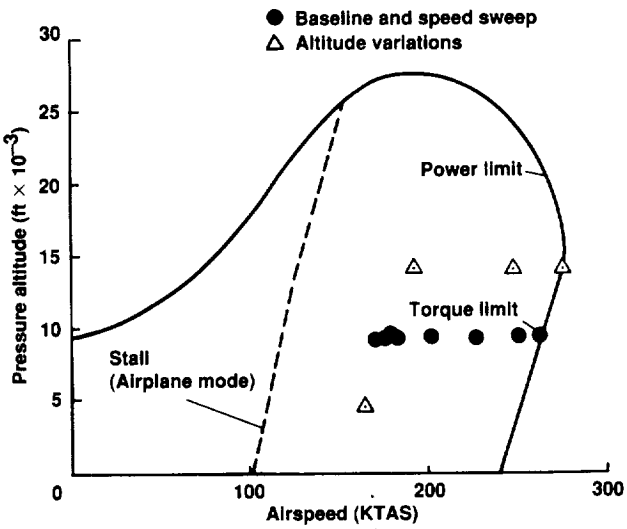

Figure 27. XV-15 flight envelope, with frequency-sweep test points.

Therefore, the values given in table 2 represent a realistic performance of the frequency-sweep flight-test method.

Exponential-Decay and Frequency-Sweep Data

Most previous XV-15 aeroelastics data were acquired with the exponential-decay method (refs. 11 and 12). An exciter—on either the flaperon or collective controls—was tuned to the frequency of maximum response for each mode, then abruptly shut off. Time histories of the resulting exponential decay of the mode were then fitted with damped sinusoidal functions (Prony method) to obtain estimates of modal frequencies and damping. The exponential-decay results plotted in figure 28 were taken from reference 31.

A comparison of the old exponential-decay results with the new frequency-sweep results presents some problems. The aircraft configurations used to gather the two types of data did not match exactly. There are two different XV-15 aircraft, one operated by Bell Helicopter Textron (serial number 702) and one by NASA Ames Research Center (serial number 703). Three different versions of rotor hubs have been flown: titanium hubs with either 2.5° or 1.5° precone, and steel hubs with 1.5° precone. The exponential-decay results shown in figure 28 are for aircraft 703 with 2.5° titanium hubs and a single flaperon exciter; the frequency-sweep results are for aircraft 703 with 1.5° steel hubs and dual flaperon exciters. Both configurations had 50,000-lb/in downstops. The data shown in figure 28 are the most closely matched aeroelastics data sets available for identical flight conditions.

Limited exponential-decay data exist for 1.5° steel hubs, but there are not enough data points to provide meaningful statistical comparisons. Inspection of the exponential-decay data available for aircraft 702 (ref. 31) reveals no obvious reduction in scatter for the dual-flaperon configuration.

Similar cautions apply to all other available aeroelastics data, such as that in references 11 and 12. Much of the published data are for aircraft 702, which was usually equipped with a flapping controller that trimmed lateral cyclic in cruise; this was to minimize 2/rev vibrations caused by the Hook's joints in the gimballed hubs. Moreover, some of the published data are misleading; in reference 31, figures 12.3-1 through 12.3-6 are labeled "level flight," but the data at 10,000 ft above 230 KCAS were taken during powered descents (L. G. Schroers, private conversation; see also the level flight envelope, reference 31, figure 2.4-3).

Table 2. Statistics for NAVFIT estimates of XV-15 wing modes at the baseline flight condition*

Mode	$\bar{\zeta}$	σ_ζ	σ_ζ % relative error	$\bar{f_n}$ (Hz)	σ_{f_n} (Hz)	σ_{f_n} % relative error
Symmetric beam	0.0254	0.00235	9.3	3.30	0.0083	0.25
Antisymmetric beam	0.0609	0.00398	6.5	5.90	0.0424	0.72
Symmetric chord	0.0394	0.00326	8.3	6.33	0.0110	0.17
Antisymmetric chord	0.0389	0.00349	9.0	7.25	0.0278	0.38
Symmetric torsion	0.0397	0.00362	9.1	8.08	0.0203	0.25
Antisymmetric torsion	0.0607	0.00406	6.7	7.25	0.0396	0.55

*Based on eight data points.

In order to make statistical comparisons between the results of the two flight-test methods and their corresponding analyses, both sets of frequency and damping estimates (for the 10,000-ft level-flight data in fig. 28) were curve-fitted against airspeed. This procedure allowed consistent comparisons to be made using all of the data. Linear fits were used, partly because all predictions showed a nearly constant slope within the airspeed range, and partly because the standard errors of each fit would be a conservative measure of scatter if the true variations were in fact nonlinear. The standard errors, slopes, and intercepts of the frequency and damping curve fits are listed in table 3 for each mode. A comparison of the curve fits shows that, except for symmetric-torsion-mode damping, the frequency-sweep estimates had significantly less scatter (based on a 2.5%-level F-ratio test) in both frequency and damping than the exponential-decay estimates. Even for symmetric-torsion-mode damping, the frequency-sweep method showed less scatter, but the improvement was not statistically significant.

In light of the caveats mentioned above, the statistical comparisons between the frequency-sweep and exponential-decay results cannot be considered completely rigorous. Further considerations are the limited number of frequency sweeps above the baseline airspeed, and severe roundoff errors in the available exponential-decay results. Repeating the flight tests with completely identical aircraft, over a wider airspeed range, and with several full replications of each test condition for both methods would doubtless yield considerably different statistics. Nevertheless, it is notable that the frequency-sweep method yielded lower scatter than the exponential-decay method in every case, without exception, and that the scatter in the estimates of modal frequencies was generally an order of magnitude lower for the frequency-sweep method.

Predictions and Flight-Test Results

A detailed assessment of all available predictive methods is beyond the scope of this paper. (A comprehensive review of the history and current state of the art of aeroelastic predictive methodologies is given in ref. 4). Two different programs—ASAP and CAMRAD—were used to avoid biasing the comparisons with flight data toward one type of theoretical analysis. The ASAP and CAMRAD predictions are plotted with the flight-data estimates in figure 28. The predictions are, in theory, continuous curves and are plotted as dashed or solid lines to distinguish them from the discrete flight-data estimates. (Predictions are, in fact, calculated for several discrete airspeeds and then plotted by connecting those points.) Because of the superior statistical results of the frequency-sweep method, only those flight data are compared with the predictions.

The ASAP predictions of frequency and damping were made by Bell Helicopter Textron; the CAMRAD predictions were made by NASA. ASAP is an analysis program proprietary to Bell; it is similar in concept to PASTA (ref. 33), but completely rederived and reprogrammed. ASAP was originally developed for the V-22 program and was modified by Bell for the XV-15 predictions given here. The CAMRAD model used here is based on that of reference 5, but is updated to have the correct precone for the steel hubs and to use recalculated NASTRAN mode shapes. (The recalculation is necessitated by the heavier hubs.) The ASAP and CAMRAD predictions were all based on nominal flight-test conditions of 10,000 ft altitude, 86% rotor speed, and 13,000 lb gross weight. (Reference 9 used predictions from DYN4, a less sophisticated program replaced by ASAP, and from an older CAMRAD model that incorporated a less accurate representation of the XV-15.)

The differences between the ASAP and CAMRAD predictions extend beyond their computational methods. The programs used different aerodynamic and structural models of the rotor blades. Both programs rely on external sources of structural modes data for the airframe, but ASAP had a more comprehensive model (i.e., more airframe modes) than CAMRAD, with small variations in the commonly modeled modes. Also, the programs used different structural damping values. All predictions given here use natural frequencies, mode shapes, and generalized masses generated by NASTRAN.

NASTRAN does not calculate structural damping—those values must be deduced from test data or assumed from experience. For the six wing modes, the ASAP predictions used zero-airspeed structural damping values derived from a 1/5-scale, rotors-off wind tunnel test (1988 entry) of an aeroelastic model of the V-22, and the CAMRAD zero-airspeed values were derived by empirically adjusting CAMRAD damping estimates to match earlier flight data. The first set of values (ζ_{sm}) was provided by Bell; the second set (ζ_{se}) is the same as the "post-test" values in reference 14 (also used in refs. 5 and 9). If desired, CAMRAD can calculate aerodynamic damping separately from structural damping, but ASAP always lumps the two together. For the empirical case (labeled ζ_{se} in the figures), CAMRAD calculated aerodynamic damping separately from structural damping; otherwise, both ASAP and CAMRAD lumped aerodynamic and structural damping together as ζ_{sm}. All other airframe modes were assumed to have a damping ratio of 0.01.

No frequency or damping data that have been directly verified by a structural test exist for the XV-15. The values of zero-airspeed structural frequencies and damping

Table 3. Statistics for frequency and damping curve-fits against airspeed

Mode	Frequency-domain estimates				Exponential-decay estimates (ref. 30)				Analytical predictions	
	No. of points	Standard error of f_n (Hz)	Intercept of f_n (Hz)	Slope of f_n (Hz/knot $\times 10^{-3}$)	No. of points	Standard error of f_n (Hz)	Intercept of f_n (Hz)	Slope of f_n (Hz/knot $\times 10^{-3}$)	CAMRAD Slope of f_n (Hz/knot $\times 10^{-3}$)	ASAP Slope of f_n (Hz/knot $\times 10^{-3}$)
Symmetric beam	12	0.00965	3.35	–0.265	3	0.0378	2.73	2.49	–0.208	–0.294
Antisymmetric beam	12	0.0350	5.67	1.27	4	0.252	6.32	0.00	–1.18*	–0.560*
Symmetric chord	12	0.0159	6.54	–1.18	4	0.212	6.44	0.059	–1.30	–1.78*
Antisymmetric chord	12	0.0296	7.08	0.893	4	0.289	5.76	10.0	–1.71*	–2.19*
Symmetric torsion	12	0.0324	8.20	–0.684	6	0.298	9.05	–4.84	–2.37*	–2.78*
Antisymmetric torsion	12	0.0397	7.96	–3.98	6	0.248	8.61	–6.05	–0.860*	–1.30*
	No. of points	Standard error of ζ	Intercept of ζ	Slope of ζ per knot $\times 10^{-5}$	No. of points	Standard error of ζ	Intercept of ζ	Slope of ζ per knot $\times 10^{-5}$	Slope of ζ per knot $\times 10^{-5}$	Slope of ζ per knot $\times 10^{-5}$
Symmetric beam	12	0.00197	0.0113	7.86	6	0.00422	0.00865	6.86	2.88*	5.14
Antisymmetric beam	12	0.00358	0.0659	–2.98	9	0.0102	0.0882	–14.8	5.68*	5.84*
Symmetric chord	12	0.00307	0.0214	10.2	12	0.0164	–0.0461	50.0	1.08*	3.66
Antisymmetric chord	12	0.00373	0.0453	–3.85	9	0.0164	0.00883	21.8	3.72	8.02*
Symmetric torsion	12	0.00376	–0.0141	30.1	8	0.00491	–0.0536	55.5	7.72*	10.07*
Antisymmetric torsion	12	0.00395	0.00615	30.8	10	0.0101	–0.0575	49.2	1.80*	3.30*

*Statistically significant difference between estimated (frequency domain) and predicted slopes.

used for all predictions reported herein are given in table 4. To keep the statistical comparisons in table 3 consistent with the values in table 4, predictions made with the older damping values ζ_{se} are not included in table 3 or in the discussions of individual modes later in this section.

Two notes should be made about the zero-airspeed values. First, it should be emphasized that the more recent values of structural damping (ζ_{sm}) are not necessarily more accurate than the older values (ζ_{se}). CAMRAD predictions made with the assumptions of reference 14 were always closer to the frequency-sweep estimates than were the predictions made with the newer damping values. This result is hardly surprising, because in reference 14, structural damping inputs were empirically adjusted to force the final aeroelastic predictions to fit XV-15 flight data (which was acquired, in that case, by using exponential decays; see refs. 11 and 12). The different damping assumptions have negligible effects on the CAMRAD predictions of frequencies; the differences are not visible at the scale of figure 28.

Second, it unfortunately is not valid to extrapolate the fitted curves of flight-test data down to 0 KTAS to obtain estimates of zero-airspeed structural frequencies and damping; the predicted curves (fig. 5) are nonlinear, and there are increasingly large statistical uncertainties as the fitted curves are extended beyond the range of the flight

Table 4. Zero-airspeed frequency and damping values used for predictions

	ASAP		CAMRAD		
Wing modes	f_s (Hz)	ζ_{sm}	f_s (Hz)	ζ_{se}	ζ_{sm}
Symmetric beam	3.25	0.015	3.23	0.015	0.015
Antisymmetric beam	6.47	0.020	6.42	0.025	0.020
Symmetric chord	6.27	0.019	6.20	0.035	0.019
Antisymmetric chord	7.69	0.050	7.63	0.025	0.050
Symmetric torsion	8.48	0.0175	8.32	0.040	0.0175
Antisymmetric torsion	8.29	0.017	8.19	0.030	0.017
Other airframe modes*					
Symmetric horizontal tail beam	13.10	0.010			
Antisymmetric horizontal tail beam	9.75	0.010			
Antisymmetric fuselage lateral bending	10.08	0.010			
Symmetric engine yaw	14.61	0.010	14.53	0.010	
Antisymmetric engine yaw	13.34	0.010			
Symmetric pylon yaw	15.07	0.010			
Antisymmetric pylon yaw	18.45	0.010	18.41	0.010	
Symmetric vertical tail beam	20.37	0.010			
Antisymmetric engine pitch	20.03	0.010			
Symmetric horizontal tail torsion	25.73	0.010			
Antisymmetric horizontal tail torsion	22.79	0.010			

*Assumed damping values.

data. Any correspondence between the intercepts listed in table 3 and the zero-airspeed values in table 4 is largely fortuitous.

The failure of the frequency predictions to match the flight data, especially for antisymmetric chord, is thought to be due to imperfect NASTRAN modeling, which would affect both CAMRAD and ASAP predictions. Reference 11 mentions a change to the NASTRAN model in an attempt to improve its prediction of antisymmetric chord frequency; the change proved helpful, but a large error remains.

The current study was not designed to permit rigorous comparisons between ASAP and CAMRAD. However, the following observations can be made. ASAP and CAMRAD gave very similar predictions, usually matched more closely to each other than to the NAVFIT estimates. The differences between the ASAP and CAMRAD predictions based on the same assumptions of zero-airspeed structural damping (ζ_{sm}) were generally much less than the differences between the CAMRAD predictions made with different input values of structural damping (ζ_{sm} versus ζ_{se}). These results imply that errors in the NASTRAN models of the XV-15 and uncertainties in the estimation of structural damping are at least as important as the differences between the analytical methods of ASAP and CAMRAD.

A comprehensive comparison of ASAP and CAMRAD would require a thorough reconciliation of the blade and airframe structural models. However, this was not considered necessary for the current work, especially in light of the dominant effects of damping assumptions. Increased attention should be given instead to improving and verifying the NASTRAN model of the XV-15 and acquiring trustworthy values of zero-airspeed structural damping.

The slopes of the NAVFIT estimates (derived from flight data) that show statistically significant differences from either the CAMRAD or ASAP predictions (based on a 5%-level t-test) are noted in table 3. For XV-15 envelope expansion, changes in damping with airspeed are more important than absolute magnitudes, hence the emphasis on the slopes. The slopes of the predictions are derived from several discrete values of f_n and ζ, but it can safely be assumed that the standard errors of these slopes are negligible in comparison with those derived from flight-test data. The large number of significant variations from the predictions actually speaks well of the frequency-domain technique: had the scatter in any given set of NAVFIT estimates been very large, a t-test would not have shown a significant difference, even if the true slopes were unequal.

The statistical comparisons between the predictions and the flight data are potentially misleading because there are uncertainties, caused by numerical round-off errors and by the small number of flight-test data points, in the curve fits to the predictions. Furthermore, it is unlikely that the scatter in the flight-data estimates would be as low as that given in table 3 if fully replicated data were available. Nevertheless, figure 28 and tables 2 and 3 together show that the frequency-domain method is sufficiently sensitive and repeatable to reliably detect seriously erroneous predictions of aeroelastic stability, and hence provides confidence in a safe envelope expansion. It is not valid to go beyond that and attempt to judge which predictive program is superior, especially in light of the unverified NASTRAN and structural-damping data.

Individual Modes

The major results for the six wing modes are combined in figures 28(a) through 28(f), one figure for each mode. The scales for damping ratio are the same in all figures, and the frequency scales all have the same increments. However, the absolute ranges of the frequency scales were allowed to vary to better reveal small differences in the results.

Evaluation of scatter by inspection of the figures can be misleading, especially when only a few data points are available. Accordingly, the reader is referred back to tables 2 and 3 for comparisons of the frequency-sweep and exponential-decay results. Only the former are discussed below.

Symmetric beam (fig. 28(a))– The CAMRAD and ASAP predictions of natural frequency f_n are about 0.1 Hz lower than the NAVFIT frequency-domain estimates derived from the flight data, and they slowly decrease with increasing airspeed, as do the estimates. The predicted values of damping ratio ζ are slightly lower in magnitude and increase more slowly with airspeed than the flight-data estimates. The dip in the ASAP predictions of ζ at 175 knots also occurs in the CAMRAD predictions, but at a lower airspeed (visible for the sea level predictions in fig. 5). The drop in predicted damping is caused by coupling between the symmetric beam mode and the regressing in-plane rotor mode (this was pointed out to the authors by D. Popelka); the effect is somewhat exaggerated by ASAP. The 175-knot point was not included in the ASAP curve fit (table 3).

Antisymmetric beam (fig. 28(b))– The predictions of f_n are about 0.5 Hz higher than the estimates and decrease with increasing airspeed, unlike the slowly increasing estimates. The predictions of ζ average at least 0.02 (2% critical damping) below the estimates and increase with airspeed; the estimates are nearly constant (their slope is not significantly different from zero).

Symmetric chord (fig. 28(c))– The predictions of f_n are about 0.2 Hz below the estimates and decrease with

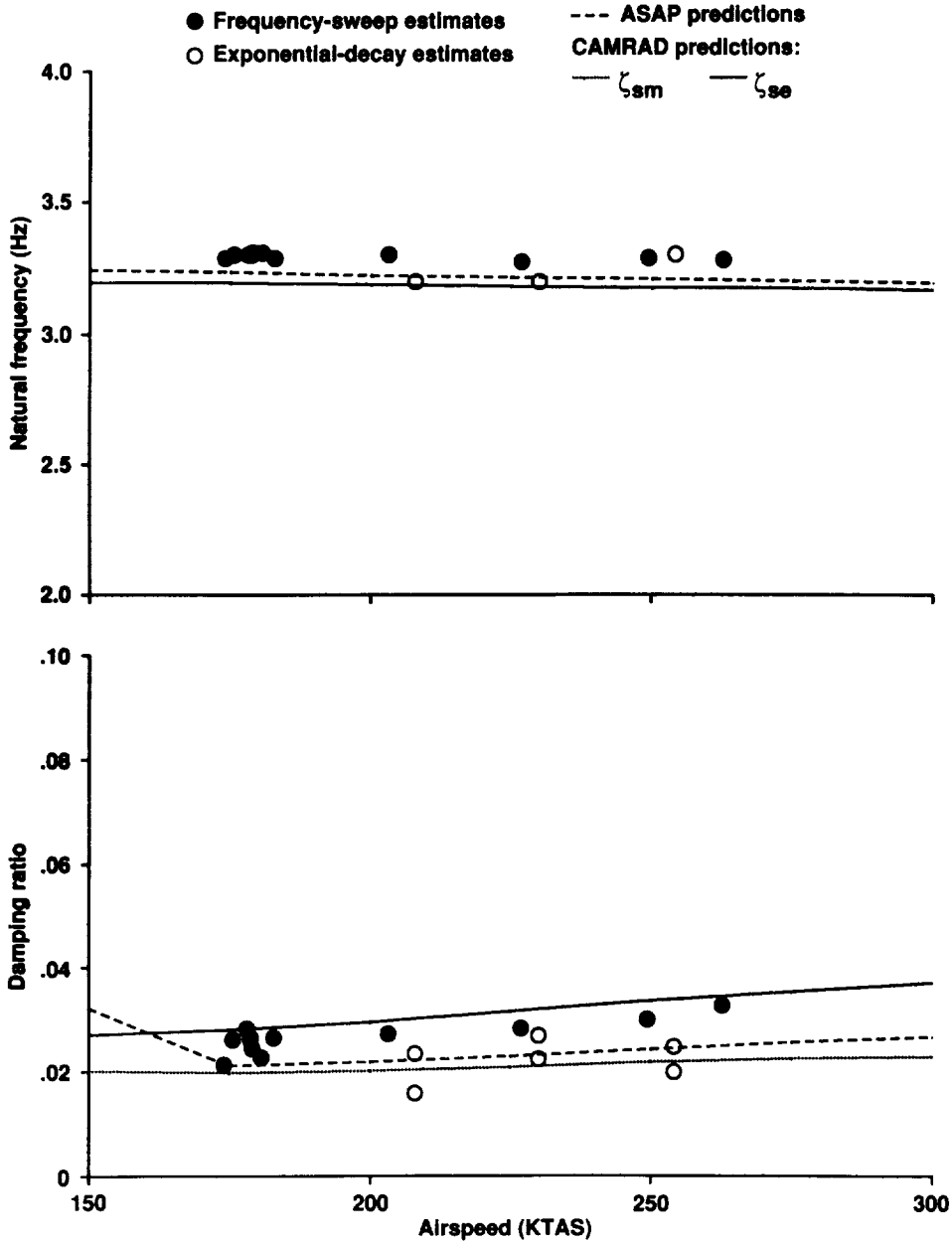

Figure 28. Flight-data estimates and analytical predictions of (top) f_n and (bottom) ζ. (a) Symmetric beam mode.

increasing airspeed at roughly the same rate. The predictions of ζ are as much as 0.02 lower than estimated and increase less rapidly with airspeed, especially for CAMRAD.

Antisymmetric chord (fig. 28(d))– The predictions of f_n are slightly greater than estimated and do not follow the slope of the estimates. The predictions of ζ are up to 0.02 greater than estimated, with positive slopes (especially ASAP). The dip in the estimated damping at 275 knots is thought to be caused by scatter.

Symmetric torsion (fig. 28(e))– The predictions of f_n lie within 0.1 Hz of the estimates. It cannot be determined whether the change in the slope of the estimates above 225 knots is an accurate reflection of XV-15 aeroelastic behavior or is an illusion caused by scatter. The predictions of ζ are more than 0.01 lower than estimated and show a significantly slower rise with airspeed.

Antisymmetric torsion (fig. 28(f))– The predictions of f_n are generally over 1 Hz greater than the estimates and decrease more slowly with increasing airspeed. The

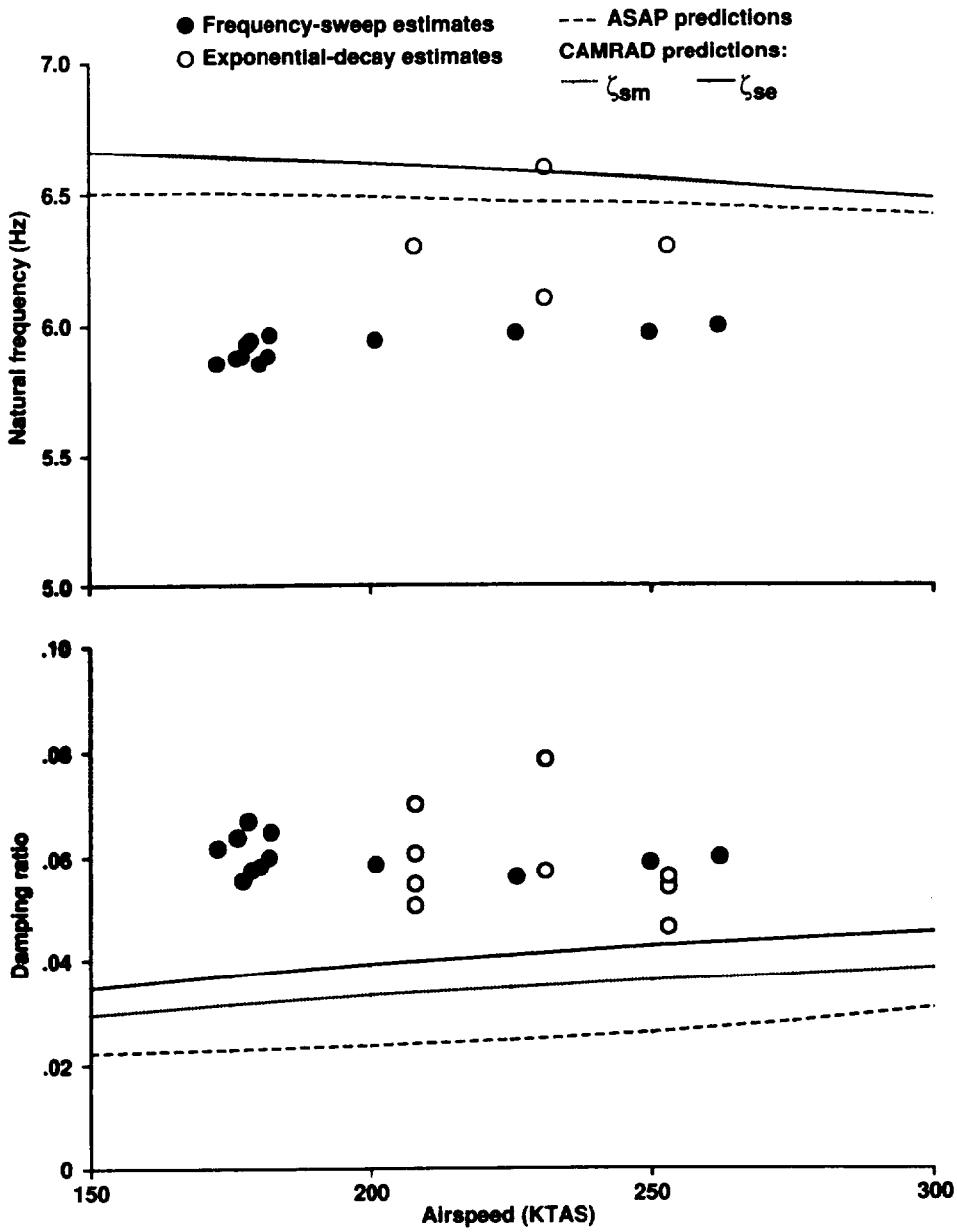

Figure 28. Continued. (b) Antisymmetric beam mode.

predictions of ζ are 0.04 to 0.06 lower than estimated and increase much less rapidly with airspeed. There is an abrupt decrease at the last, highest speed estimate of ζ, but it cannot be determined whether this reflects a true change in slope or whether it is merely caused by scatter.

Although antisymmetric chord and torsion, as estimated by NAVFIT, have the same natural frequency at the baseline point (table 2), there is a statistically significant difference between the estimated slopes of the two modal frequencies (table 3). Furthermore, the damping values for these two modes are clearly different in magnitude and slope (figs. 28(d) and 28(f)). This shows that the chord and torsion strain gages have low enough crosstalk for the frequency-domain method to resolve two very close modes.

In a few cases, the frequency-domain estimates appear to vary nonlinearly with airspeed, contrary to the roughly linear predictions, but it has not been proven that any such instance indicates a real aeroelastic phenomenon. Even at worst, the overall consistency of the estimates is adequate for reliable detection of incipient

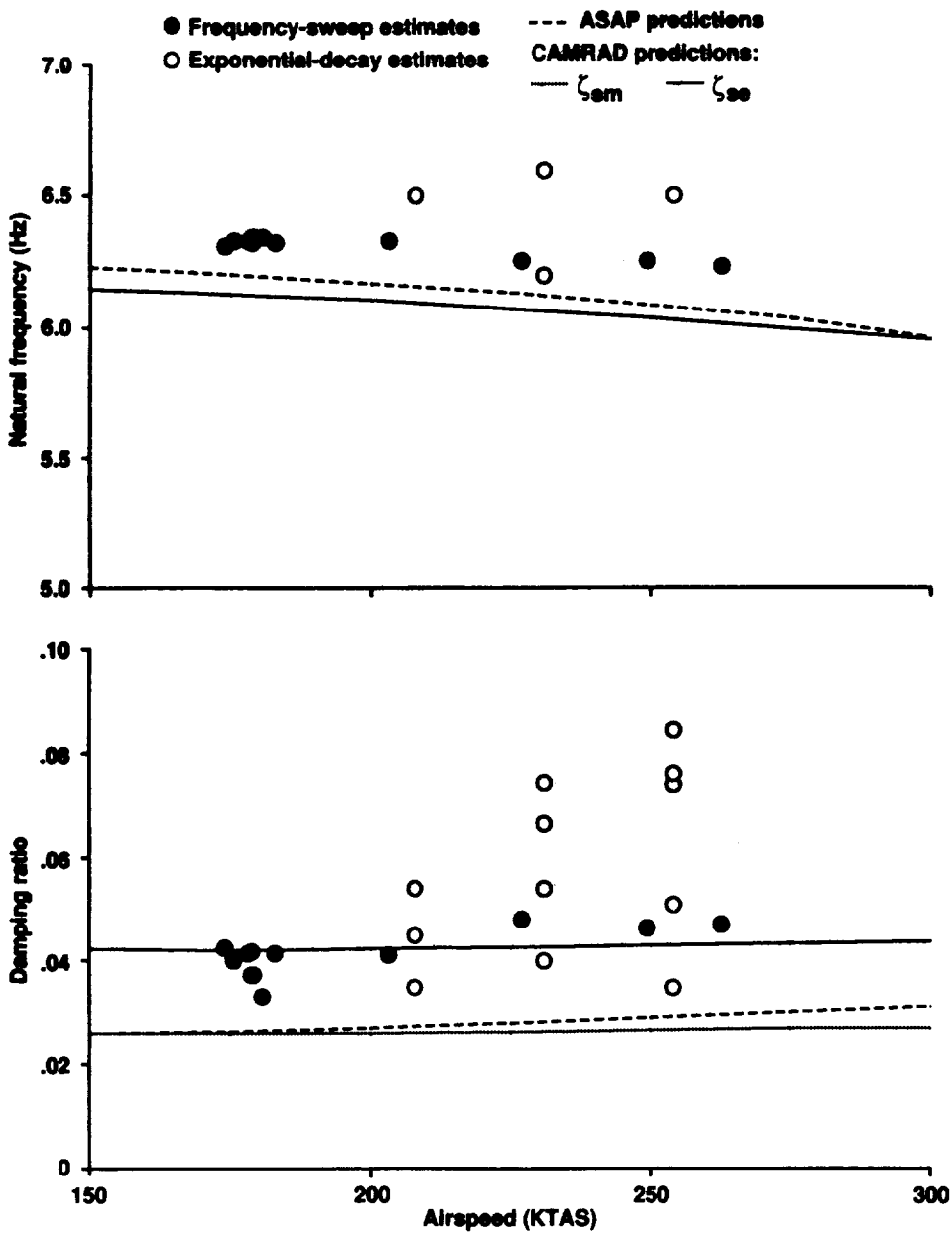

Figure 28. Continued. (c) Symmetric chord mode.

aeroelastic instability, which is the goal of this development effort.

Additional Flight Data

In addition to the baseline and high-speed data taken at 10,000 ft, data were taken at 5,000 ft and 15,000 ft (nominal values). These data permitted limited investigation of the effects of airspeed on the modal parameters at 15,000 ft, and of the effects of altitude at constant airspeed (150 KIAS). Maximum-power climbs and power-off descents were performed at 150 KIAS at 10,000 ft to illustrate the effects of power. Very limited data were also obtained at 10,000 ft at 98% rotor speed. CAMRAD predictions were computed for all of these cases and are plotted with the flight data in figures 29-36, discussions of which follow. Note that the scales of the plots are different from those of figure 28 and vary from plot to plot to reveal the data as clearly as possible.

High-altitude data– A limited number of data points were obtained at 15,000 ft, at 150, 190, and 210 KIAS.

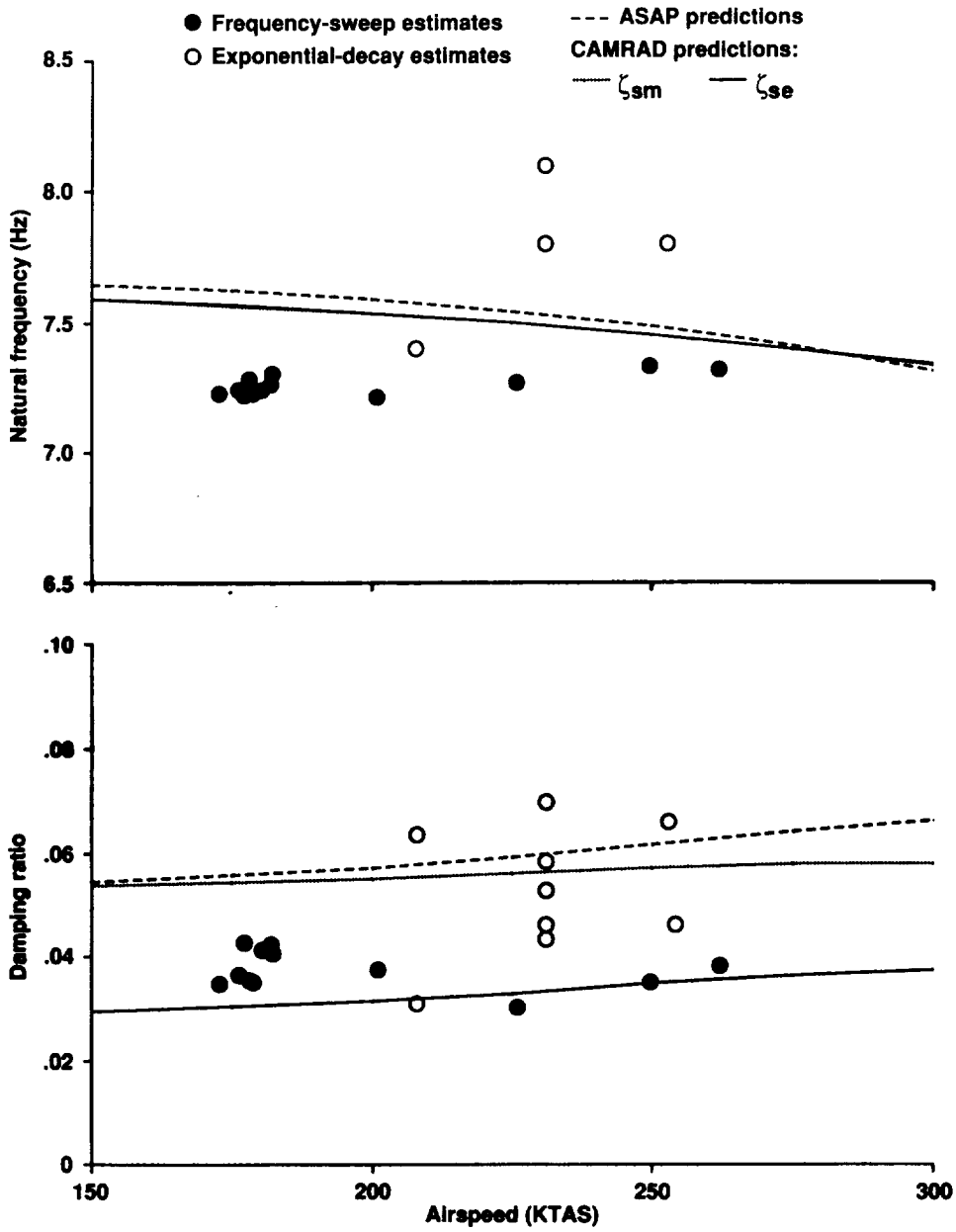

Figure 28. Continued. (d) Antisymmetric chord mode.

The density altitude actually reached was slightly over 14,000 ft, with true airspeeds near 190, 250, and 275 knots. To give an idea of the effect of the difference between the nominal and true altitudes, CAMRAD predictions were calculated for density altitudes of both 14,000 and 15,000 ft. Both sets of predictions are plotted in figures 29 and 30, along with the frequency-domain mode estimates derived from the flight data.

No rigorous conclusions can be drawn with only three data points, but an overall inspection of the figures is nevertheless instructive. In four cases (symmetric torsion ζ, antisymmetric beam f_n and ζ, and antisymmetric torsion f_n), the slopes of the mode estimates versus airspeed are clearly different from those predicted by CAMRAD. The symmetric-chord estimates of f_n and ζ appear to show nonlinearities that match the CAMRAD estimates; a similar effect is visible for symmetric beam ζ, but shifted in airspeed. However, all nonlinear matches are questionable with so few data points. No reliable conclusions at all can be drawn for damping for antisymmetric chord or torsion. In the remaining cases, the frequency-domain estimates appear to follow the

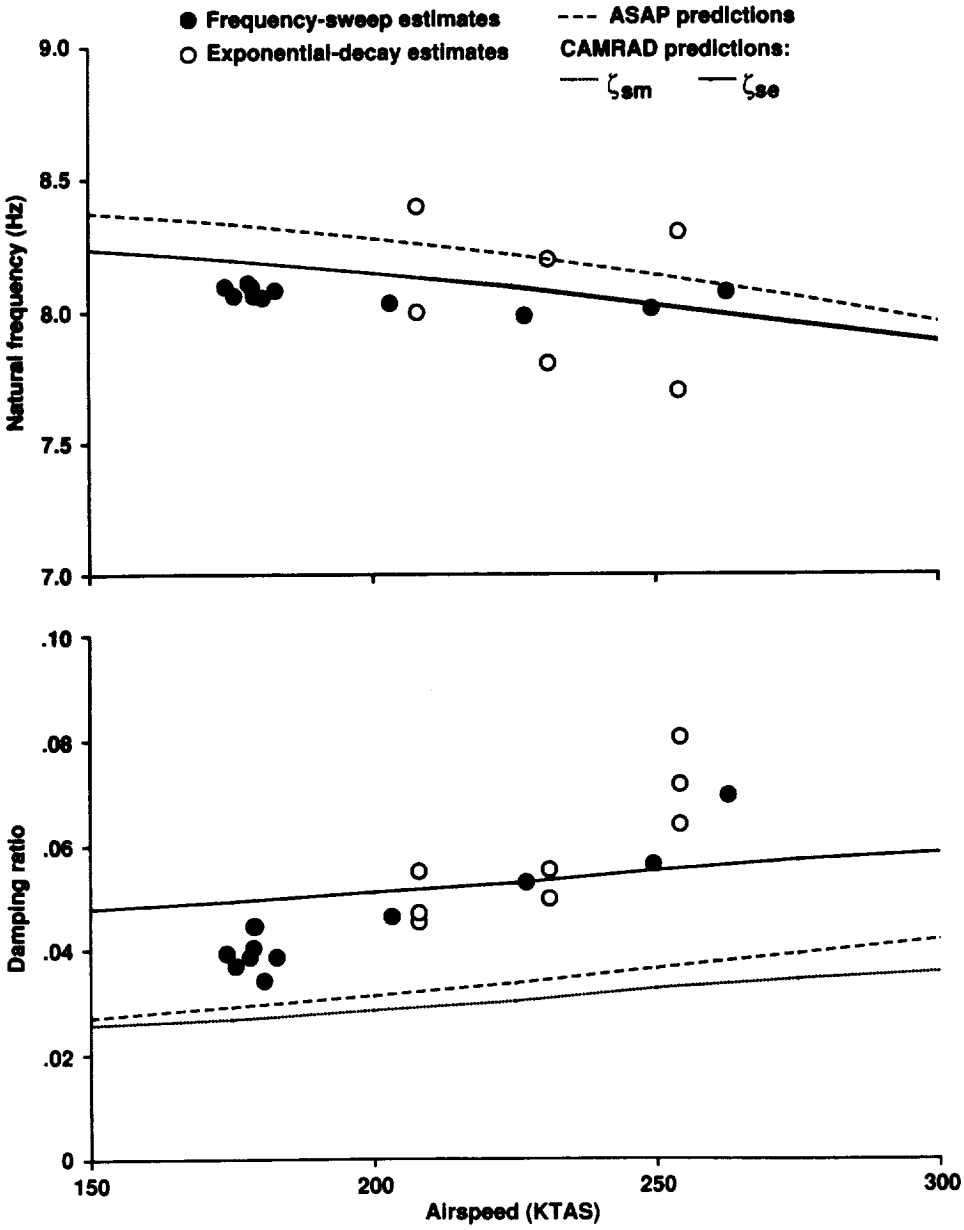

Figure 28. Continued. (e) Symmetric torsion mode.

CAMRAD predictions, but in nearly all cases, there is a significant offset in average value.

Altitude variations– Aeroelastics data were acquired at 150 KIAS at a density altitude of 5,000 ft. The resulting mode estimates are plotted in figures 31 and 32 along with the 150-KIAS data point at 15,000 ft and the 10,000-ft baseline data, to reveal the trends of modal frequencies and damping with changing altitude. Because true airspeed varies with altitude for a constant indicated airspeed, CAMRAD predictions were calculated for the following flight conditions (which correspond to a constant 150 KIAS): 5000 ft at 165 KTAS; 10,000 ft at 175 KTAS; and 15,000 ft at 190 KTAS. These values correspond to the conditions actually achieved in flight (see appendix A). For reference, CAMRAD predictions were also calculated for the same altitudes at a constant 175 KTAS. Both sets of predictions are plotted in the figures for comparison with the frequency-domain estimates.

The solid symbols in figures 31 and 32 denote data taken when the aircraft was within weight limits defined by the weights actually flown at the 5000-ft and 15,000-ft points. In virtually every case, these points define obvious

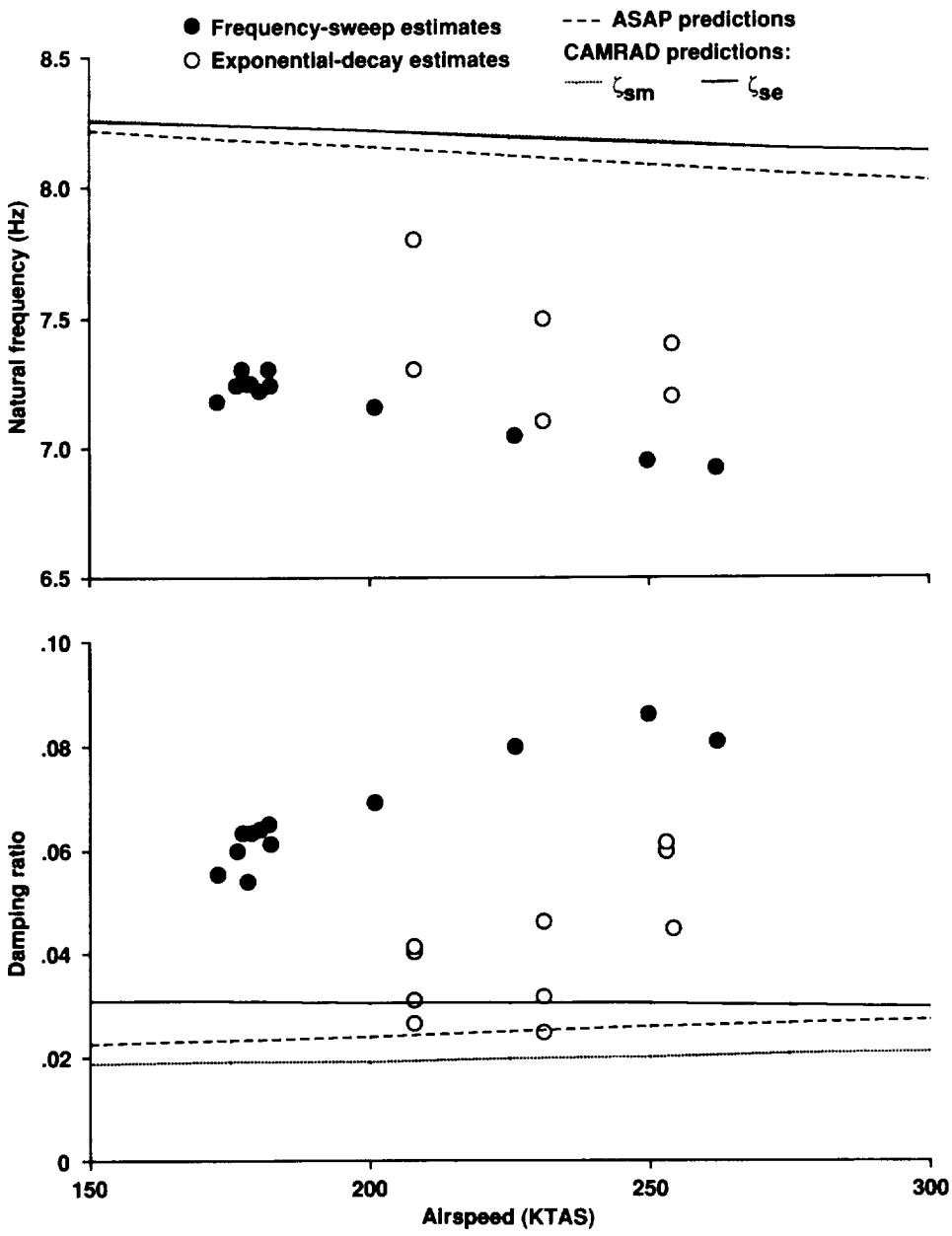

Figure 28. Concluded. (f) Antisymmetric torsion mode.

linear trends with changing altitude, standing out clearly from the scatter at the baseline flight condition. No other parameter, including power and airspeed, reveals the trends with such consistency, nor does any parameter do so in the plots of power or rotor speed variations (discussed below).

This result appears to conflict with the finding discussed earlier that very few modal parameters were significantly correlated with gross weight. Two interpretations suggest themselves: (1) the effects of gross weight are real, but are usually obscured by poor experimental design or low data quality, altitude variations being the one exception; or (2) the apparent effects are purely coincidental or are correlated with some unknown or unmeasured effect (such as wing lift distribution). The issue cannot be resolved with the limited number of data points available.

Power variations– By climbing and diving at maximum and minimum power at constant indicated airspeed (150 KIAS) and taking data at constant altitude (10,000 ft), the effects of rotor power on the modal parameters could be studied. Figures 33 and 34 show the

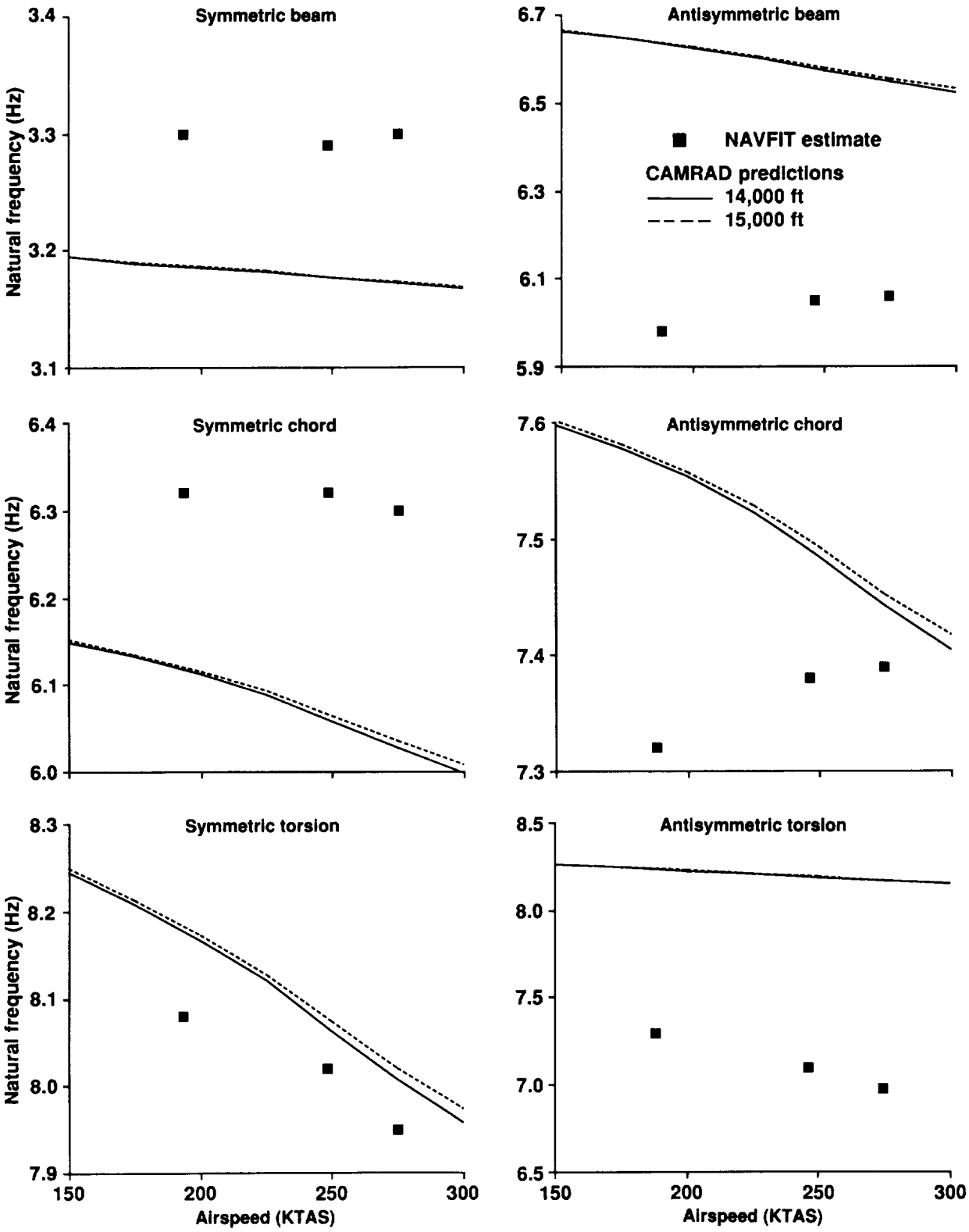

Figure 29. NAVFIT estimates and CAMRAD predictions of f_n versus airspeed at high altitude (15,000 ft nominal).

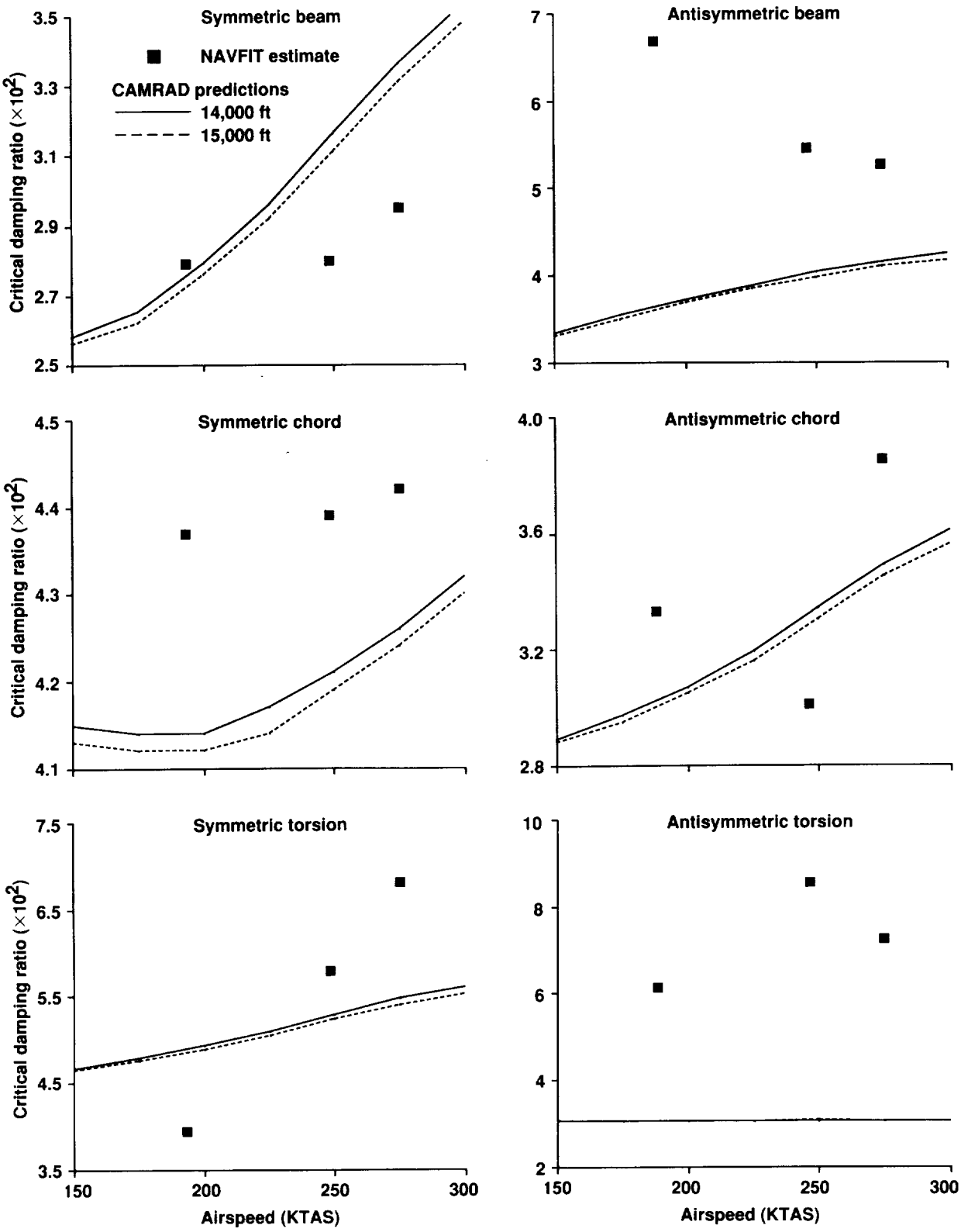

Figure 30. NAVFIT estimates and CAMRAD predictions of ζ versus airspeed at high altitude (15,000 ft nominal).

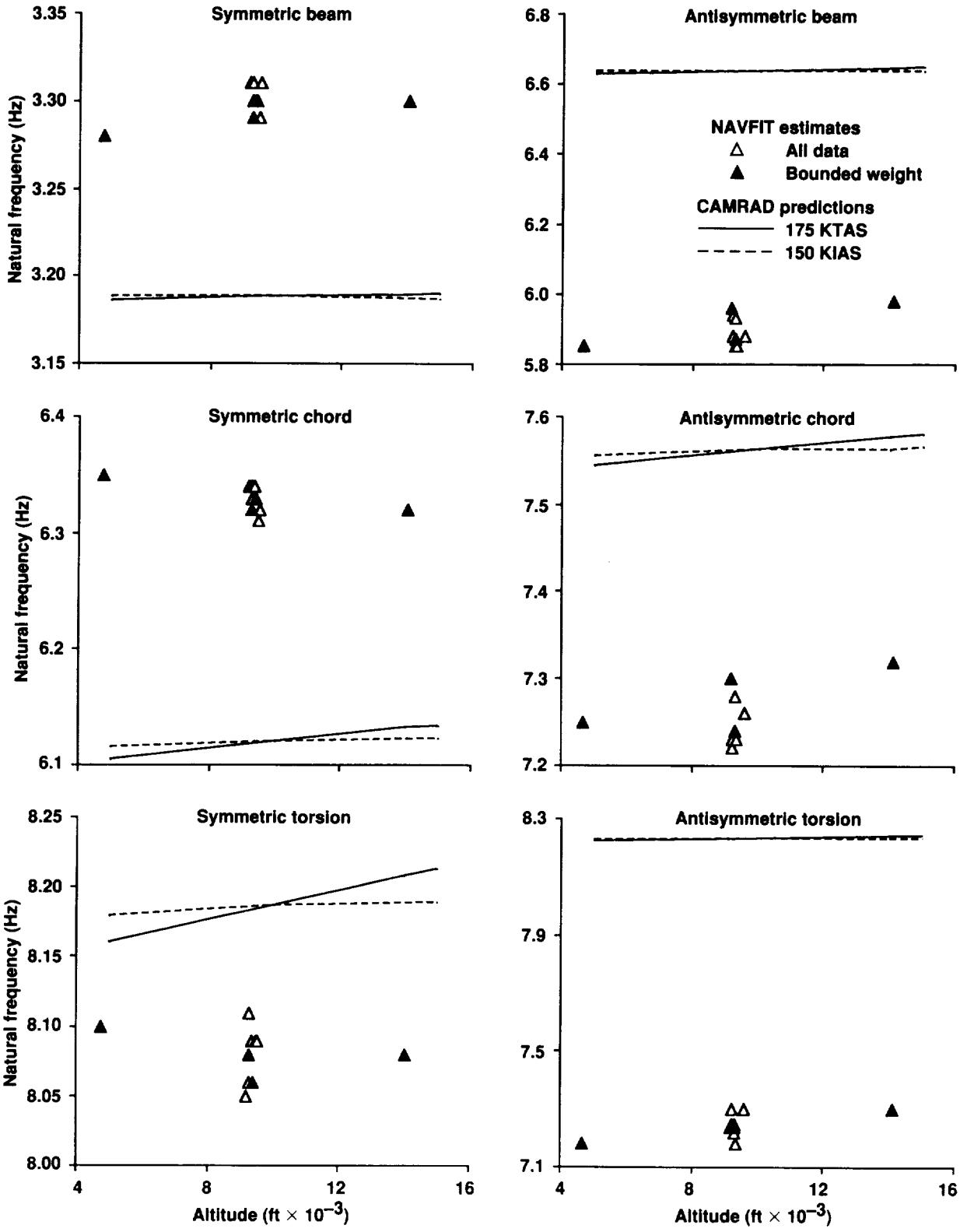

Figure 31. NAVFIT estimates and CAMRAD predictions of f_n versus altitude at constant airspeed (150 KIAS).

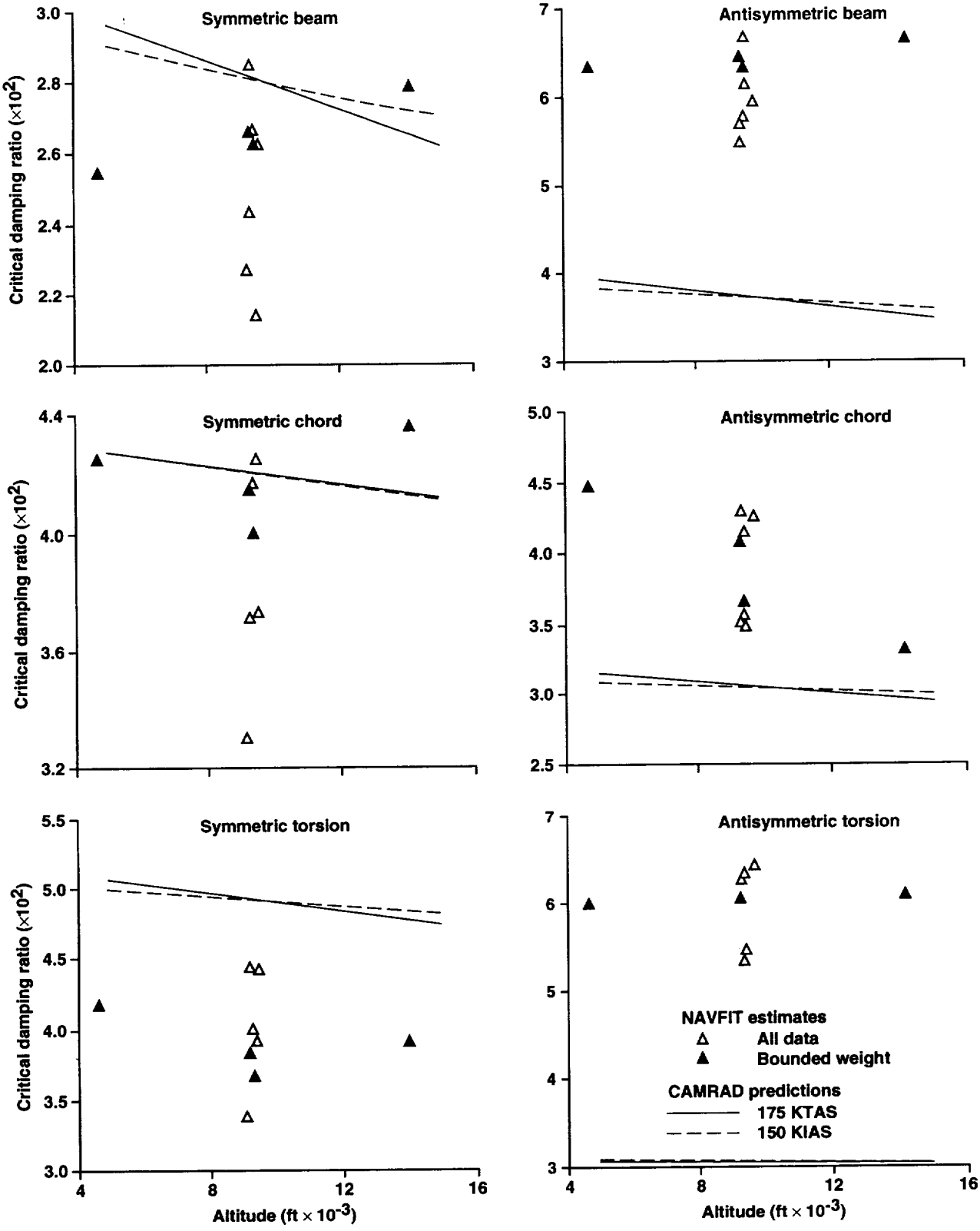

Figure 32. NAVFIT estimates and CAMRAD predictions of ζ versus altitude at constant airspeed (150 KIAS).

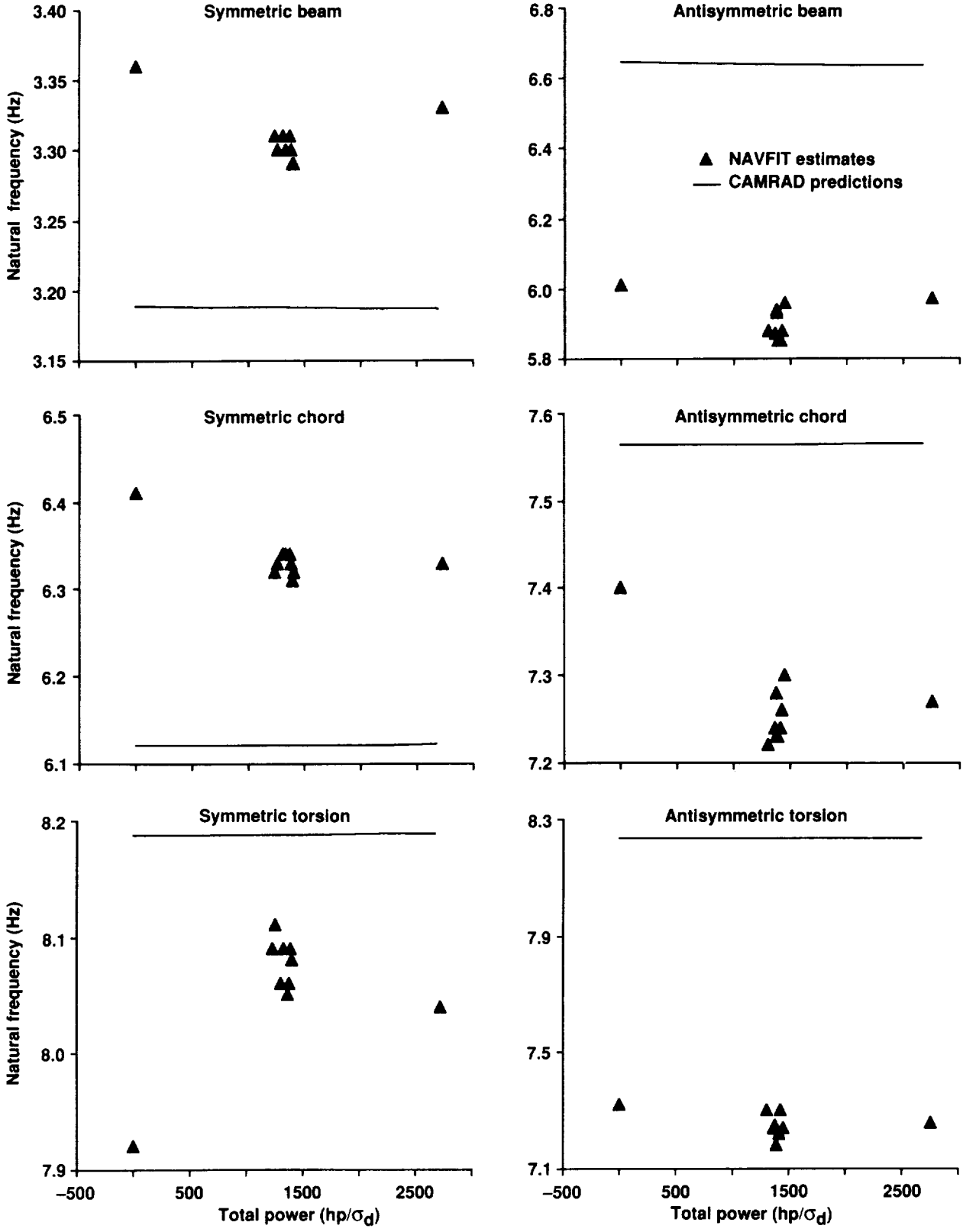

Figure 33. NAVFIT estimates and CAMRAD predictions of f_n versus power (descent, level flight, and climb) at constant airspeed.

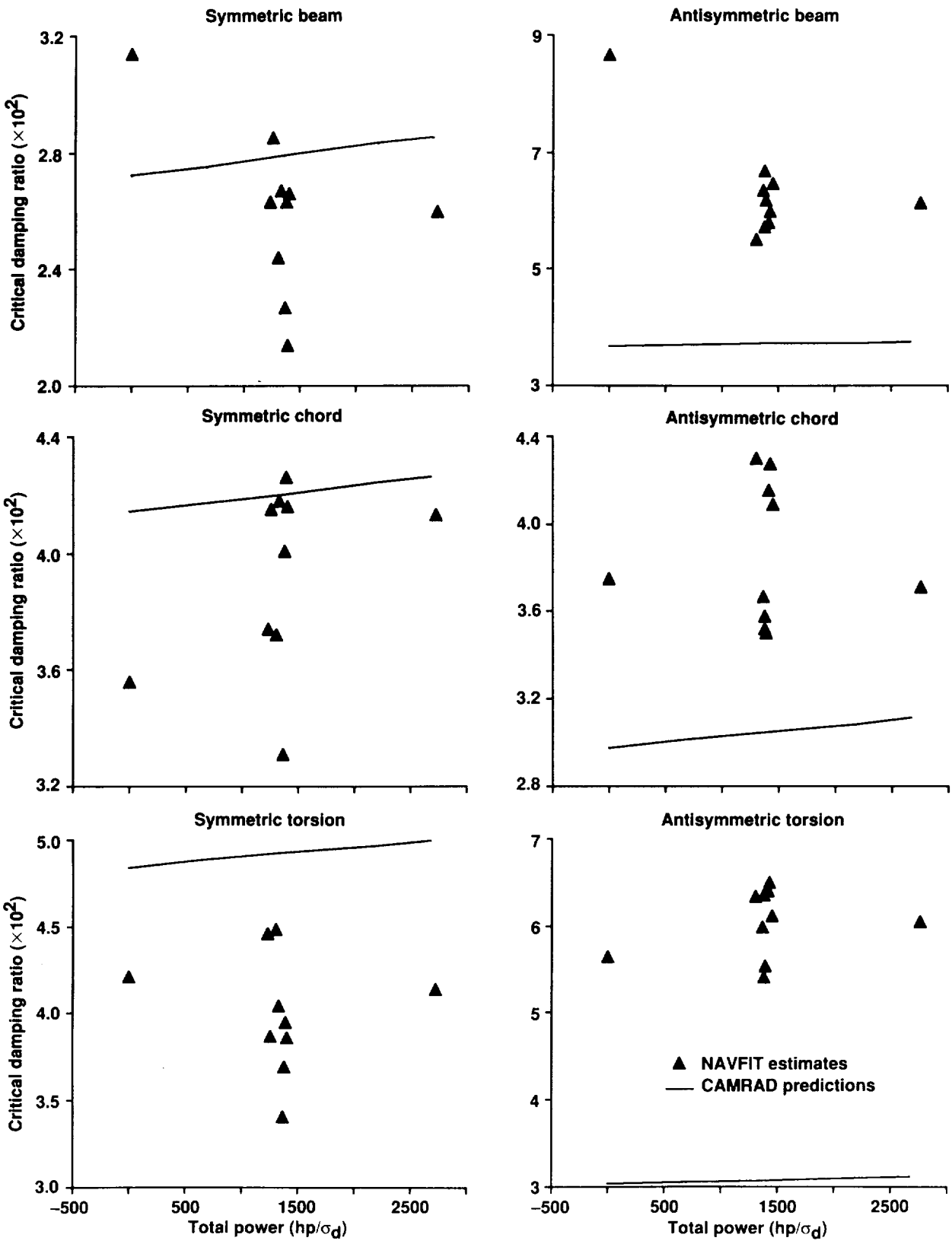

Figure 34. NAVFIT estimates and CAMRAD predictions of ζ versus power (descent, level flight, and climb) at constant airspeed.

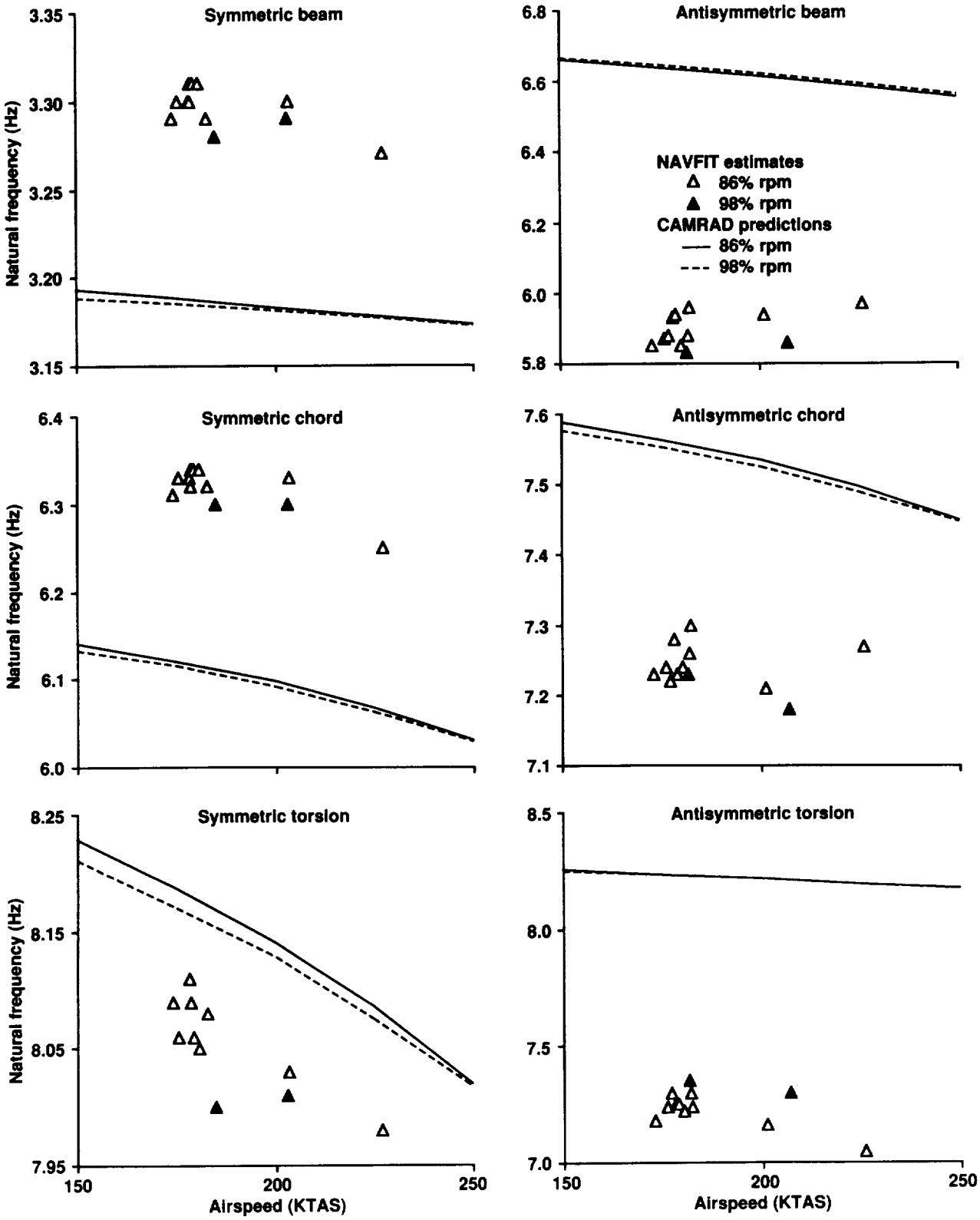

Figure 35. NAVFIT estimates and CAMRAD predictions of f_n versus airspeed at 86% and 98% rotor speed.

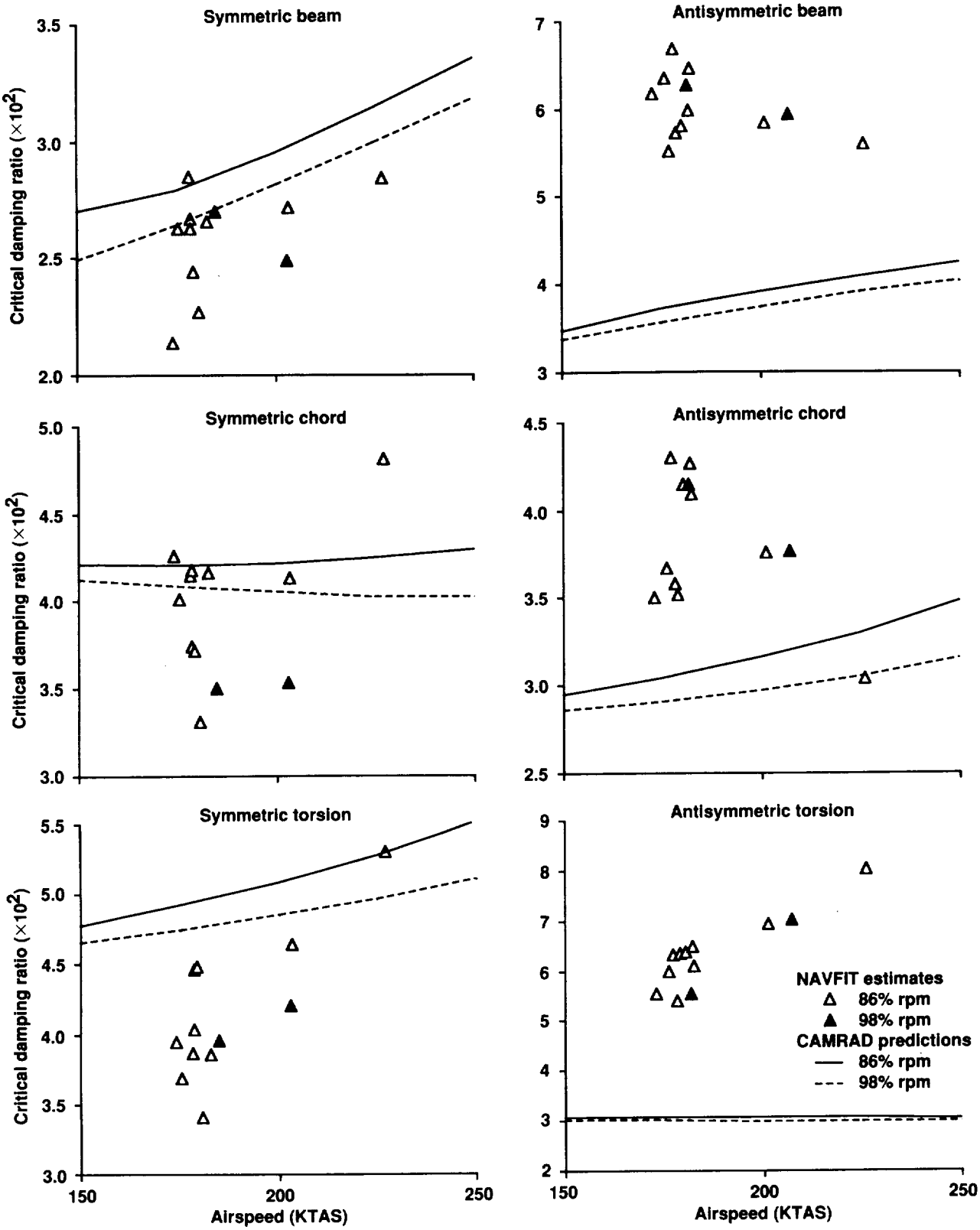

Figure 36. NAVFIT estimates and CAMRAD predictions of ζ versus airspeed at 86% and 98% rotor speed.

resulting mode estimates and corresponding CAMRAD predictions. The baseline data were all taken at about half maximum power and are also plotted. The values used for power are referred power, which is shaft horsepower (hp) normalized by the air density ratio (σ_d). At minimum power, the aircraft measurements of shaft power become erratic and unreliable; these values are shown as zero power in the figures.

The scatter in the baseline frequency-domain estimates was usually large compared with the slopes of the estimates with increasing power, and was sometimes large compared with the difference between the estimates and the CAMRAD predictions. Furthermore, no other parameters (weight, airspeed, or altitude) were found to interact with power in such a way as to consistently define linear slopes (analogous to the effect of weight in figures 31 and 32). Inspection of figures 33 and 34 reveals only a few cases of a consistent, linear or nearly linear slope, generally for the antisymmetric modes.

As usual, there were considerable offsets between the estimates and the CAMRAD predictions, somewhat exaggerated by the expanded plot scales.

Rotor speed variations– An attempt was made to determine the effects of airspeed on the aeroelastic modes at 98% rotor speed (589 rpm), which is the normal rotor speed for low-speed (helicopter mode and tilt-rotor mode) flight. However, the effort was curtailed after data were taken for two airspeed points (150 and 170 KIAS), because of high dynamic loads at the non-optimum rotor speed. (Aeroelastic stability itself was not a problem.)

The data obtained are shown in figures 35 and 36. The 86%-rotor-speed baseline data are also plotted, as are two airspeeds for the 86%-rotor-speed high-speed data; these data together serve to bracket the speed range covered by the 98%-rotor-speed data. CAMRAD predictions for 98% and 86% rotor speed are also plotted.

Overall, there is little difference between the two rotor speeds for any of the modes. Flight over a greater range of rotor speeds is possible, but not desirable, because of poor aircraft performance and high dynamic loads. A full set of rotor speed variations, even with enough different values for good statistics, would probably be of little value because of the small size of the expected effects compared with the scatter in the baseline estimates.

CONCLUDING REMARKS

Frequency-sweep excitation combined with frequency-domain analysis was demonstrated to be a reliable and efficient way of determining XV-15 aeroelastic behavior from flight data, permitting good estimations of all modes. Dual-flaperon excitation plus sum-and-difference signal processing yielded good time-history data for each mode, and chirp z-transform Fourier analysis generated excellent spectra. The estimates of modal frequencies and damping ratios were based on curve fits to frequency responses; the estimates varied linearly with airspeed and were highly repeatable at a reference flight condition (within less than 1% relative error for natural frequency and 9% relative error for damping). These results were significant improvements over the older exponential-decay method. Because of the good analytical results shown here and the reduced flight-test time compared with other methods, the frequency-sweep method has been chosen to support flight tests of the new XV-15 composite blades (ATBs).

Obvious improvements would be to replicate all flight-test conditions beyond the baseline point and to extend the speed range to both higher and lower airspeeds, thereby permitting more accurate determination of the trends of frequency and damping with changing airspeed with more complete statistics. Gross weight cannot be kept constant, but given a greater range of weights and enough replications, the effects of weight could be more reliably determined and distinguished from the effects of airspeed.

A more subtle change would be to reduce the speed at which the flaperons sweep through the frequency range. The ideal procedure is to have very slow sweeps, repeated many times at each test condition, with several replications of each condition. Unfortunately, this would require an excessive amount of flight-test time. In initial tests of the ATBs, slower sweeps will be used over a reduced frequency range to explicitly study the trade-off in accuracy between sweep rate and number of sweeps per test point.

Improvements are also possible for the analytical predictions. CAMRAD and ASAP are both being continually upgraded, and new predictions will be made for the XV-15 as improved programs become available. A ground vibration test of the XV-15 using the frequency-sweep techniques described here is planned, with the goal of obtaining better estimates of zero-airspeed structural frequencies and damping. Such results could be fed into the CAMRAD and ASAP models for further improvements in the predictions of aeroelastic stability.

Ames Research Center
National Aeronautics and Space Administration
Moffett Field, California
October 5, 1990

APPENDIX A

TEST POINTS AND TABULATED RESULTS

Tables A1 and A2 list the modal frequencies and damping for all flight conditions flown. Table A1 lists the results for the flight conditions on which most of the analyses reported herein were based: level flight at 10,000 ft density altitude and 86% rotor speed. All baseline points are included. Table A2 lists the results for the other flight conditions: level flight at 5,000 and 15,000 ft; maximum-power climbs and power-off (windmilling) descents, and 98% rotor speed at 10,000 ft. The averaged baseline values are included for ease of comparison.

Tables A3 through A5 list all individual sweeps and relevant aircraft data for each sweep, organized by flight number, test condition, and counter. The counter is the numerical label for each data record in the TRENDS data base (ref. 19). Tables A6 through A8 list all sweeps by flight in order of counter, with the TRENDS counter descriptions (based on the pilots' comments and the flight cards). (No aeroelastics data were taken on flight 227.)

The structure and notation of tables A3 through A8 have been kept similar to that generated by TRENDS for ease of comparison with other XV-15 flight data. Power is normalized by air density ratio σ_d. Gross weight is corrected for known anomalies in the fuel-flow and fuel-quantity instrumentation; the corrections were made by James A. Weiberg of NASA Ames Research Center. The baseline points are numbered not in chronological order, but in the order in which fully verified data were made available in TRENDS for analysis. The repetition-test data overlap baseline #4; although not discussed in this report, the repetition-test counters are included in the tables for completeness.

By referencing the appropriate tables, the reader should be able to identify the exact counter(s) in TRENDS needed to duplicate the results reported herein or to apply different analyses for comparison.

Table A1. XV-15 frequency and damping estimates for 10,000-ft level flight

Flight condition	Symmetric beam		Antisymmetric beam		Symmetric chord		Antisymmetric chord		Symmetric torsion		Antisymmetric torsion	
	f_n (Hz)	ζ	f_n (Hz)	ζ	f_n (Hz)	ζ	f_n (Hz)	ζ	f_n (Hz)	ζ	f_n (Hz)	ζ
Baseline:												
#1	3.29	0.0266	5.96	0.0646	6.32	0.0416	7.30	0.0409	8.08	0.0386	7.24	0.0611
#2	3.31	0.0263	5.88	0.0598	6.32	0.0374	7.26	0.0427	8.09	0.0446	7.30	0.0649
#3	3.31	0.0227	5.88	0.0552	6.34	0.0331	7.22	0.0430	8.05	0.0341	7.30	0.0633
#4	3.30	0.0263	5.87	0.0635	6.33	0.0401	7.24	0.0367	8.06	0.0369	7.24	0.0598
#5	3.29	0.0214	5.85	0.0617	6.31	0.0426	7.23	0.0350	8.09	0.0395	7.18	0.0553
System tests:												
SCAS off	3.31	0.0244	5.85	0.0580	6.34	0.0372	7.24	0.0415	8.06	0.0448	7.22	0.0639
ARS off	3.30	0.0267	5.93	0.0668	6.34	0.0418	7.28	0.0358	8.09	0.0404	7.25	0.0541
FFS off	3.30	0.0285	5.94	0.0573	6.33	0.0415	7.23	0.0352	8.11	0.0387	7.25	0.0634
Speed sweep:												
150 KIAS*	3.30	0.0254	5.90	0.0609	6.33	0.0394	7.25	0.0389	8.08	0.0397	7.25	0.0607
170 KIAS	3.30	0.0272	5.94	0.0584	6.33	0.0413	7.21	0.0376	8.03	0.0464	7.16	0.0693
190 KIAS	3.27	0.0284	5.97	0.0559	6.25	0.0481	7.27	0.0304	7.98	0.0530	7.05	0.0801
210 KIAS	3.29	0.0302	5.97	0.0589	6.25	0.0462	7.33	0.0354	8.01	0.0565	6.95	0.0861
V_{max}	3.28	0.0328	6.00	0.0599	6.23	0.0471	7.32	0.0384	8.07	0.0696	6.92	0.0809

*Averaged baseline values.

Table A2. XV-15 frequency and damping estimates for additional flight conditions

Flight condition	Symmetric beam		Antisymmetric beam		Symmetric chord		Antisymmetric chord		Symmetric torsion		Antisymmetric torsion	
	f_n (Hz)	ζ	f_n (Hz)	ζ	f_n (Hz)	ζ	f_n (Hz)	ζ	f_n (Hz)	ζ	f_n (Hz)	ζ
Altitude variations*:												
5,000 ft	3.28	0.0255	5.85	0.0635	6.35	0.0426	7.25	0.0448	8.10	0.0421	7.18	0.0606
10,000 ft†	3.30	0.0254	5.90	0.0609	6.33	0.0394	7.25	0.0389	8.08	0.0397	7.25	0.0607
15,000 ft	3.30	0.0279	5.98	0.0668	6.32	0.0437	7.32	0.0333	8.08	0.0394	7.30	0.0615
Power variations*:												
Power-off descent	3.36	0.0314	6.01	0.0867	6.41	0.0356	7.40	0.0375	7.92	0.0421	7.32	0.0565
Cruise power†	3.30	0.0254	5.90	0.0609	6.33	0.0394	7.25	0.0389	8.08	0.0397	7.25	0.0607
Max-power climb	3.33	0.0260	5.97	0.0612	6.33	0.0413	7.27	0.0371	8.04	0.0414	7.26	0.0605
Speed sweep, 15,000 ft:												
150 KIAS	3.30	0.0279	5.98	0.0668	6.32	0.0437	7.32	0.0333	8.08	0.0394	7.30	0.0615
190 KIAS	3.29	0.0280	6.05	0.0545	6.32	0.0439	7.38	0.0301	8.02	0.0580	7.10	0.0858
210 KIAS	3.30	0.0295	6.06	0.0527	6.30	0.0442	7.39	0.0385	7.95	0.0682	6.98	0.0725
98% Rotor speed:												
150 KIAS	3.28	0.0270	5.83	0.0626	6.30	0.0350	7.23	0.0415	8.00	0.0396	7.35	0.0554
170 KIAS	3.29	0.0249	5.86	0.0593	6.30	0.0353	7.18	0.0377	8.01	0.0421	7.30	0.0703

*150 KIAS, 86% rpm.

†Averaged baseline values.

Table A3. Test-point conditions for flight 225

FLIGHT 225: BASELINE DATA

P002.AVS	AIRSPEED-NOSE BOOM (KIAS)	KNOTS
KCAS.AVS	CALIBRATED AIRSPEED	KNOTS
KTAS.AVS	TRUE AIRSPEED	KNOTS
R106.AVS	ROTOR RPM	%
HDFT.AVS	DENSITY ALTITUDE	FEET
RHPN.AVS	NORMALIZED HP (RSHP/SIGMA)	HP
GWJW.AVS	GROSS WEIGHT BY JIM WEIBERG	LBS

Counter	KIAS	KCAS	KTAS	RPM, %	HD, ft	RHPN	Weight, lb
BASELINE #4:							
12747	143.57	152.09	175.53	86.58	9309.44	693	13353.36
12748	143.58	152.10	175.80	86.53	9385.69	692	13342.18
12749	143.15	151.65	175.42	86.52	9459.74	679	13333.45
12752	142.94	151.43	174.43	86.54	9278.28	661	13304.87
12753	145.31	153.91	177.42	86.53	9300.22	695	13285.84
12754	144.72	153.29	176.97	86.55	9383.29	694	13275.00
SCAS OFF:							
12757	147.22	155.91	179.56	86.34	9237.71	712	13217.08
12758	147.23	155.92	179.73	86.31	9308.59	713	13208.26
12759	148.82	157.58	181.69	86.39	9324.81	702	13200.18
12760	146.10	154.73	178.47	86.27	9345.96	651	13191.22
12761	146.99	155.66	179.31	86.32	9274.94	654	13183.23
12762	147.65	156.35	179.80	86.32	9181.66	654	13174.75
ARS OFF:							
12799	146.63	155.29	179.01	86.40	9233.44	695	13201.07
12800	144.84	153.42	177.15	86.46	9325.35	691	13190.50
12801	145.79	154.41	178.28	86.47	9348.31	690	13174.24
12802	146.81	155.48	179.59	86.39	9364.91	690	13160.28
12803	145.76	154.38	178.38	86.54	9391.98	652	13150.34
12804	145.69	154.31	178.11	86.53	9324.45	648	13140.46
FFS OFF:							
12805	145.41	154.01	177.37	86.61	9191.33	685	13106.36
12806	146.88	155.55	179.42	86.53	9249.90	692	13096.25
12807	147.15	155.83	179.51	86.47	9234.52	698	13085.34
12808	145.89	154.52	178.50	86.54	9346.44	637	13073.01
12809	147.66	156.37	180.32	86.62	9246.06	634	13062.82
12810	143.67	152.19	175.54	86.53	9211.33	614	13052.00

Table A3. (Continued.)

FLIGHT 225: SPEED SWEEP DATA

P002.AVS	AIRSPEED-NOSE BOOM (KIAS)	KNOTS
KCAS.AVS	CALIBRATED AIRSPEED	KNOTS
KTAS.AVS	TRUE AIRSPEED	KNOTS
R106.AVS	ROTOR RPM	%
HDFT.AVS	DENSITY ALTITUDE	FEET
RHPN.AVS	NORMALIZED HP (RSHP/SIGMA)	HP
GWJW.AVS	GROSS WEIGHT BY JIM WEIBERG	LBS

Counter	KIAS	KCAS	KTAS	RPM, %	HD, ft	RHPN	Weight, lb
BASELINE #5:							
12824	141.22	149.63	172.90	86.06	9330.87	685	13555.16
12825	141.23	149.64	172.76	85.95	9302.00	701	13545.42
12826	141.32	149.74	172.99	86.06	9364.97	706	13536.59
12827	142.07	150.52	174.07	85.98	9424.39	694	13528.15
12828	140.96	149.36	173.01	85.93	9509.47	684	13518.81
12829	142.90	151.39	175.16	85.93	9456.60	704	13511.30
12764	162.65	172.03	198.66	86.30	9375.93	788	13137.22
12765	165.02	174.51	201.37	86.26	9358.21	790	13126.63
12766	166.71	176.28	203.40	86.29	9353.26	792	13114.46
12767	166.94	176.52	203.62	86.30	9334.44	790	13105.53
12768	166.53	176.09	203.11	86.33	9337.15	788	13097.53
12769	166.24	175.79	202.75	86.34	9332.63	788	13089.64
12777	184.67	195.05	224.70	86.76	9347.11	979	13533.65
12778	189.08	199.66	229.67	86.70	9304.50	1039	13522.92
12779	185.99	196.43	226.52	86.80	9410.68	975	13511.22
12780	186.42	196.88	226.92	86.87	9364.21	979	13499.55
12781	186.02	196.46	226.54	86.82	9339.75	974	13489.07
12783	184.29	194.65	224.19	86.82	9300.13	985	13471.72
12785	203.72	214.96	247.98	86.51	9437.92	1230	13412.80
12786	206.76	218.14	251.59	86.61	9463.63	1269	13401.51
12787	204.81	216.10	249.61	86.53	9549.62	1208	13391.11
12788	204.69	215.97	249.28	86.58	9494.10	1188	13379.21
12789	204.49	215.76	248.94	86.62	9446.40	1179	13368.98
12790	206.03	217.37	250.33	86.49	9354.90	1178	13356.78
12792	216.45	228.26	262.80	86.58	9446.66	1361	13309.82
12793	216.70	228.53	262.94	86.46	9403.61	1333	13299.72
12794	216.68	228.50	262.72	86.52	9355.75	1355	13289.49
12795	216.84	228.67	262.82	86.41	9329.15	1339	13279.24
12796	215.00	226.75	260.92	86.48	9371.84	1362	13268.47
12797	216.05	227.85	262.35	86.50	9409.39	1375	13258.02

Table A3. (Concluded.)

FLIGHT 225: ADDITIONAL DATA

P002.AVS	AIRSPEED-NOSE BOOM (KIAS)	KNOTS
KCAS.AVS	CALIBRATED AIRSPEED	KNOTS
KTAS.AVS	TRUE AIRSPEED	KNOTS
R106.AVS	ROTOR RPM	%
HDFT.AVS	DENSITY ALTITUDE	FEET
RHPN.AVS	NORMALIZED HP (RSHP/SIGMA)	HP
GWJW.AVS	GROSS WEIGHT BY JIM WEIBERG	LBS

Counter	KIAS	KCAS	KTAS	RPM, %	HD, ft	RHPN	Weight, lb
REPETITION TEST:							
12747	143.57	152.09	175.53	86.58	9309.44	693	13353.36
12748	143.58	152.10	175.80	86.53	9385.69	692	13342.18
12749	143.15	151.65	175.42	86.52	9459.74	679	13333.45
12750	141.21	149.62	172.94	86.59	9466.58	637	13324.71
12751	141.98	150.43	173.59	86.57	9367.24	637	13314.51
12752	142.94	151.43	174.43	86.54	9278.28	661	13304.87
12753	145.31	153.91	177.42	86.53	9300.22	695	13285.84
12754	144.72	153.29	176.97	86.55	9383.29	694	13275.00
12755	148.53	157.27	181.39	86.41	9335.11	696	13265.31
12756	138.96	147.27	169.54	86.31	9203.55	632	13235.55
5,000 ft DENSITY ALTITUDE:							
12831	143.20	151.70	163.26	85.87	4808.46	560	13444.31
12832	145.48	154.09	165.84	85.83	4785.11	526	13436.34
12833	146.02	154.65	166.25	85.96	4709.37	548	13415.91
12834	144.63	153.20	164.43	85.76	4622.22	543	13406.79
12835	143.47	151.99	163.22	85.83	4632.52	553	13398.77
12836	142.36	150.83	162.10	85.81	4671.85	553	13390.95

Table A4. Test-point conditions for flight 226

FLIGHT 226: SPEED SWEEP & CLIMB & DESCENT DATA

P002.AVS	AIRSPEED-NOSE BOOM (KIAS)	KNOTS
KCAS.AVS	CALIBRATED AIRSPEED	KNOTS
KTAS.AVS	TRUE AIRSPEED	KNOTS
R106.AVS	ROTOR RPM	%
HDFT.AVS	DENSITY ALTITUDE	FEET
RHPN.AVS	NORMALIZED HP (RSHP/SIGMA)	HP
GWJW.AVS	GROSS WEIGHT BY JIM WEIBERG	LBS

Counter	KIAS	KCAS	KTAS	RPM, %	HD, ft	RHPN	Weight, lb
15,000 ft SPEED SWEEP:							
12853	149.99	158.80	198.06	86.68	13974.58	961	13272.25
12854	141.57	150.00	187.66	86.72	14137.95	765	13261.78
12855	147.39	156.08	194.88	86.68	14030.29	883	13252.64
12856	142.72	151.20	189.25	86.56	14166.42	796	13240.90
12859	141.95	150.40	188.11	86.67	14115.94	787	13218.75
12860	140.92	149.32	186.74	86.69	14080.82	785	13209.42
12862	186.73	197.20	245.96	86.60	14195.42	1190	13156.94
12863	186.83	197.31	245.95	86.58	14161.32	1182	13147.14
12864	187.90	198.42	247.22	86.54	14133.33	1240	13137.86
12865	188.83	199.40	248.51	86.68	14166.64	1243	13129.18
12866	189.00	199.57	248.68	86.48	14165.61	1227	13120.81
12867	188.61	199.17	248.17	86.55	14176.36	1210	13109.24
12869	207.34	218.74	272.60	86.54	14347.66	1548	13062.76
12870	210.35	221.89	276.20	86.53	14275.13	1556	13054.20
12871	210.77	222.33	276.59	86.52	14242.67	1547	13045.62
12872	210.25	221.78	275.94	86.50	14237.73	1550	13035.87
12873	209.13	220.61	274.70	86.55	14295.28	1531	13027.28
12874	207.21	218.61	272.35	86.47	14335.88	1482	13017.27
WINDMILL DESCENT:							
12875	145.75	154.37	182.18	86.51	10392.35	n/a	12953.20
12877	141.36	149.78	175.66	86.50	9979.97	n/a	12893.81
12879	142.46	150.93	177.36	86.50	10155.18	n/a	12841.72
12881	144.09	152.63	177.11	86.65	9369.79	n/a	12790.89
12883	141.37	149.79	176.65	86.51	10332.69	n/a	12745.49
12885	142.81	151.30	175.91	86.53	9474.46	n/a	12703.12
MAXIMUM-POWER CLIMB:							
12876	144.69	153.26	179.62	86.57	9918.80	1379	12920.21
12878	144.53	153.09	178.76	86.61	9680.81	1364	12867.37
12880	145.69	154.31	181.29	86.66	10108.50	1389	12819.01
12882	143.63	152.15	177.69	86.73	9717.32	1387	12768.96
12884	140.53	148.91	174.60	86.64	9913.33	1366	12723.10
12886	142.24	150.70	173.90	86.55	8957.99	1323	12681.11

Table A5. Test-point conditions for flight 228

FLIGHT 228: BASELINE AND 98% RPM DATA

P002.AVS	AIRSPEED-NOSE BOOM (KIAS)	KNOTS
KCAS.AVS	CALIBRATED AIRSPEED	KNOTS
KTAS.AVS	TRUE AIRSPEED	KNOTS
R106.AVS	ROTOR RPM	%
HDFT.AVS	DENSITY ALTITUDE	FEET
RHPN.AVS	NORMALIZED HP (RSHP/SIGMA)	HP
GWJW.AVS	GROSS WEIGHT BY JIM WEIBERG	LBS

Counter	KIAS	KCAS	KTAS	RPM, %	HD, ft	RHPN	Weight, lb
BASELINE #1:							
13012	147.26	155.95	181.49	86.26	9105.99	738	13365.28
13013	150.34	159.17	185.22	86.27	9139.47	742	13356.72
13014	145.98	154.61	180.39	86.27	9291.62	696	13348.52
13015	146.62	155.28	181.00	86.24	9265.07	701	13287.93
13016	149.32	158.10	184.30	86.23	9256.73	700	13275.80
13017	148.20	156.93	183.06	86.18	9294.58	701	13267.55
98% RPM SPEED SWEEP:							
13019	150.86	159.71	186.25	97.90	9297.39	772	13223.28
13020	148.35	157.09	183.42	97.88	9348.16	743	13215.72
13021	149.68	158.48	184.89	97.87	9294.02	744	13207.66
13022	154.06	163.05	189.81	97.88	9149.85	747	13199.42
13023	143.73	152.26	177.90	97.76	9337.28	676	13190.81
13024	143.51	152.03	177.44	98.05	9270.62	680	13183.01
13026	165.90	175.43	204.81	98.10	9405.04	914	13153.27
13027	168.29	177.93	207.88	98.14	9461.05	933	13142.46
13028	169.32	179.00	209.22	98.12	9499.04	919	13133.82
13030	162.98	172.38	201.70	97.98	9562.18	847	13097.46
13031	161.33	170.65	199.82	98.13	9594.98	832	13090.08
13032	167.86	177.48	207.58	98.12	9549.02	939	13082.55
BASELINE #2:							
13034	148.62	157.37	184.19	87.16	9499.69	770	13035.70
13035	142.52	150.99	177.24	87.11	9689.06	627	13027.51
13036	148.53	157.27	184.41	87.09	9626.92	750	13019.35
13037	142.78	151.26	177.56	87.16	9667.00	610	13010.88
13038	144.33	152.88	179.01	87.20	9508.14	612	13003.28
13039	145.18	153.77	179.63	87.15	9377.21	633	12989.39
BASELINE #3:							
13041	144.52	153.08	178.37	87.13	9217.72	638	12950.00
13042	141.65	150.08	175.00	87.15	9257.59	639	12942.05
13043	144.41	152.97	178.19	87.17	9202.20	679	12932.09
13044	148.12	156.85	182.60	87.14	9160.47	685	12921.82
13045	146.30	154.94	180.46	87.01	9178.66	683	12914.16
13046	144.78	153.36	178.76	87.08	9234.70	682	12906.01

Table A6. TRENDS counter list for flight 225

		Pilot Comments	Duration, sec
FLT 225	CTR 12747	SYM SWEEP 150 KTS 86% RPM	39.3
FLT 225	CTR 12748	SYM SWEEP 150 KTS 86% RPM	33.4
FLT 225	CTR 12749	SYM SWEEP 150 KTS 86% RPM	32.0
FLT 225	CTR 12752	ASYM SWEEP 150 KTS 86% RPM	32.3
FLT 225	CTR 12753	ASYM SWEEP 150 KTS 86% RPM	32.7
FLT 225	CTR 12754	ASYM SWEEP 150 KTS 86% RPM	33.5
FLT 225	CTR 12757	ASYM SWEEP 150 KTS SCAS OFF	28.9
FLT 225	CTR 12758	ASYM SWEEP 150 KTS SCAS OFF	30.7
FLT 225	CTR 12759	ASYM SWEEP 150 KTS SCAS OFF	30.9
FLT 225	CTR 12760	SYM SWEEP 150 KTS SCAS OFF	31.9
FLT 225	CTR 12761	SYM SWEEP 150 KTS SCAS OFF	30.1
FLT 225	CTR 12762	SYM SWEEP 150 KTS SCAS OFF	29.8
FLT 225	CTR 12764	ASYM SWEEP 170 KTS 86% RPM	34.4
FLT 225	CTR 12765	ASYM SWEEP 170 KTS 86% RPM	31.0
FLT 225	CTR 12766	ASYM SWEEP 170 KTS 86% RPM	29.6
FLT 225	CTR 12767	SYM SWEEP 170 KTS 86% RPM	28.6
FLT 225	CTR 12768	SYM SWEEP 170 KTS 86% RPM	30.3
FLT 225	CTR 12769	SYM SWEEP 170 KTS 86% RPM	32.0
FLT 225	CTR 12777	SYM SWEEP 190 KTS 86% RPM	32.3
FLT 225	CTR 12778	SYM SWEEP 190 KTS 86% RPM	29.4
FLT 225	CTR 12779	SYM SWEEP 190 KTS 86% RPM	32.6
FLT 225	CTR 12780	ASYM SWEEP 190 KTS 86% RPM	29.9
FLT 225	CTR 12781	ASYM SWEEP 190 KTS 86% RPM	32.3
FLT 225	CTR 12783	ASYM SWEEP 190 KTS 86% RPM	30.5
FLT 225	CTR 12785	ASYM SWEEP 210 KTS 86% RPM	29.8
FLT 225	CTR 12786	ASYM SWEEP 210 KTS 86% RPM	30.4
FLT 225	CTR 12787	ASYM SWEEP 210 KTS 86% RPM	30.6
FLT 225	CTR 12788	SYM SWEEP 210 KTS 86% RPM	29.6
FLT 225	CTR 12789	SYM SWEEP 210 KTS 86% RPM	30.6
FLT 225	CTR 12790	SYM SWEEP 210 KTS 86% RPM	28.9
FLT 225	CTR 12792	SYM SWEEP VMAX 86% RPM	28.9
FLT 225	CTR 12793	SYM SWEEP VMAX 86% RPM	30.6
FLT 225	CTR 12794	SYM SWEEP VMAX 86% RPM	29.6
FLT 225	CTR 12795	ASYM SWEEP VMAX 86% RPM	31.2
FLT 225	CTR 12796	ASYM SWEEP VMAX 86% RPM	30.3
FLT 225	CTR 12797	ASYM SWEEP VMAX 86% RPM	30.2

Table A6. (Concluded.)

FLT 225	CTR 12799	ASYM SWEEP 150 KTS ARS OFF	31.6
FLT 225	CTR 12800	ASYM SWEEP 150 KTS ARS OFF	29.5
FLT 225	CTR 12801	ASYM SWEEP 150 KTS ARS OFF	30.7
FLT 225	CTR 12802	SYM SWEEP 150 KTS ARS OFF	28.2
FLT 225	CTR 12803	SYM SWEEP 150 KTS ARS OFF	29.9
FLT 225	CTR 12804	SYM SWEEP 150 KTS ARS OFF	28.7
FLT 225	CTR 12805	ASYM SWEEP FFS OFF 150 KTS	30.3
FLT 225	CTR 12806	ASYM SWEEP FFS OFF 150 KTS	28.1
FLT 225	CTR 12807	ASYM SWEEP FFS OFF 150 KTS	29.6
FLT 225	CTR 12808	SYM SWEEP FFS OFF 150 KTS	29.5
FLT 225	CTR 12809	SYM SWEEP FFS OFF 150 KTS	29.5
FLT 225	CTR 12810	SYM SWEEP FFS OFF 150 KTS	29.6
FLT 225	CTR 12824	ASYM SWEEP 150 KTS 86% RPM	32.1
FLT 225	CTR 12825	ASYM SWEEP 150 KTS 86% RPM	31.7
FLT 225	CTR 12826	ASYM SWEEP 150 KTS 86% RPM	30.8
FLT 225	CTR 12827	SYM SWEEP 150 KTS 86% RPM	32.7
FLT 225	CTR 12828	SYM SWEEP 150 KTS 86% RPM	30.8
FLT 225	CTR 12829	SYM SWEEP 150 KTS 86% RPM	30.0

Table A7. TRENDS counter list for flight 226

		Pilot Comments	Duration, sec
FLT 226	CTR 12853	SYM SWEEP 150 KTS 15K FT	30.3
FLT 226	CTR 12854	SYM SWEEP 150 KTS 15K FT	28.9
FLT 226	CTR 12855	SYM SWEEP 150 KTS 15K FT	27.2
FLT 226	CTR 12856	ASYM SWEEP 150 KTS 15K FT	37.3
FLT 226	CTR 12859	ASYM SWEEP 150 KTS 15K FT	28.7
FLT 226	CTR 12860	ASYM SWEEP 150 KTS 15K FT	30.8
FLT 226	CTR 12862	ASYM SWEEP 190 KTS 15K FT	29.0
FLT 226	CTR 12863	ASYM SWEEP 190 KTS 15K FT	28.6
FLT 226	CTR 12864	ASYM SWEEP 190 KTS 15K FT	28.8
FLT 226	CTR 12865	SYM SWEEP 190 KTS 15K FT	27.7
FLT 226	CTR 12866	SYM SWEEP 190 KTS 15K FT	26.9
FLT 226	CTR 12867	SYM SWEEP 190 KTS 15K FT	27.7
FLT 226	CTR 12869	SYM SWEEP 210 KTS 15K FT	27.2
FLT 226	CTR 12870	SYM SWEEP 210 KTS 15K FT	27.2
FLT 226	CTR 12871	SYM SWEEP 210 KTS 15K FT	27.1
FLT 226	CTR 12872	ASYM SWEEP 210 KTS 15K FT	27.2
FLT 226	CTR 12873	ASYM SWEEP 210 KTS 15K FT	27.5
FLT 226	CTR 12874	ASYM SWEEP 210 KTS 15K FT	27.0
FLT 226	CTR 12875	ASYM SWEEP 150 KTS WINDMILL	30.5
FLT 226	CTR 12876	ASYM SWEEP 150 KTS CLIMB	26.8
FLT 226	CTR 12877	ASYM SWEEP 150 KTS WINDMILL	28.3
FLT 226	CTR 12878	ASYM SWEEP 150 KTS CLIMB	27.9
FLT 226	CTR 12879	ASYM SWEEP 150 KTS WINDMILL	29.0
FLT 226	CTR 12880	ASYM SWEEP 150 KTS CLIMB	28.5
FLT 226	CTR 12881	SYM SWEEP 150 KTS WINDMILL	27.1
FLT 226	CTR 12882	SYM SWEEP 150 KTS CLIMB	28.3
FLT 226	CTR 12883	SYM SWEEP 150 KTS WINDMILL	28.3
FLT 226	CTR 12884	SYM SWEEP 150 KTS CLIMB	27.6
FLT 226	CTR 12885	SYM SWEEP 150 KTS WINDMILL	27.0
FLT 226	CTR 12886	SYM SWEEP 150 KTS CLIMB	28.3

Table A8. TRENDS counter list for flight 228

		Pilot Comments	Duration, sec
FLT 228	CTR 13012	ASYM SWEEP 150KTS 10K FT 86%	29.7
FLT 228	CTR 13013	ASYM SWEEP 150KTS 10K FT 86%	29.1
FLT 228	CTR 13014	ASYM SWEEP 150KTS 10K FT 86%	28.3
FLT 228	CTR 13015	SYM SWEEP 150 KTS 10K FT 86%	28.9
FLT 228	CTR 13016	SYM SWEEP 150 KTS 10K FT 86%	30.6
FLT 228	CTR 13017	SYM SWEEP 150 KTS 10K FT 86%	29.0
FLT 228	CTR 13034	ASYM SWEEP 150KTS 10K FT 86%	28.5
FLT 228	CTR 13035	ASYM SWEEP 150KTS 10K FT 86%	28.9
FLT 228	CTR 13036	ASYM SWEEP 150KTS 10K FT 86%	29.6
FLT 228	CTR 13037	SYM SWEEP 150 KTS 10K FT 86%	28.1
FLT 228	CTR 13038	SYM SWEEP 150 KTS 10K FT 86%	28.2
FLT 228	CTR 13039	SYM SWEEP 150 KTS 10K FT 86%	30.3
FLT 228	CTR 13041	ASYM SWEEP 150KTS 10K FT 86%	28.2
FLT 228	CTR 13042	ASYM SWEEP 150KTS 10K FT 86%	32.0
FLT 228	CTR 13043	ASYM SWEEP 150KTS 10K FT 86%	34.2
FLT 228	CTR 13044	SYM SWEEP 150 KTS 10K FT 86%	27.7
FLT 228	CTR 13045	SYM SWEEP 150 KTS 10K FT 86%	27.2
FLT 228	CTR 13046	SYM SWEEP 150 KTS 10K FT 86%	30.6

APPENDIX B

DATA ACQUISITION AND STORAGE

The input and output data analyzed in this study were mainframe PCM aircraft parameters, stored by an on-board flight recorder as 11-bit words (including a sign bit) at a sampling rate of 125.35 ± 0.25/sec (125.5/sec nominal). Three-pole Butterworth anti-aliasing prefilters were used in the aircraft signal conditioning.

All aeroelastics parameters were sampled sequentially. Similar parameters (e.g., strain gages) were placed adjacent in the data stream to minimized time skews. (FRESPID uses a digital anti-jitter filter to reduce resulting distortion in the spectra, and NAVFIT always fitted a time delay separate from the structural model to compensate for any residual time skew between the input and output parameters.)

The analog (serial PCM) flight tapes were digitized to parallel (VAX standard) archival tapes. Time histories of selected input and output parameters were copied off the digital tapes and stored in the XV-15 data base (TRENDS, ref. 19) on a VAX 11/785 computer, where the spectral analyses were performed. The data were stored in the TRENDS "Special Aeroelastics" data group as "Raw" data, with no further decimation or filtering by TRENDS. (Filtering is included in FRESPID; see Windowing and Filtering in the Analysis Methods section.)

Table B1 lists the item codes that were stored and analyzed. The item code is the abbreviated label used to identify each parameter accessible in TRENDS.

Table B1. Aeroelastics item codes

Right flaperon LVDT	D747
Left flaperon LVDT	D800
Right-wing-spar beam bending strain gage	B600
Left-wing-spar beam bending strain gage	B601
Right-wing-spar chord bending strain gage	B603
Left-wing-spar chord bending strain gage	B604
Right-wing-spar torsion strain gage	M606
Left-wing-spar torsion strain gage	M607

The right and left torsion strain-gage signals (M606 and M607) have oppositely defined signs. This is so that the data in TRENDS will show responses in the same sense for the first torsional wing mode, which is antisymmetric. However, the two chord strain gages are also opposite in sign, and B603 had about half the response magnitude of B604. This was found to be an error in data processing (an incorrect calibration factor), and was corrected in FRESPID in order to get good sum-and-difference results before applying the chirp z-transform. (The correction was not made in ref. 9.)

REFERENCES

1. Hall, W. E., Jr.: Prop-Rotor Stability at High Advance Ratios. J. American Helicopter Soc., vol. 11, no. 2, April 1966, pp. 11–26.
2. Edenborough, H. K.: Investigation of Tilt Rotor VTOL Aircraft Rotor-Pylon Stability. J. Aircraft, vol. 5, no. 2, March-April 1968, pp. 97–105.
3. Popelka, D.; Sheffler, M.; and Bilger, J.: Correlation of Test and Analysis for the 1/5-Scale V-22 Aeroelastic Model. J. American Helicopter Soc., vol. 32, no. 2, April 1987, pp. 21–33.
4. Ormiston, R. A.; Warmbrodt, W. G.; Hodges, D. H.; and Peters, D. A.: Rotorcraft Aeroelastic Stability. NASA/Army Rotorcraft Technology, Vol. 1: Aerodynamics, and Dynamics and Aeroelasticity. NASA CP-2495, 1988, pp. 353–529.
5. Johnson, W.; Lau, B. H.; and Bowles, J. V.: Calculated Performance, Stability, and Maneuverability of High-Speed Tilting-Prop-Rotor Aircraft. NASA TM-88349, Sept. 1986.
6. Alexander, H. R.; Maisel, M. D.; and Giulianetti, D. J.: The Development of Advanced Technology Blades for Tiltrotor Aircraft. Paper No. 39, 11th European Rotorcraft Forum, London, England, Sept. 10–13, 1985.
7. Tischler, M. B.; Leung, J. G. M.; and Dugan, D. C.: Frequency-Domain Identification of XV-15 Tilt-Rotor Aircraft Dynamics. AIAA Paper 83-2695, Nov. 1983.
8. Tischler, M. B.: Frequency-Response Identification of XV-15 Tilt-Rotor Aircraft Dynamics. NASA TM-89428, May 1987.
9. Acree, C. W.; and Tischler, M. B.: Using Frequency-Domain Methods to Identify XV-15 Aeroelastic Modes. NASA TM-100033, Nov. 1987.
10. Acree, C. W., Jr.; and Tischler, M. B.: Identification of XV-15 Aeroelastic Modes Using Frequency-Sweeps. J. Aircraft, vol. 26, no. 7, July 1989, pp. 667–675.
11. Schroers, L. G.: Dynamic Structural Aeroelastic Stability Testing of the XV-15 Tilt Rotor Research Aircraft. NASA TM-84293, Dec. 1982.
12. Bilger, J. M.; Marr, R. L.; and Zahedi, A.: In-Flight Structural Dynamic Characteristics of the XV-15 Tilt Rotor Research Aircraft. AIAA Paper 81-0612, 1981.
13. Johnson, W.: A Comprehensive Analytical Model of Rotorcraft Aerodynamics and Dynamics. Part I: Analysis Development. NASA TM-81182, June 1980.
14. Johnson, W.: An Assessment of the Capability To Calculate Tilting Prop-Rotor Aircraft Performance, Loads, and Stability. NASA TP-2291, March 1984.
15. Johnson, W.: A Discussion of Dynamic Stability Measurement Techniques. NASA TM X-73,081; Nov. 1975.
16. Johnson, W.: Development of a Transfer Function Method for Dynamic Stability Measurement. NASA TN D-8522, July 1977.
17. Flannelly, W. G.; Fabunmi, J. A.; and Nagy, E. J.: Analytical Testing. NASA CR-3429, May 1981.
18. Bendat, J. S.; and Piersol, A. G.: Random Data. Second ed. John Wiley and Sons, Inc., New York, 1986.
19. Bjorkman, W. S.; and Bondi, M. J.: TRENDS: The Aeronautical Post-Test Database Management System. NASA TM-101025, Jan. 1990.
20. Hodgkinson, J.; LaManna, W. J.; and Heyde, J. L.: Handling Qualities of Aircraft with Stability and Control Augmentation Systems—A Fundamental Approach. Paper No. 264, Aeron. J., vol. 80, no. 782, Feb. 1976, pp. 75–81.
21. Tischler, M. B.; and Cauffman, M. G.: Frequency-Response Method for Rotorcraft System Identification: Flight Applications to BO-105 Coupled Rotor/Fuselage Dynamics. J. American Helicopter Soc., vol. 37. no. 3, July 1992, pp. 3–17.
22. Otnes, R. K.; and Enochson, L.: Applied Time Series Analysis. John Wiley and Sons, Inc., New York, 1978.
23. Harris, F. J.: On the Use of Windows for Harmonic Analysis with the Discrete Fourier Transform. Proceedings of the IEEE, vol. 66, no. 1, Jan. 1978, pp. 51–83.
24. Nuttall, A. H.: Some Windows with Very Good Sidelobe Behavior. IEEE Transactions on Acoustics, Speech, and Signal Processing, vol. ASSP-29, no. 1, Feb. 1981, pp. 84–91.
25. Rabiner, L. R.; and Gold, B.: Theory and Application of Digital Signal Processing. Prentice-Hall, Inc., Englewood Cliffs, New Jersey, 1975.
26. Fabunmi, J. A.: Developments in Helicopter Ground Vibration Testing. J. American Helicopter Soc., vol. 31, no. 3, July 1986, pp. 54–59.
27. Carter, G. C.; Knapp, C. H.; and Nuttal, A. H.: Estimation of the Magnitude-Squared Coherence Function via Overlapped Fast Fourier Transform Processing. IEEE Transactions on Audio and Electroacoustics, vol. AU-21, no. 4, Aug. 1973, pp. 337–444.

REPORT DOCUMENTATION PAGE

Form Approved
OMB No. 0704-0188

1. AGENCY USE ONLY *(Leave blank)*	2. REPORT DATE	3. REPORT TYPE AND DATES COVERED
	May 1993	Technical Paper

4. TITLE AND SUBTITLE

Determining XV-15 Aeroelastic Modes from Flight Data with Frequency-Domain Methods

5. FUNDING NUMBERS

505-61-51

6. AUTHOR(S)

C. W. Acree, Jr. and Mark B. Tischler*

7. PERFORMING ORGANIZATION NAME(S) AND ADDRESS(ES)

Ames Research Center
Moffett Field, CA 94035-1000
*Aeroflightdynamics Directorate, U.S. Army Aviation and Troop Command, Ames Research Center, Moffett Field, CA 94035-1000

8. PERFORMING ORGANIZATION REPORT NUMBER

A-91002

9. SPONSORING/MONITORING AGENCY NAME(S) AND ADDRESS(ES)

National Aeronautics and Space Administration
Washington, DC 20546-0001

10. SPONSORING/MONITORING AGENCY REPORT NUMBER

NASA TP-3330
USAATCOM TR 93-A-004

11. SUPPLEMENTARY NOTES

Point of Contact: C. W. Acree, Ames Research Center, MS 237-5, Moffett Field, CA 94035-1000
(415) 604-5423

12a. DISTRIBUTION/AVAILABILITY STATEMENT

Unclassified-Unlimited
Subject Category – 05

Available from the NASA Center for AeroSpace Information,
800 Elkridge Landing Road, Linthicum Heights, MD 21090; (301) 621-0390

12b. DISTRIBUTION CODE

13. ABSTRACT ***(Maximum 200 words)***

The XV-15 tilt-rotor wing has six major aeroelastic modes that are close in frequency. To precisely excite individual modes during flight test, dual flaperon exciters with automatic frequency-sweep controls were installed. The resulting structural data were analyzed in the frequency domain (Fourier transformed). All spectral data were computed using chirp z-transforms. Modal frequencies and damping were determined by fitting curves to frequency-response magnitude and phase data. The results given in this report are for the XV-15 with its original metal rotor blades. Also, frequency and damping values are compared with theoretical predictions made using two different programs, CAMRAD and ASAP. The frequency-domain data-analysis method proved to be very reliable and adequate for tracking aeroelastic modes during flight-envelope expansion. This approach required less flight-test time and yielded mode estimations that were more repeatable, compared with the exponential-decay method previously used.

14. SUBJECT TERMS	15. NUMBER OF PAGES
XV-15, Rotorcraft, Tiltrotor, Aeroelastics, Flight test	68
	16. PRICE CODE: A04

17. SECURITY CLASSIFICATION OF REPORT	18. SECURITY CLASSIFICATION OF THIS PAGE	19. SECURITY CLASSIFICATION OF ABSTRACT	20. LIMITATION OF ABSTRACT
Unclassified	Unclassified		

NSN 7540-01-280-5500

☆U.S. GOVERNMENT PRINTING OFFICE: 1993 - 786-499/99149

Standard Form 298 (Rev. 2-89)
Prescribed by ANSI Std. Z39-18
298-102

28. Flutter Testing Techniques, NASA SP-415, 1976.
29. Houbolt, J. C.: On Identifying Frequencies and Damping in Subcritical Flutter Testing. Flutter Testing Techniques, NASA SP-415, 1976, pp. 1–42.
30. Tischler, M. B.: Advancements in Frequency-Domain Methods for Rotorcraft System Identification. Vertica, vol. 13, no. 3, 1989, pp. 327–343.
31. Arrington, W. L.; Kumpel, M.; Marr, R. L.; and McEntire, K. G.: XV-15 Tilt Rotor Research Aircraft Flight Test Data Report. Vol. 3: Structural Loads and Dynamics. NASA CR-177406, June 1985.
32. Crow, E. L.; Davis, F. A.; and Maxfield, M. W.: Statistics Manual. Dover Publications, Inc., New York, 1960.
33. Kvaternik, R. G.: Studies in Tilt-Rotor VTOL Aircraft Aeroelasticity. Ph.D. Thesis, Case Western Reserve University, Cleveland, Ohio, June 1973 (Order #74-2538).

National Aeronautics and
Space Administration

Ames Research Center
Moffett Field, California 94035-1000

BULK RATE
POSTAGE & FEES PAID
NASA
Permit No. G-27